Doctoral Dissertation

Structure Control and Characterization of Tungsten Oxide Nanoparticles by Aqueous Solution Methods

MOHAMED SALAHELDIN EL-NOUBY

January 2014

Division of Materials and Manufacturing Science

Graduate School of Engineering,

Osaka University

Abstract

Tungsten oxides are interesting semiconductors with a wide- range of potential applications. The performance of tungsten oxides in such applications depend on its microstructure properties. In particular, there are needs to develop a facile, green, and economic synthesis route to produce tungsten oxides with controllable microstructure properties. Tungsten oxide nanoparticles have been synthesized from aqueous precursor via hydrothermal method, aqueous sol-gel method and galvanostatic electrodeposition method. Tungsten oxides with various structures have been successfully obtained by these methods. Monoclinic WO_3 square nanoplates have been synthesized via mild hydrothermal treatment of ion-exchanged precursor at 50 ^oC. The nanoplates have an edge size of ~700 nm and thickness of 10 nm. One-dimensional crystal growth of orthorhombic $WO_3 \cdot 0.33H_2O$ was demonstrated by hydrothermal treatment of ion-exchanged precursor at 120 ^oC. The obtained nanoneedles have a length of 250-300 nm and diameter of 25-30 nm. Hexagonal WO_3 was successfully obtained by dehydration- induced Topotactic transformations of $WO_3 \cdot 0.33H_2O$. WO_3 nanoparticles films were fabricated by spin coated a stabilized ion –exchanged precursor on ITO glass, then annealed at 300 ^oC. Hydrogen peroxide and oxalic acid were applied as stabilizing agents. The thickness of the prepared WO_3 thin films was ranged between 0.33 μm to 9.82 μm, depending on the number of applied layers. The effect of stabilizing agent and thickness on the electrochromic performance of the obtained thin films was examined. The highest coloration efficiency of 64.2 cm^2/C was obtained for the open porous structure of the two-layer film prepared with W^+ ion concentration of 0.1 M, and 1% hydrogen peroxide and 4% oxalic acid. As comparison study, thin films of WO_3 nanoparticles were deposited on ITO by galvanostatic electrodeposition method. The effect of preparation parameters such as tungsten ions concentration, pH, current density and annealing on the properties and performance of WO_3 thin films electrochromic materials were investigated. Triclinic WO_3 structure was prepared at 0.1 M of W^+ and current density of 0.5 mA/cm^2, while at 0.2 M of W^+, and 1 mA/cm^2, orthorhombic structure was revealed. The highest diffusion coefficient of $6.81 \times 10^{-11} cm^2/S$ and coloration efficiency of 62.6 cm^2/C were obtained for the films prepared at pH 2, 1 mA/cm^2 and 0.1 M of W^+.

Contents

Chapter 1
Introduction

1.1 Introduction

Tungsten oxide (WO_3) is a transition metal oxide. After the discovery of electrochromic (EC) effect in WO_3 by Deb in 1969 [1], the research interest of WO_3 was sparked not only for EC devices but also many other related applications [2-6]. The WO_3-based EC ‘‘smart windows’’ have already emerged as a viable commercial product after extensive technological developments, making a huge impact on energy saving [7, 8]. In addition, the unique ability to induce bi-stable optical and electrical properties in WO_3 has led to many interests such as photochemical cell [5, 6] and photocatalysts [9-12] .

Recently, with advent of nanotechnologies, synthesis and characterization of WO_3 nanostructures or nanoparticles have been increasingly prominent [13, 14]. To date, the WO_3 nanoparticles with different morphologies such as one-dimensional nanoneedles [15] or nanofiber [16], two-dimensional nanoplates [17-22] or nanosheets [10, 23, 24] and spherical nanoparticles [25], have been synthesized by various methods. These nanoparticles are versatile and exceptionally offer unique characteristics. For example, it was reported that the crystalline WO_3 nanoparticle films showed greater charge density for proton intercalation and comparable coloration efficiency, compared with conventional amorphous WO_3 EC films [26-28]. The improvements of the EC properties of the nanoparticle film have been attributed to a larger active surface area and to the low density of the films [29]. The nanostructuring of WO_3 provides new opportunities and significant impact on various applications.

Controlled synthesis of WO_3 nanoparticles is still a focused subject to explore further nanostructure-dependent properties. In particular, there are needs for economic and environmentally benign synthetic routes which can produce WO_3 nanoparticles efficiently. With this regard, the present thesis concerns the structural control and characterization of WO_3 nanoparticles by aqueous solution methods.

1.2 Tungsten Oxide (WO_3)

In this section, various crystal structures of WO_3 are summarized. Then some properties of WO_3 nanoparticles that have been presented in the literature are addressed to show that the nanostructuring of WO_3 provides new opportunities.

1.2.1 Crystal structure

The structure of tungsten oxide (WO_3) is best described as a three-dimensional network of corner-sharing WO_6 octahedra. The connectivity of this network is identical to the cubic ReO_3 structure and the AMO_3 perovskite structure in the absence of an A cation. However, the symmetry of WO_3 is lowered from the ideal ReO_3 structure by two distortions: tilting of WO_6 octahedra and displacement of tungsten from the center of its octahedron. Tungsten oxide adopts at least five distinct crystallographic modifications between absolute zero and its melting point. The phase transformation occurs in the following sequence [30, 31]: monoclinic II (ε -WO_3, < − 43 °C) → triclinic (δ -WO_3, − 43 °C to 17 ° C) → monoclinic I (γ -WO_3, 17 ° C to 330 °C) → orthorhombic (β -WO_3, 330 °C to 740 °C) → tetragonal (α -WO_3, > 740 °C). The above phase transition of WO_3 has been reported to be partially reversible. At room temperature, monoclinic I (γ -WO_3) has been reported as the most stable phase. Triclinic (δ- WO_3) is also observed. Hereafter, unless specified, the term "monoclinic" will be used to refer to the monoclinic I (γ -WO_3) phase (see Fig.1.1 (a)).

Another possible stable phase at room temperature for WO_3 is hexagonal (h-WO_3). It was first reported by Gerand et al. in 1979 [32]. Hexagonal (h-WO_3) is built up of layers in which the WO_6 octahedra share their corners, forming three and six- membered rings in the a b -plane. For h-WO_3, the stacking of these layers along the [001] axis leads to the formation of one- dimensional hexagonal tunnels along this direction (see Fig.1.1 (b)).

Hexagonal (h-WO_3) was originally obtained from the dehydration of tungstate ($WO_3 \cdot 0.33H_2O$) [32]. However, this hexagonal crystal phase is metastable and reported to be transformed into a monoclinic structure when annealed at temperatures exceeding 400 °C [33].

Investigations of WO_3 hydrates ($WO_3 \cdot nH_2O$) or "tungstic acids" are important as they are closely related to WO_3. The importance of $WO_3 \cdot nH_2O$ stems from the fact that generally in liquid-phase synthesis routes, $WO_3 \cdot nH_2O$ are first produced and subsequently annealed to obtain the desired crystal phase of WO_3 [30]. Recently, unique morphologies of $WO_3 \cdot nH_2O$ such as nanoneedles, nanofibers and nanoplates have been synthesized by various methods.

Among the WO_3 hydrates, the structure of $WO_3 \cdot 2H_2O$, $WO_3 \cdot H_2O$, and $WO_3 \cdot 0.33H_2O$ have been well documented. $WO_3 \cdot 2H_2O$ ($H_2WO_4 \cdot H_2O$) possesses a layered structure, which is composed of $WO_5(OH)_2$ single sheets in corner-sharing mode. The second water molecule of the dihydrate is found to be positioned between the layers [34]. The monohydrate $WO_3 \cdot H_2O$ has a two-dimensional crystalline structure where each plane consists of WO_6 octahedra sharing four of their six corners in the ac plane. Across these planes, one oxygen forms part of a short W=O bond and the other belongs to a structural water molecule. These planes are connected by hydrogen bond [35] (see Fig. 1.2 (a)). The hydrate, $WO_3 \cdot 0.33H_2O$ precursor of h-WO_3 was first reported by Gerand et al. in 1981 [36]. The $WO_3 \cdot 0.33H_2O$ has a structure built up of the same kind of WO_6 layers as h- WO_3 with, however, one layer out of two shifted by a/2 along the [001] axis. This compound is characterized by two types of WO_6 octahedra:

Space group	Lattice parameters
P21/n(14)	a= 7.3060 Å b= 7.5400 Å c=7.6920 Å

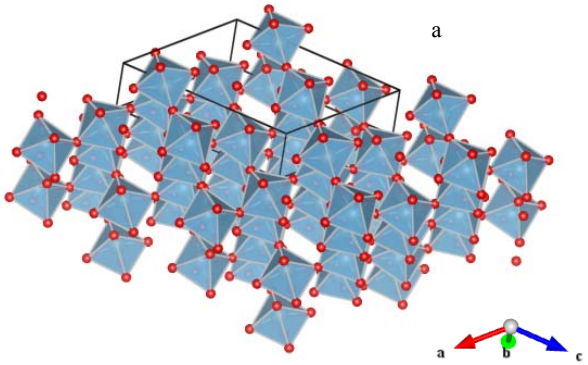

Space group	Lattice parameters
P6/mmm(191)	a= 7.2980 Å c= 3.8990 Å

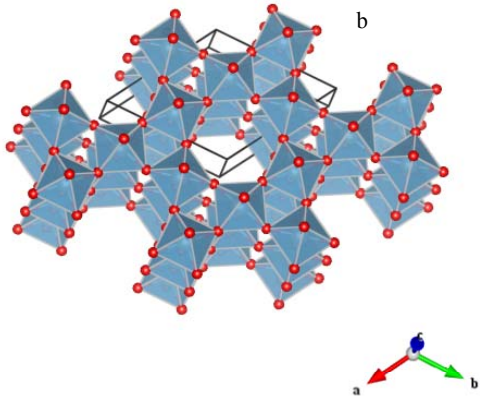

Fig. 1.1 Schematic representation of the crystalline structures of (a) monoclinic and (b) hexagonal WO_3.

Space group	Lattice parameters
Pmnb(62)	a= 5.2380 Å
	b= 10.7040 Å
	c= 5.1200 Å

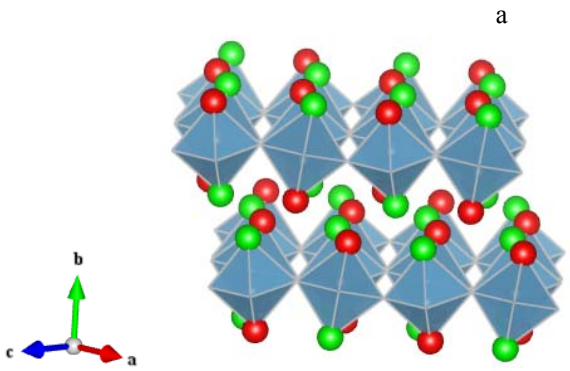

● Structural H_2O

● Terminal O

Space group	Lattice parameters
Fmm2(42)	a= 7.3590 Å
	b= 12.5130 Å
	c=7.7040 Å

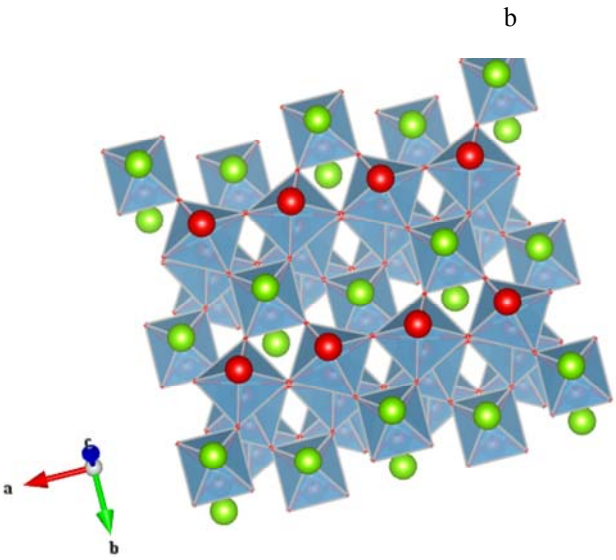

Fig. 1.2 Schematic representation of the crystalline structures of (a) orthorhombic $WO_3 \cdot H_2O$ and (b) orthorhombic $WO_3 \cdot 0.33H_2O$.

W (1) where the six oxygen atoms connect the octahedra together by corner sharing and W (2) where two of the oxygen atoms are implicated in a short W=O bond and a longer W-OH_2 bond respectively, both bonds being along the [001] direction. This stacking leads to cavities, which are occupied by the structural water molecules [37] (see Fig. 1.2 (b)).

1.2.2 Some properties of WO_3 nanoparticles

WO_3 is a wide-band gap n-type semiconductor, with an energy band gap (Eg), corresponding to the difference between the energy levels of the valence band, formed by filled O 2p orbitals and the conduction band formed by empty W 5d orbitals [38]. Crystalline WO_3 has been reported to show a typical E g of ≈ 2.5-2.7 eV for indirect transitions at room temperature [39]. On the other hand, amorphous WO_3 normally possesses a relatively large E_g on the order of ≈ 3.46 eV, [38]. Recently, several experimental results indicate that the energy band gap increases with reducing grain size in nanostructured WO_3 films. It has been considered that this observed blue shift can be attributed to the quantum confinement effect [40].

WO_3 is one of the most widely used EC materials [23, 41, 42]. The general EC phenomena of WO_3 is due to the formation of tungsten bronze (M_xWO_3) electrochemically. The electrochemical reaction that results in the chromic response of WO_3 can be described by considering the injection of a quantity (x) of positive ions (M^+) and an equal quantity of electrons (e^-). Symbolically, this reaction can be represented as follows [43]:

$$WO_3 + xM^+ + xe^- \longleftrightarrow M_xWO_3 \qquad (1.1)$$

Typical ions can be $M^+ = H^+$, Li^+ and Na^+ among others, and the quantity x becomes the stoichiometric parameter of the product and can vary between 0 and 1.

Most of the WO_3 EC devices have focused on amorphous films due to their high coloration efficiency and fast color/bleach time [26, 27]. Unfortunately, the amorphous WO_3 has poor structural and chemical stability, resulting in poor EC stability. Although crystalline WO_3 is much more stable structurally, it has a relatively lower coloration efficiency and slow switching time. Recently, nanostructured WO_3 films with a high degree of porosity has been overcome the draw backs of crystalline WO_3 for EC application [44]. The WO_3 particle films improve the surface-to-volume ratio, allowing more surface area available for reactions, hence producing superior optical modulation as compared to the dense films [44]. Additionally, the hexagonal tunnel structure enhances species diffusion within the system, which may improve the chromic response time. [45]].

As mentioned, WO_3 has indirect band gap energy of 2.5–2.8 eV that can capture approximately 12% of the solar spectrum and can absorb light in the visible spectrum up to 500 nm. Given its band gap, WO_3 is a more suitable material for photoelectrochemical water splitting than TiO_2 (Eg = 3.0-3.2 eV). TiO_2 absorbs only in the ultraviolet region of the spectrum and captures approximately 4% of solar irradiation [6]. WO_3 also exhibits high resistance against photocorrosion and good chemical stability in acidic aqueous solutions (pH < 4) under solar illumination. Recently, to improve the incident photon-to-electron conversion efficiency of WO_3 photoanodes, much effort has focused on design and growth of nanoparticle-based WO_3 [22]. The nanoparticle based WO_3 photoanodes have high interfacial contact area compared with bulk WO_3 that can increase the density of redox-active sites and enhance light harvesting and charge separation efficiency.

As can be seen, the nanostructuring of WO_3 provides new opportunities, and thereby controlled synthesis of WO_3 nanoparticles is still a focused subject to explore further nanostructure-dependent properties.

1.3 Synthesis routes for WO_3 nanoparticles

1. 3.1. Vapor-Phase Synthesis

The category of vapor-phase deposition (VPD) includes a wide range of material synthesis techniques such as sputtering [46, 47], chemical vapor deposition [26, 48], thermal evaporation [49], laser ablation [17], and spray pyrolysis [50, 51]. In general, it involves the condensation of vaporized source material onto the targeted substrates. J. Thangala et al. have reported that one-dimensional WO_x nanowires can be obtained under optimum thermal evaporation method [49]. The diameter of their obtained nanowires ranged from 20 to 100 nm. Other nanomorphologies such as two-dimensional nanoplate and nanosheet have not been obtained through vapor-phase synthesis routes.

1.3.2. Liquid-Phase Synthesis

Liquid-phase synthesis methods are inexpensive and offer better control of structure of WO_3 when compared to the vapor-phase methods. The use of the liquid-phase synthesis is advantageous for large-scale production of such coatings and a number of such routes are available. These can use a variety of different sources, for examples; tungsten alkoxide WCl_6 [52] for non-aqueous precursor, and sodium tungstate Na_2WO_4 [53] and tungsten metal W for aqueous precursor. The non-aqueous precursors are expensive and highly volatile, and the WO_3 films produced from them are rather compact and featureless [54].With this regards, over the years, environmentally benign synthetic routes using aqueous precursors have been investigated for synthesizing WO_3 in various nanostructured forms. The following focuses hydrothermal, aqueous sol-gel and electrodeposition methods as aqueous synthesis methods.

1.3.2.1 Hydrothermal method

Hydrothermal treatment of a tungstic acid solution (H_2WO_4) as precursor is a facile and cost-effective technique. Typically, the precursor, called acidified precursor is obtained by acidification of aqueous sodium tungstate solutions (Na_2WO_4) using strong acid such as HCl and HNO_3 [55]. During the hydrothermal treatment, hydrolysis of H_2WO_4 proceeds, condensing to form mainly crystalline $WO_3 \cdot nH_2O$ precipitates (see Table 1.1). Subsequent annealing leads to obtain the crystal phase of WO_3. A vast number of hydrothermal treatments have been investigated using the acidified precursor as shown in Table 1.1, and it has been shown that morphologies and crystal structures of $WO_3 \cdot nH_2O$ precipitates strongly depend on aging temperature, aging time and additives used. The acidified precursor obviously contains by-product ions such as Na^+. However, it is still unclear the effect of co-existence of Na^+ on the morphological and structural evolution of $WO_3 \cdot nH_2O$ nanoparticles. In addition, under the utilization of the acidified precursor, the unavoidably contaminated cations such as Na^+ in the final products may result in negative effects on the performances of resulting WO_3 nanoparticles [17, 56].

An ion-exchanged precursor is an alternative acidified precursor [57], which is prepared by acidification only through a protonated cation-exchange resin. It contains intrinsically negligible amount of by-product ions such as Na^+ and Cl^-, and therefore can be used as impurity-free precursor [53, 58]. Nevertheless, the hydrothermal treatment of ion-exchanged precursor has been less attention. There are only a few reports on the formation of $WO_3 \cdot nH_2O$ nanoplates in the ion-exchanged precursor. For producing impurity-free WO_3 nanoparticles, systematic study is needed to understand morphological and structural evolution of $WO_3 \cdot nH_2O$ in ion-exchanged precursor.

Table 1.1 Summary of WO_3 nanoparticles synthesized by hydrothermal treatment of acidified precursor.

Morphology	Crystal phase	Tungsten source	Acidification	Additive or Additional step	Temp. [^oC]	Time [h]	Ref
Nanoplate W>1μm T:N/A	$WO_3 \cdot H_2O$	$Na_2WO_4 \cdot 2H_2O$	HCl	Washing (Na~40ppm)	120	20	[59]
Nanoplate W~1μmT:N/A	$WO_3 \cdot 0.33H_2O$	$Na_2WO_4 \cdot 2H_2O$	HCl	Washing (Na~160ppm)	120	19	[59]
Nanoplate W190nm T50nm	$WO_3 \cdot H_2O$	$(NH_4)_{10}W_{12}O_{41} \cdot 5H_2O$	HNO_3	-	80 & R.T.	1 24	[60]
Nanoplate W~100nm T:N/A	$WO_3 \cdot H_2O$	$Na_2WO_4 \cdot 2H_2O$	HBF_4	-	30~90	10	[18]
Nanoplate W 400nm~1μm	t-WO_3	$Na_2WO_4 \cdot 2H_2O$	HBF_4	-	160	10	[18]
Nanoplate W>1μm T>50nm	$WO_3 \cdot H_2O$	$Na_2WO_4 \cdot 2H_2O$	HCl	$(NH_4)_2C_2O_4$	120	12	[5]
Nanoplate W~1μm T~50nm	m-H_2O	$Na_2WO_4 \cdot 2H_2O$	HCl	$(NH_4)_2C_2O_4$	180	12	[5]
Nanoplate W~700m T~N/A	$WO_3 \cdot H_2O$	$Na_2WO_4 \cdot 2H_2O$	HCl	-	40	168	[61]
Nanoplate W~150nmT~25nm	$WO_3 \cdot H_2O$	$Na_2WO_4 \cdot 2H_2O$	HCl	$H_2C_2O_4$	90	3	[19]
Nanoplate W~100nmT30nm	t-WO_3	$Na_2WO_4 \cdot 2H_2O$	HCl	Tartaric acid	160	12	[62]
Nanoplate W 200nm~2μm	h-WO_3	$Na_2WO_4 \cdot 2H_2O$	HCl	$C_4H_{12}N_2O_6$	150	6	[63]
Nanoneedle L~300nm, D<50nm	$WO_3 \cdot 0.33H_2O$	$Na_2WO_4 \cdot 2H_2O$	HCl	-	120	-	[32]
Nanofiber L>5μm D~30nm	h-WO_3	Li_2WO_4	HCl	Li_2SO_4	180	24-48	[64]
Nanofiber L>5μm D~10nm	h-WO_3	$Na_2WO_4 \cdot 2H_2O$	HCl	K_2SO_4	180	12	[65]
Nanofiber L~1 μm D~100nm	h-WO_3	$Na_2WO_4 \cdot 2H_2O$	HCl	NaCl	180	24	[66]
Nanofiber L~1.5μm D~30nm	h-WO_3	$Na_2WO_4 \cdot 2H_2O$	HCl	$(NH_4)_2SO_4$	180	4	[67]
Nanoplate W~40nm T~25nm	$WO_3 \cdot 2H_2O$	$Na_2WO_4 \cdot 2H_2O$	I.E.	-	R.T	72	[53]
Nanorod L~700nm D~50nm	$WO_3 \cdot 0.33H_2O$	$Na_2WO_4 \cdot 2H_2O$	I.E.	-	180	24	[68]
Fine particles	$WO_3 \cdot 0.33H_2O$	$Na_2WO_4 \cdot 2H_2O$	I.E	-	200	2	[69]
Rectangular	m-WO_3	$Na_2WO_4 \cdot 2H_2O$	I.E	-	250-300	2	[69]

W: width, T: thickness, L: length, D: diameter

I.E.: Ion-exchanged method (Impurity-free acidified precursor can be prepared by passing Na_2WO_4 solution through a protonated cation-exchange resin)

1.3.2.2 Aqueous Sol-Gel method

The sol-gel method has been investigated for producing films consisting of WO_3 nanoparticles. This method generally starts with a precursor solution to form discrete particles or a network gel structure. During the course of gelation (aging), various forms of hydrolysis and polycondensation take place. The acidified precursor mentioned above is known to be an aqueous precursor for aqueous sol-gel method. However, the condensation process in this precursor is rather fast, resulting in large crystallites. Such precipitates are not convenient for the deposition of transparent thin films. Therefore, stabilizing or slow gelling at room temperature is preferable. This can be realized by adding H_2O_2 to form peroxotungstic acid solution. The peroxotungstic acid solution is also obtained by dissolving tungsten metal powder in H_2O_2 solution [70], and probably the most widely used precursor. A typical surface morphology of the WO_3 films obtained using peroxotungstic acid solution is consisted of WO_3 nanoparticles with 100-200 nm in size [71, 72]. Controlling the finer gain size may be possible by optimizing process conditions or adding appropriate additives.

1.3.2.3 Electrodeposition

The electro deposition can be considered the reverse of electrochemical anodization. For the electrodeposition of WO_3, the most popular choice of electrolyte is the peroxotungstic acid solution [73]. The electrodeposition of WO_3 from a peroxytungstate aqueous precursor was first reported by Yamanaka *et al.* [74, 75]. Typically the process requires only a small applied voltage (e.g.,-0.5 V versus Ag/AgCl) (potintiostate deposition), and the deposition duration is in the range of 1–30 min. [76]. By control process conditions, electrodeposition can produce porous WO_3 nanoparticle films with gains of 20-100 nm [76]. On the other hand, galvanostatic deposition route is also available. In the galvanostatic deposition route, the

effect of process parameters such as, concentration, pH value, and current density on the morphology and structure of WO_3 nanoparticle film has not been fully investigated.

1.4 Objective of this study

1.4.1 Objective

The hydrothermal treatment of the acidified solution, i.e., a tungstic acid solution (H_2WO_4) is a facile, inexpensive and green technique, which has the capability of producing WO_3 or $WO_3 \cdot nH_2O$ of different nanomorphologies. As mentioned above, the tungstic acid solution is generally prepared by acidification of Na_2WO_4 solution by mixing strong acids such as HCl, resulting in considerable coexistence of Na^+ and Cl^- ions. Sulfates and certain type of organic acids are also added as shape-directing agents. However, it is still unclear what exact polycondensation mechanisms are influenced by these additions. The residual Na is a persist contaminant in products. The contamination may result in negative effects on the performances of materials. An ion-exchanged precursor is an alternative acidified precursor, which is prepared by acidification only through a protonated cation-exchange resin. It contains intrinsically negligible amount of by-product ions, and therefore can be used as impurity-free precursor. Nevertheless, the hydrothermal treatment of ion-exchanged precursor has been less attention for synthesizing WO_3 nanoparticles.

In this study, therefore, the major objective is to study the structure control and characterization of WO_3 nanoparticles by hydrothermal treatment of an impurity-free ion-exchanged precursor. The ion-exchanged precursor was also applied to aqueous sol-gel method. For this purpose, stabilizing agents were added to the ion-exchanged precursor to prevent fast gelation and precipitation of the precursor. The effect of the stabilizing agents on the microstructures and electrochromic performance of the obtained WO_3 nanparticle films

were investigated. Additionally, WO_3 nanoparticle films were fabricated by galvanostatic electrodeposition method, and the effect of preparation parameters such as tungsten ions concentration, pH, current density and annealing on the properties and performance of WO_3 thin films electrochromic materials were investigated.

1.4.2 Scope of thesis

This thesis comprises 6 chapters. To clarify the background of this study and its objectives, Chapter 1 first introduced the various crystal structures, morphologies of WO_3 nanoparticles, their opportunities and their synthetic routes that have been presented in the literature to date.

In Chapter 2, a facile synthesis route of monoclinic WO_3 nanoplates via mild hydrothermal aging of ion-exchanged precursor was presented. The effects of mild hydrothermal conditions such as reaction temperature and time on the morphology and structure of $WO_3 \cdot nH_2O$ have been studied systematically. The important finding in this experiment was that the $WO_3 \cdot H_2O$ nanoplates precipitated predominantly under the mild aging (50°C) without any shape-directing additives, and the monoclinic WO_3 nanoplates were obtained by dehydration-induced topochemical transformation.

In Chapter 3, a facile synthesis route of hexagonal (h) WO_3 nanoneedles was presented. The schematic investigation revealed that $WO_3 \cdot 0.33H_2O$ nanoneedles grew predominantly under additive-free hydrothermal treatment of ion-exchanged precursor at 120°C. The h-WO_3 nanoneedles were then obtained by dehydration-induced topochemical transformation. The colloidal dispersibility of the nanoneeldes in aqueous medium was also investigated, aiming for assembling of nanoneedles.

In Chapter 4, a preparation and EC performance of WO_3 nanoparticle films were presented. A stabilized ion-exchanged precursor with H_2O_2 and oxalic acid was used. High

coloration efficiency of 64.2 cm^2/C was obtained for the open porous structure of the two-layer film prepared with W^+ ion concentration of 0.1 M, and 1% H_2O_2 and 4% oxalic acid.

In Chapter 5, an electrodeposition route for preparing WO_3 nanoparticle films and their EC performance were presented. The effect of preparation parameters such as tungsten ions concentration, pH, current density and annealing on the properties and performance of WO_3 thin films electrochromic materials was described.

In Chapter 6, the results obtained throughout this study were summarized.

References

[1] S. K. Deb, Applied Optics 8 (1969) 192-195.

[2] J. Kukkola, J. Mäklin, N. Halonen, T. Kyllönen, G. Tóth, M. Szabó, A. Shchukarev, J. P. Mikkola, H. Jantunen, K. Kordás, Sensors and Actuators B: Chemical 153 (2011) 293-300.

[3] T. Kida, A. Nishiyama, M. Yuasa, K. Shimanoe, N. Yamazoe, Sensors and Actuators B: Chemical 135 (2009) 568-574.

[4] K. Huang, Q. Zhang, Nano Energy 1 (2012) 172-175.

[5] J. Yang, W. Li, J. Li, D. Sun, Q. Chen, Journal of Materials Chemistry 22 (2012) 17744-17752.

[6] X. Liu, F. Wang, Q. Wang, Physical Chemistry Chemical Physics 14 (2012) 7894-7911.

[7] G. A. Niklasson, C. G. Granqvist, Journal of Materials Chemistry 17 (2007) 127-156.

[8] A. Karuppasamy, A. Subrahmanyam, Thin Solid Films 516 (2007) 175-178.

[9] Y. P. Xie, G. Liu, L. Yin, H. M. Cheng, Journal of Materials Chemistry 22 (2015) 6746-6751.

[10] X. Chen, Y. Zhou, Q. Liu, Z. Li, J. Liu, Z. Zou, ACS Applied Materials & Interfaces 4 (2012) 3372-3377.

[11] Z. Jiao, J. Wang, L. Ke, X.W. Sun, H.V. Demir, ACS Applied Materials & Interfaces 3 (2011) 229-236.

[12] Z. G. Zhao, M. Miyauchi, Angewandte Chemie International Edition 47 (2008) 7051-7055.

[13] D. N. Rajagopal, D Mangalaraj, Y. Djaoued, J. Robichaud, O. Y. Khyzhun, Nanoscale Research Letters 4 (2009) 8-14.

[14] K. Huang, Q. Pan, F. Yang, S. Ni, X. Wei, D. He, Journal of Physics D: Applied Physics 41(2008) 155417-155420.

[15] T. Stoycheva, S. Vallejos, C. Blackman, S. J. A. Moniz, J. Calderer, X. Correig, Sensors

and Actuators B: Chemical 161(2012) 406-413.

[16] X. Lu, X. Liu, W. Zhang, C. Wang, Y. Wei, Journal of Colloid and Interface Science 298 (2006) 996-999.

[17] H. Zhang, G. Duan, Y. Li, X. Xu, Z. Dai, W. Cai, Crystal Growth & Design 12 (2012) 2646-2652.

[18] J. Ma, J. Zhang, S. Wang, T. Wang, J. Lian, X. Duan, W. Zheng, The Journal of Physical Chemistry C 115 (20110) 18157-18163.

[19] L. Li, J. Zhao, Y. Wang, Y. Li, D. Ma, Y. Zhao, S. Hou, X. Hao, Journal of Solid State Chemistry 184 (2011) 1661-1665.

[20] S. J. Kim, I. S. Hwang, J. K. Choi, J. H. Lee, Thin Solid Films 519 (2011) 2020-2024.

[21] X. Su, F. Xiao, Y. Li, J. Jian, Q. Sun, J. Wang, Materials Letters 64 (2010) 1232-1234.

[22] D. J. Ham, A. Phuruangrat, S. Thongtem, J. S. Lee, Chemical Engineering Journal 165 (2010) 365-369.

[23] W. Xiao, W. Liu, X. Mao, H. Zhu, D. Wang, Journal of Materials Chemistry A 1 (2013) 1261-1269.

[24] L. Zhou, J. Zou, M. Yu, P. Lu, J. Wei, Y. Qian, Y. Wang, C. Yu, Crystal Growth & Design 8 (2008) 3993-3998.

[25] H. Wang, T. Lindgren, J. He, A. Hagfeldt, S. E. Lindquist, The Journal of Physical Chemistry B 104 (2000) 5686-5696.

[26] V. D. Vernardou, H. Drosos, E. Spanakis, E. Koudoumas, N. Katsarakis, M. E. Pemble, Electrochimica Acta 65 (2012) 185-189.

[27] A. I. Inamdar, Y. S. Kim, B. U. Jang, H. Im, W. Jung, D. Y. Kim, H. Kim, Thin Solid Films 520 (2012) 5367-5371.

[28] M. Deepa, R. Sharma, A. Basu, S. A. Agnihotry, Electrochimica Acta 50 (2005) 3545-3555.

[29] S. K. Deb, Solar Energy Materials and Solar Cells 9(2008) 245-258.

[30] H. Zheng, J. Z. Ou, M. S. Strano, R. B. Kaner, A. Mitchell, K. Kalantar-zadeh, Advanced Functional Materials 21 (2011) 2175-2196.

[31] P. M. Woodward, A. W. Sleight, T. Vogt, Journal of Solid State Chemistry 131 (1997) 9-17.

[32] B. Gerand, G. Nowogrocki, J. Guenot, M. Figlarz, Journal of Solid State Chemistry 29 (1979) 429-434.

[33] M. Figlarz, Progress in Solid State Chemistry 19(1989) 1-46.

[34] M. Deepa, P. Singh, S. N. Sharma, S. A. Agnihotry, Solar Energy Materials and Solar Cells 90 (2006) 2665-2682.

[35] D. Chen, L. Gao, A. Yasumori, K. Kuroda, Y. Sugahara, Small 4 (2008) 1813-1822.

[36] B. Gerand, , G. Nowogrocki, M. Figlarz, Journal of Solid State Chemistry 38 (1981) 312-320.

[37] C. Guéry, C. Choquet, F. Dujeancourt, J. M. Tarascon, J. C. Lassègues, Journal of Solid State Electrochemistry 1 (1997) 199-207.

[38] E. Ozkan, S. H. Lee, C. E. Tracy, J. R. Pitts, S. K. Deb, Solar Energy Materials and Solar Cells 79 (2003) 439-448.

[39] F. P. Koffyberg, K. Dwight, A. Wold, Solid State Communications 30 (1979) 433-437.

[40] Z. Ou, M. H. Yaacob, M. Breedon, H. D. Zheng, J. L. Campbell, K. Latham, J.d. Plessis, W. Wlodarski, K. Kalantar-zadeh, Physical Chemistry Chemical Physics 13 (2011) 7330-7339.

[41] L. Yang, D. Ge, J. Zhao, Y. Ding, X. Kong, Y. Li, Solar Energy Materials and Solar Cells 100 (2012) 251-257.

[42] C. K. Wang, D. Sahu, S. C. Wang, J. L. Huang, Ceramics International 38 (2012) 2829-2833.

[43] C. G. Granqvist, Applied Physics A 57 (1993) 3-12.

[44] Y. C. Nah, A. Ghicov, D. Kim, P. Schmuki, Electrochemistry Communications 10 (2008)

1777-1780.

[45] M. Shibuya, M. Miyauchi, Chemical Physics Letters 473 (2009) 126-130.

[46] C. Chananonnawathorn, S. Pudwat, M. Horprathum, P. Eiamchai, P. Limnontakul, C. Salawan, K. Aiempanakit, Procedia, Procedia Engineering 32 (2012) 752-758.

[47] X. Sun, Z. Liu, and H. Cao, Thin Solid Films 519 (2011) 3032-3036.

[48] Z. Dimitrova, D. Gogova, Materials Research Bulletin 40 (2005) 333-340.

[49] J. Thangala, S. Vaddiraju, R. Bogale, R. Thurman, T. Powers, B. Deb, M. K. Sunkara, Small 3 (2007) 890-896.

[50] J. M. O-Rueda de León, D. R. Acosta, U. Pal, L. Castañeda, Electrochimica Acta 56 (2011) 2599-2605.

[51] S. R. Bathe, P. S. Patil, Solar Energy Materials and Solar Cells 91 (2007) 1097-1101.

[52] S. Badilescu, P.V. Ashrit, Solid State Ionics 158 (2003) 187-197.

[53] Y. G. Choi, G. Sakai, K. Shimanoe, N. Miura, N. Yamazoe, Sensors and Actuators B: Chemical 87 (2002) 63-72.

[54] J. Livage, D. Ganguli, Solar Energy Materials and Solar Cells 68 (2001) 365-381.

[55] X. Li, J. Li, Q. Zhou, Z. Peng, G. Liu, T. Qi, Metallurgical and Materials Transactions B 4 (2012) 221-228.

[56] K. O. Iwu, A. Galeckas, P. Rauwel, A. Y. Kuznetsov, T. Norby, Journal of Solid State Chemistry 185 (2012) 245-252.

[57] J. Livage, G. Guzman, Solid State Ionics 84 (1996) 205-211.

[58] M. Gotić, M. Ivanda, S. Popović, S. Musić, Materials Science and Engineering: B 77 (2000) 193-201.

[59] C. Balázsi, J. Pfeifer, Solid State Ionics 151 (2002) 353-358.

[60] L. Seguin, M. Figlarz, and J. Pannetier, Solid State Ionics 63–65(1993) 437-441.

[61] F. Shiba, M. Yokoyama, Y. Mita, T. Yamakawa, Y. Okawa, Materials Letters 61 (2007) 1778-1780.

[62] X. Han, X. Han, L. Li, C. Wang, New Journal of Chemistry 36 (2012) 2205-2208.

[63] H. F. Pang, X. Xiang, Z. J. Li, Y. Q. Fu, X. T. Zu, physica status solidi (a) 209 (2012) 537-544.

[64] Z. Gu, H. Li, T. Zhai, W. Yang, Y. Xia, Y. Ma, J. Yao, Journal of Solid State Chemistry 180 (2007) 98-105.

[65] X. C. Song, Y. F. Zheng, E. Yang, Y. Wang, Materials Letters 61 (2007) 3904-3908.

[66] J. Wang, E. Khoo, P.S. Lee, J. Ma, The Journal of Physical Chemistry C 113 (2009) 9655-9658.

[67] J. Zhang, J. Tu, X. Xia, X. L. Wang, C. Gu, Journal of Materials Chemistry 21 (2011) 5492-5498.

[68] R. F. Mo, G. Q. Jin, X. Y. Guo, Materials Letters 61 (2007) 3787-3790.

[69] H. Kominami, K. I. Yabutani, T. Yamamoto, Y. Kera, B. Ohtani, Journal of Materials Chemistry 11 (2001) 3222-3227.

[70] J. Shi, G. Hu, R. Cong, H. Bu, N. Dai, New Journal of Chemistry 37 (2013) 1538-1544.

[71] M. Deepa, A. K. Srivastava, S. N. Sharma, Govind, S. M. Shivaprasad, Applied Surface Science 254 (2008) 2342-2352.

[72] A. K. Srivastava, M. Deepa, S. Singh, R. Kishore, S. A. Agnihotry, Solid State Ionics 176 (2005) 1161-1168.

[73] T. Pauporté, Journal of The Electrochemical Society 149 (2002) C539-C545.

[74] K. Yamanaka, H. Oakamoto, H. Kidou, T. Kudo, Jpn. J. Appl. Phys. 25 (1986) 1420-1426.

[75] K. Yamanaka, Jpn. J. Appl. Phys. 26 (1987) 1884-1890.

[76] Z. Yu, X. Jia, J. Du, J. Zhang, Solar Energy Materials and Solar Cells 64 (2000) 55-63.

Chapter 2

Synthesis of Monoclinic WO_3 Nanoplates via Mild Aging of Ion-Exchanged Precursor

Abstract

A facile method to synthesize $WO_3 \cdot H_2O$ square nanoplates via a mild hydrothermal aging (50˚C) of ion-exchanged precursor was developed. The ion-exchanged precursor was prepared by passing the sodium tungstate solution (Na_2WO_4) through a protonated cation-exchange resin, and used as impurity-free acidified precursor for synthesizing $WO_3 \cdot H_2O$ nanoplates. No shape-directing additive was employed. The effects of mild hydrothermal conditions such as reaction temperature and time on the morphology and structure of $WO_3 \cdot nH_2O$ have been studied systematically. The $WO_3 \cdot H_2O$ with an orthorhombic structure and platelet-like morphology was synthesized at 50 °C for 8 h. The morphological evolution to square platelet proceeded with an increase of aging time. After aging for 24 h, the $WO_3 \cdot H_2O$ square nanoplates were predominantly synthesized. The square nanoplates consisted of a few or several stacked thin layers (thickness, ~10nm/layer), and provided the well-defined {010} facet for two dominantly exposed surfaces and {101} side facets. Their lateral dimension reached several hundreds of nanometers. In addition, the monoclinic WO_3 nanoplates were successfully obtained by dehydration-induced topochemical transformation of the $WO_3 \cdot H_2O$ nanoplates. It is thus demonstrated that the mild aging (50 °C) of the ion-exchanged precursor is a simple and impurity-free synthetic route for $WO_3 \cdot H_2O$ nanoplates and monoclinic WO_3 nanoplates.

2.1 Introduction

Recently, synthetic strategy for nanostructures of $WO_3 \cdot nH_2O$ and their dehydrated WO_3 has been focused subject due to the interest in both fundamental science and technological applications [1-3]. Among various nanostructures, two-dimensional nanopalates have received much attention, because the nanoplates not only can provide active sites for catalysis and sensors [4-6] but also can be used as building blocks to construct complex nanostructures. To date, hydrothermal treatment of the acidified precursor with assistance of shape-directing additives has been widely investigated for synthesizing the nanoplates [6-10]. The acidified precursor is prepared by adding strong acids into a sodium tungstate solution (Na_2WO_4); different crystalline structures as well as morphologies may occur, depending on the processing conditions [11]. However, under the utilization of the acidified precursor, the unavoidably contaminated cations such as Na^+ in the final products may result in negative effects on the performances of materials [12, 13].

An ion-exchanged precursor is an alternative acidified precursor [14], which is prepared by acidification only through a protonated cation-exchange resin. It contains intrinsically negligible amount of by-product ions such as Na^+ and Cl^- and therefore can be used as impurity-free precursor [15, 16]. It can be also expected that the crystalline $WO_3 \cdot nH_2O$ such as $WO_3 \cdot 2H_2O$ and $WO_3 \cdot H_2O$ would be formed with platelet-morphologies, according to the two-dimensional condensation reaction in the acidified solution (H_2WO_4) [14, 17, 18]. Nevertheless, there are only a few studies reported on the formation of $WO_3 \cdot nH_2O$ nanoplates in the ion-exchanged precursor. Choi et al. [16] stated that the ion-exchanged precursor became rapidly turbid, then a gel was formed and transformed into precipitated $WO_3 \cdot 2H_2O$ nanoparticles (about 30nm in

diameter) after three days at room temperature. They found that the precipitates further grew up to be nanoplate morphology by the post-treatments of centrifuging [19], ultrasonic agitation [16] and mixing polyethylene glycol as a shape-director additive [20]. However, their process needs long route to obtain the nanoplates, and the effect of the process conditions on the morphological evolution has still remained unclear. On the other hand, the hydrothermal treatment (>100 °C) promoted rather one-dimensional products like nanorods [21]. To our knowledge, there have been few efforts to investigate the effect of intermediate or mild aging condition (<100 ℃) on morphology and structure of $WO_3 \cdot nH_2O$ precipitated in the ion-exchanged precursor.

In this chapter, we present a facile and one-pot route to synthesize the square nanoplates of tungsten monohydrous oxide via a mild aging of the ion-exchanged precursor, without any shape-directing additives. As shown later, it was found that the $WO_3 \cdot H_2O$ with an orthorhombic structure and platelet-like morphology was synthesized at 50 °C for 24 h. We expect that the synthetic strategy with such a low temperature will receive some benefits as inexpensive and versatile techniques. By using this route, the effect of aging time on the morphological and structural evolution of $WO_3 \cdot H_2O$ nanoplates was investigated. In addition, the $WO_3.H_2O$ nanoplates were converted to WO_3 particles by annealing, and their morphology and structure were evaluated.

2.2. Experimental

2.2.1 Materials

Sodium tungstate dihydrate ($Na_2WO_4 \cdot 2H_2O$, >99%) was purchased from Kanto Chemicals Co. (Japan) and used without further purification. Strong acid type of Diaion

PK228LH cation exchange resin (ion-exchange capacity >2.05 meq/ml) was supplied from Mitsubishi Chemical Co. (Japan). Deionized water (18.2MΩcm) from Sartorius-arium®61316 system (Germany) was used throughout the experiments. A glass column with height of 150 mm and 24.6 mm in diameter was used for the ion-exchange process. The glass column was packed with 30mL of the ion-exchange resin, and then 10 mL of water was passed through the column to wash the resin. This washing step was repeated five times before the experiment.

2.2.2 Sample preparation

0.5M Na_2WO_4 solution was prepared by dissolving $Na_2WO_4{\cdot}2H_2O$ powder in deionized water. Then, a 10 mL of the solution was loaded on the glass column, and the acidified tungstic acid (H_2WO_4) solution was recovered from the column by elution with deionized water. The resulting solution was yellowish and transparent. The present ion-exchange treatment was performed in the temperature-controlled chamber at 15°C. The concentration of H_2WO_4 was determined to be 0.23 M by X-ray fluorescence spectroscopy (EDX-800, Shimazu, Japan). The Na^+ concentration was determined to be 1.7 ±0.6 ppm (n=3) by inductively coupled plasma atomic emission spectrometry (ICP-AES, Optima 4300DV, Perkinelmr). This ion-exchanged precursor was aged under different temperatures (30, 40, 50, 60 and 80 °C) and times (8, 16, 24 and 168 h). No additive was used in this experiment. After aging, the precipitated powder was collected for morphological and structural examinations. Furthermore, WO_3 nanoparticles were synthesized by annealing the $WO_3{\cdot}nH_2O$ samples at 350 °C in air for 1 h.

2.2.3 Sample characterizations

The crystallographic phase of the samples was determined by powder X-ray diffraction (XRD; Ultima IV, Rigaku, Japan, Cu-Kα radiation). Their morphology was examined by scanning electron microscopy (SEM; JSM 6010LA, JEOL, Japan) and atomic force microscopy (AFM; NanoNavi Station, SII, Japan). Their microstructures were also observed by transmission electron microscopy (TEM; JEM-2100F, JEOL, Japan). The weight loss of the precipitate was measured by a thermogravimetric analysis (TG; TG/DTA 6200, SII, Japan). The structural property of WO_3 obtained by annealing the $WO_3 \cdot H_2O$ sample was evaluated by XRD and TEM analyses. The phase evolution was observed by high temperature X-Ray diffraction (HT-XRD) analysis which was conducted by using an instrument of Multiflex (CuKα, 40 kV, 40 mA, Rigaku Co.) in the range between room temperature and 500° C in air with a 0.02^o step. Each XRD pattern was acquired after 5 min holding at each temperature. The samples were mounted on a platinum plate.

2.3 Results and discussion

2.3.1 Synthesis of $WO_3 \cdot H_2O$ square nanoplates

The ion-exchanged precursor was yellowish and transparent as shown in Fig.2.1 (a). After aging at 50 °C for 24 h, yellow precipitates were obtained as shown in Fig.2.1 (b). The similar appearance was observed for the samples aged at 30, 40 and 60 °C. On the other hand, after aging at 80 °C for 24 h, not only the yellow but also white precipitates were observed as shown in Fig.2.1 (c).

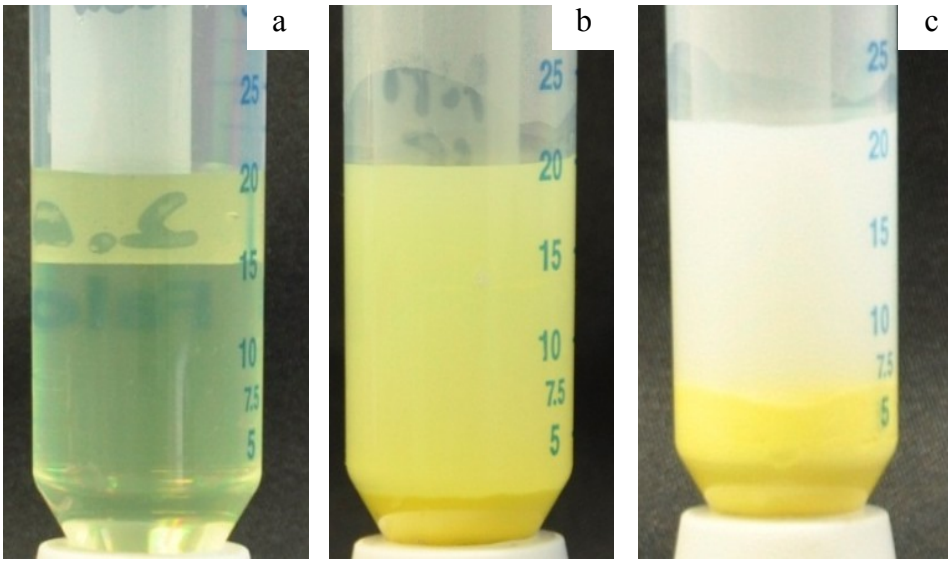

Fig. 2.1 Photographs of (a) ion exchange precursor, (b) the precipitate after aging at 50 ^{o}C for 24 h and (c) after aging at 80 ^{o}C for 24 h.

Under aging at room temperature (30 ^{o}C), the crystal growth of flake-like morphology was observed as shown in Fig.2.2 (a). The crystal phase of these particles was mainly monoclinic $WO_3 \cdot 2H_2O$ ($H_2WO_4.H_2O$, ICDD Card No. 00-018-1420), containing orthorhombic $WO_3 \cdot H_2O$ (ICDD Card No. 00-043-0679) as secondary phase (see Fig.2.2 (b)). These observations are similar to those reported previously [16].

Figure 2.3 shows the XRD patterns of the precipitates obtained after aging for 24 h at different aging temperatures (40, 50, 60 and 80 ^{o}C). When the reaction was conducted at 40 and 50°C, all peaks were indexed to the orthorhombic $WO_3 \cdot H_2O$ with a space group of Pmnb (62) and lattice parameters a= 5.2380 Å, b= 10.7040Å, c=5.1200 Å (ICDD Card No. 00-043-0679). With temperature increasing to 60° C, besides the main peaks due to the $WO_3 \cdot H_2O$, secondary peaks originating from the orthorhombic $WO_3 \cdot 0.33H_2O$ phase (ICDD No.01-072-0199) were detected. Further enhancing the reaction temperature to 80°C, the intensity of the secondary peaks increased.

Figure 2.4 shows the SEM images of precipitates after aging at 40, 50, 60 and 80 ^{o}C for 24h. The samples aged at 40 and 50 ^{o}C are composed of a large quantity of nanoplates. On the other hand, the samples aged at 60 and 80 ^{o}C contain also small particles. These particles may be due to formation of the secondary phase (see Fig. 2.(c), (d)). These results indicate that the aging temperature plays a crucial role in controlling the crystal structure and morphology of the precipitated tungsten oxide hydrates.

Figure 2.5 shows the XRD patterns of the precipitates obtained by aging the tungstic acid precursor at 50 ^{o}C for different times of 8, 16, 24, and 168 h. All peaks in the four XRD patterns were indexed to the orthorhombic $WO_3 \cdot H_2O$ phase with space group of Pmnb (62) and lattice parameters a = 5.2380, b = 10.7040, c = 5.1200 (ICDD Card No. 00-043-0679). No secondary phase was detected for all samples.

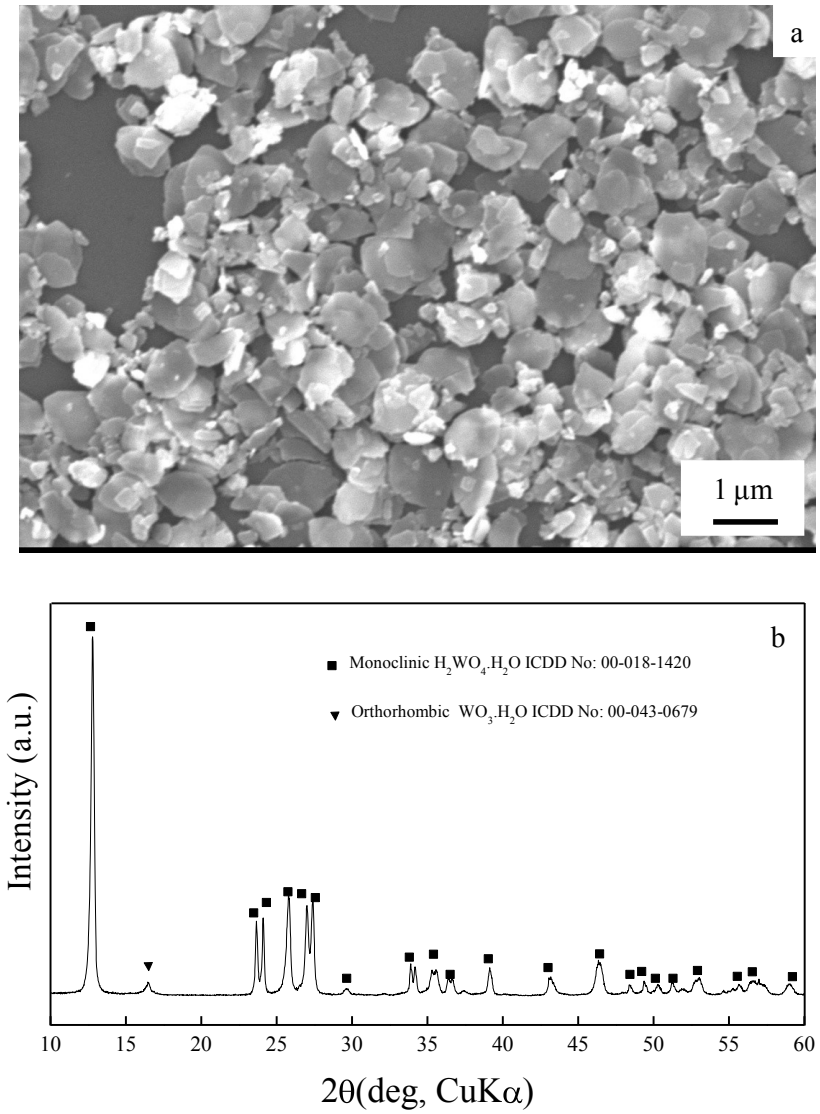

Fig. 2.2 (a) SEM image and (b) XRD patterns of as-prepared tungsten oxide hydrate aged at 30 ^{o}C for 72 h.

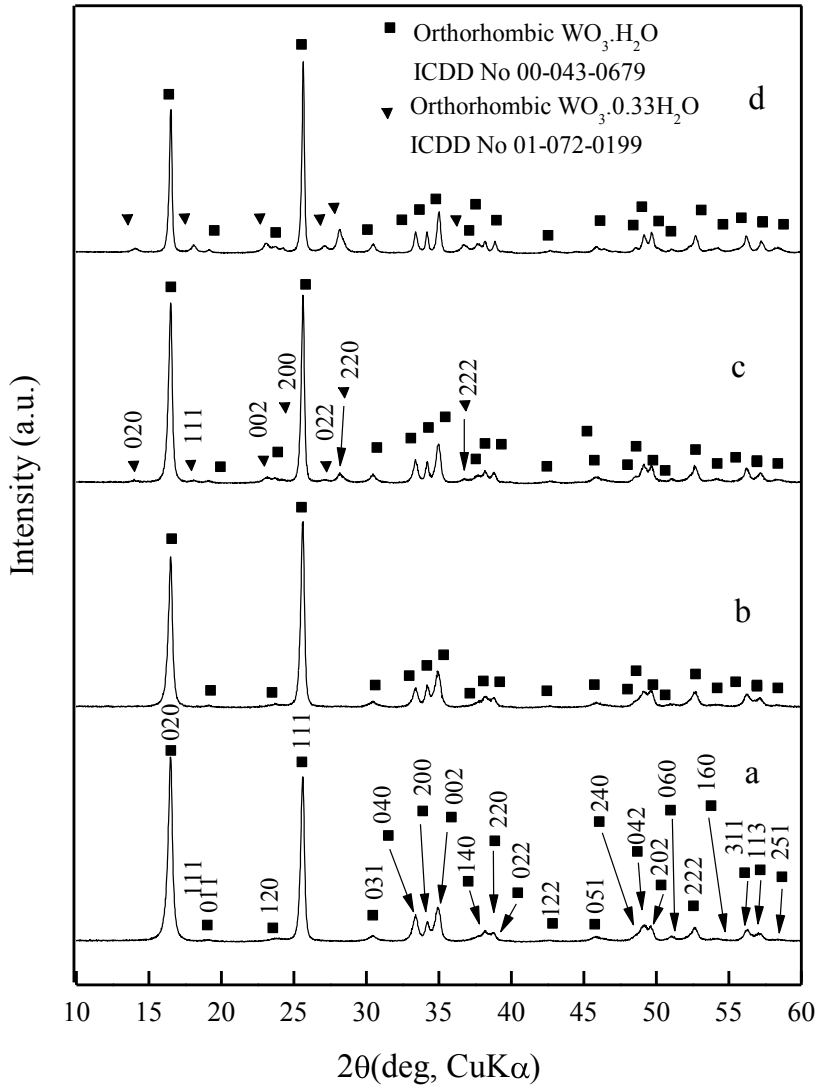

Fig. 2.3 XRD patterns of as-prepared tungsten oxides aged for 24 h at (a) 40 ^{o}C, (b) 50 ^{o}C, (c) 60 ^{o}C and (d) 80 ^{o}C.

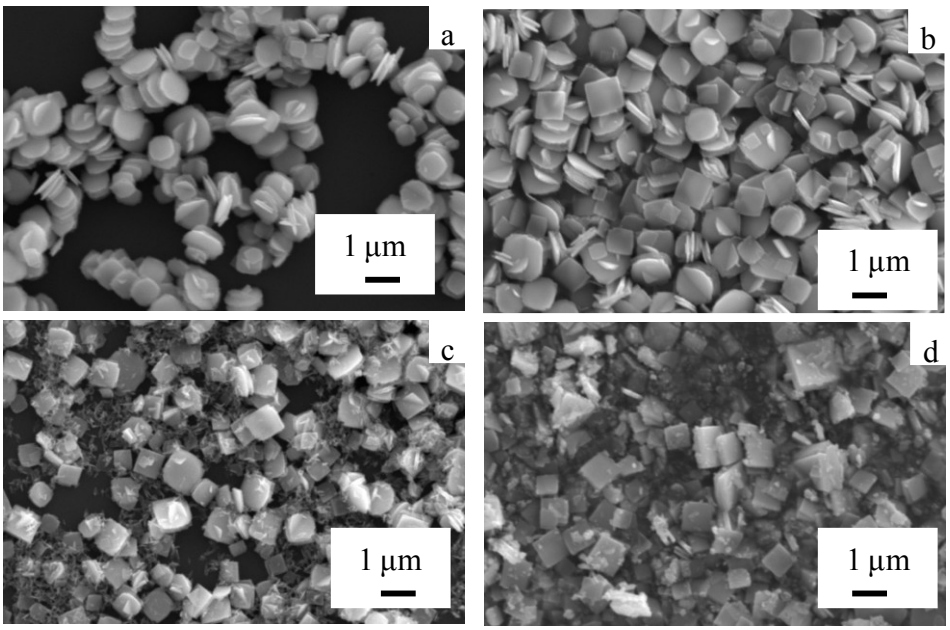

Fig. 2.4 SEM images of as-prepared tungsten oxide hydrates aged for 24 h at (a) 40 ^{o}C, (b) 50 ^{o}C, (c) 60 ^{o}C and (d) 80 ^{o}C.

It should be noted that the intensity ratio of (020) to (111) reflection peaks increased with an increase of the aging time, suggesting that the products show a preferential orientation of the (020) crystal plane.

Figure 2.6 shows the SEM images of the $WO_3 \cdot H_2O$ samples obtained after aging time of 8, 16, 24 and 168 h. It is revealed that all samples are composed of a large quantity of nanoplates. The size of the nanoplates did not significantly increase with an increase of aging time, even after prolonging aging time to 168 h and it was of several hundreds of nanometers. On the other hand, the morphology of the particles changes from relatively round shape (8 h) to square shape with increase of aging time. The present observation indicates that the aging time plays an important role on the formation of $WO_3 \cdot H_2O$ square nanoplates, and a suitable reaction time was 24 h and more.

Figure 2.7(a) shows a typical TEM image of the square nanoplates obtained after aging time of 24 h. The square nanoplates were clearly observed from the TEM image. The lateral dimension of the nanoplates reached several hundreds of nanometers. Figure 2.7(b) is a typical set of TEM image and the corresponding SAED pattern. All other nanoplates also showed the identical SAED pattern which can be assigned to a phase of single crystalline of the orthorhombic $WO_3 \cdot H_2O$ located along the [010] zone axis, revealing that it provides the well-defined {010} facet for two dominantly exposed surfaces. In addition, the [101] and $[10\bar{1}]$ directions are almost perpendicular to adjacent sides of the square nanoplates, indicating the nanoplates are enclosed by {101} facets on four sides. From these observations, it can be concluded that the $WO_3 \cdot H_2O$ precipitated grows preferentially along to {010} plane and eventually is enclosed by {101} side facets to form square platelets under aging at 50 °C.

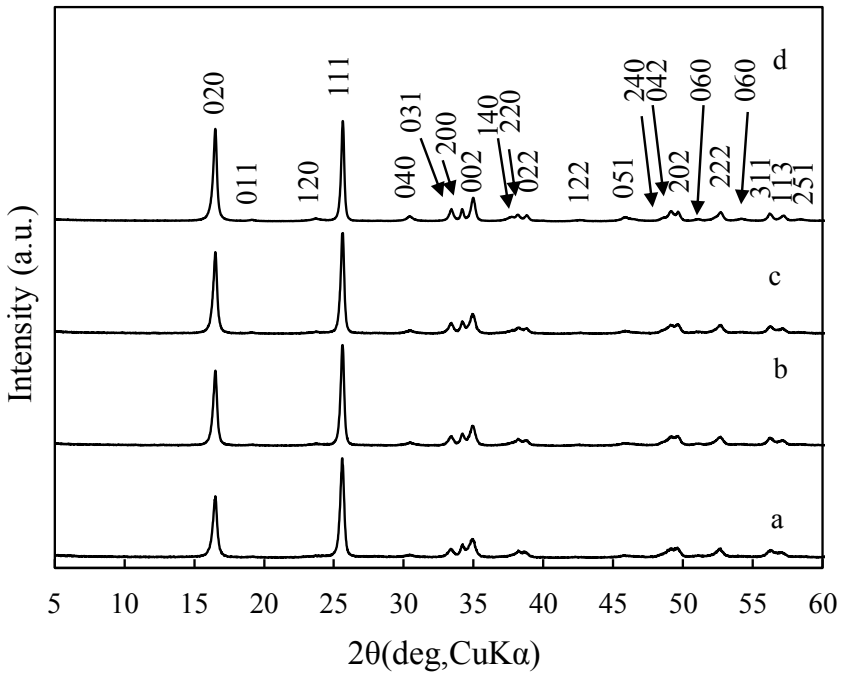

Fig. 2.5 XRD patterns of as-prepared tungsten oxide aged at 50 ^{o}C for (a) 8 h, (b) 16 h, (c)24 h and (d) 168 h. (all peaks can be indexed to $WO_3 \cdot H_2O$ (ICDD No. 00-043-0679)).

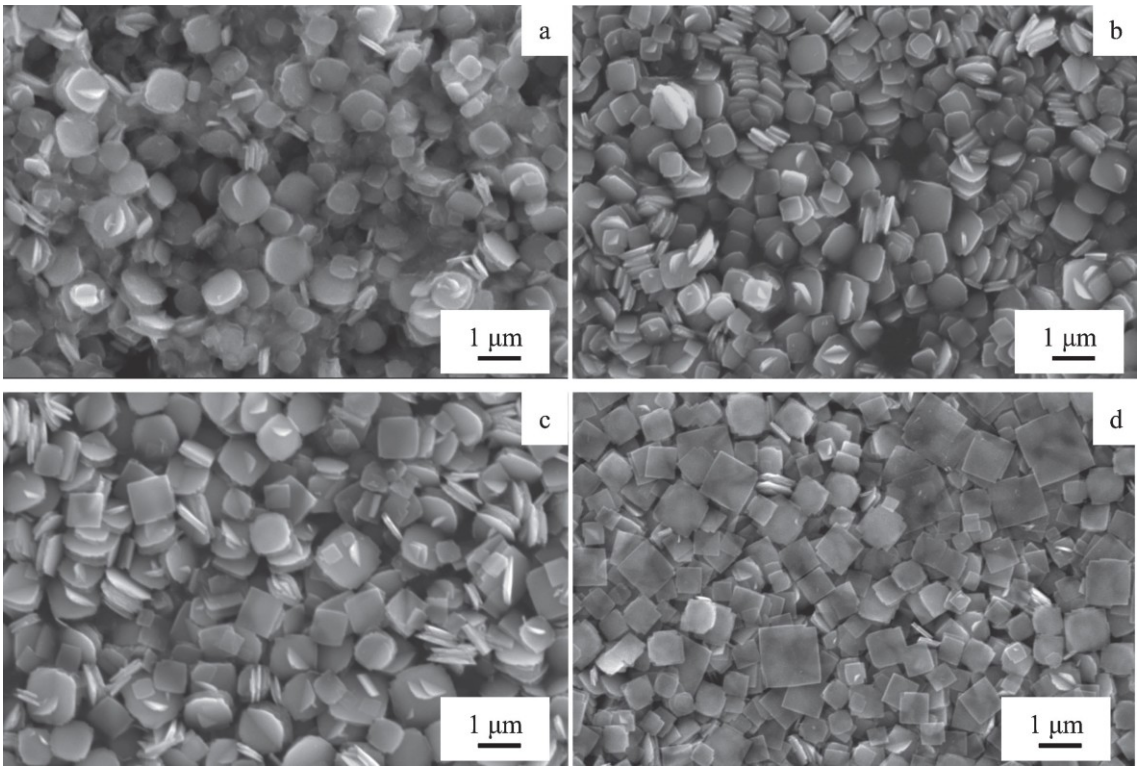

Fig. 2.6 SEM images of $WO_3 \cdot H_2O$ nanoplates aged at 50 °C for (a) 8 h, (b) 16 h, (c) 24 h and (d) 168 h.

Figure 2.7(d) and (e) shows highly magnified images of the $WO_3 \cdot H_2O$ nanoplates. It can be seen that these nanoplates are not monolayer, but consisted of a few or several stacked nanosheets.

Figure 2.8(a) and (b) shows an AFM image of a $WO_3 \cdot H_2O$ nanoplate and the cross-sectional profile corresponds to the line drawn in (a), respectively. The observed topographical feature along the line suggests that the at least three thin layers stacked and each layer is of around 10 nm in thickness.

In this study, we focused on the mild aging for controlling morphology and structure of the precipitates in the ion exchanged precursor. Both of crystalline phase and morphological structures were affected by aging conditions, and it was demonstrated that the $WO_3 \cdot H_2O$ square nanoplates were successfully synthesized. In the previous studies, the precipitates were often obtained under aging at room temperature [14, 16] and they were identified as $WO_3 \cdot 2H_2O$. On the other hand, hydrothermal treatment (180 °C for 24 h) promoted rather one-dimensional crystal growth, resulting in the hexagonal WO_3 and $WO_3 \cdot 0.33H_2O$ with nanorod morphology. It is thus proven that the aging at 50 °C is adequate to synthesize the $WO_3 \cdot H_2O$ square nanoplate in the impurity-free acidified precursor.

Since the present ion-exchanged precursor contained negligible amount of impurity-ions and no shape-directing additives, i.e., contained no extra species which may influence crystal growth, the observed preferential growth of $WO_3 \cdot H_2O$ along to {010} plane can be explained from the intrinsic growth habit of $WO_3 \cdot H_2O$ as follow:

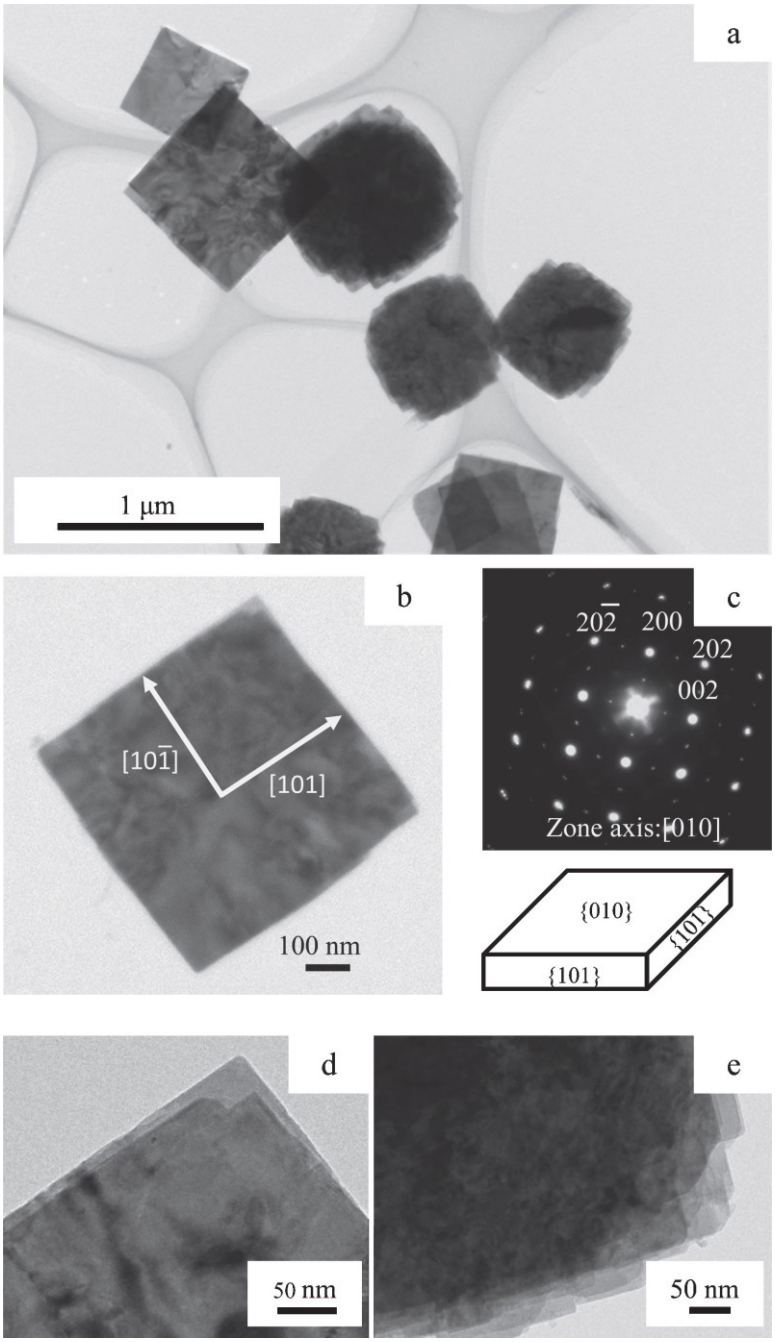

Fig. 2.7 (a) TEM images of $WO_3 \cdot H_2O$ nanoplates, (b, c) TEM image of $WO_3 \cdot H_2O$ nanoplate and its corresponding SAED pattern, with crystal model of the nanoplate, (d, e) magnified TEM images of the edge of $WO_3 \cdot H_2O$ nanoplates.

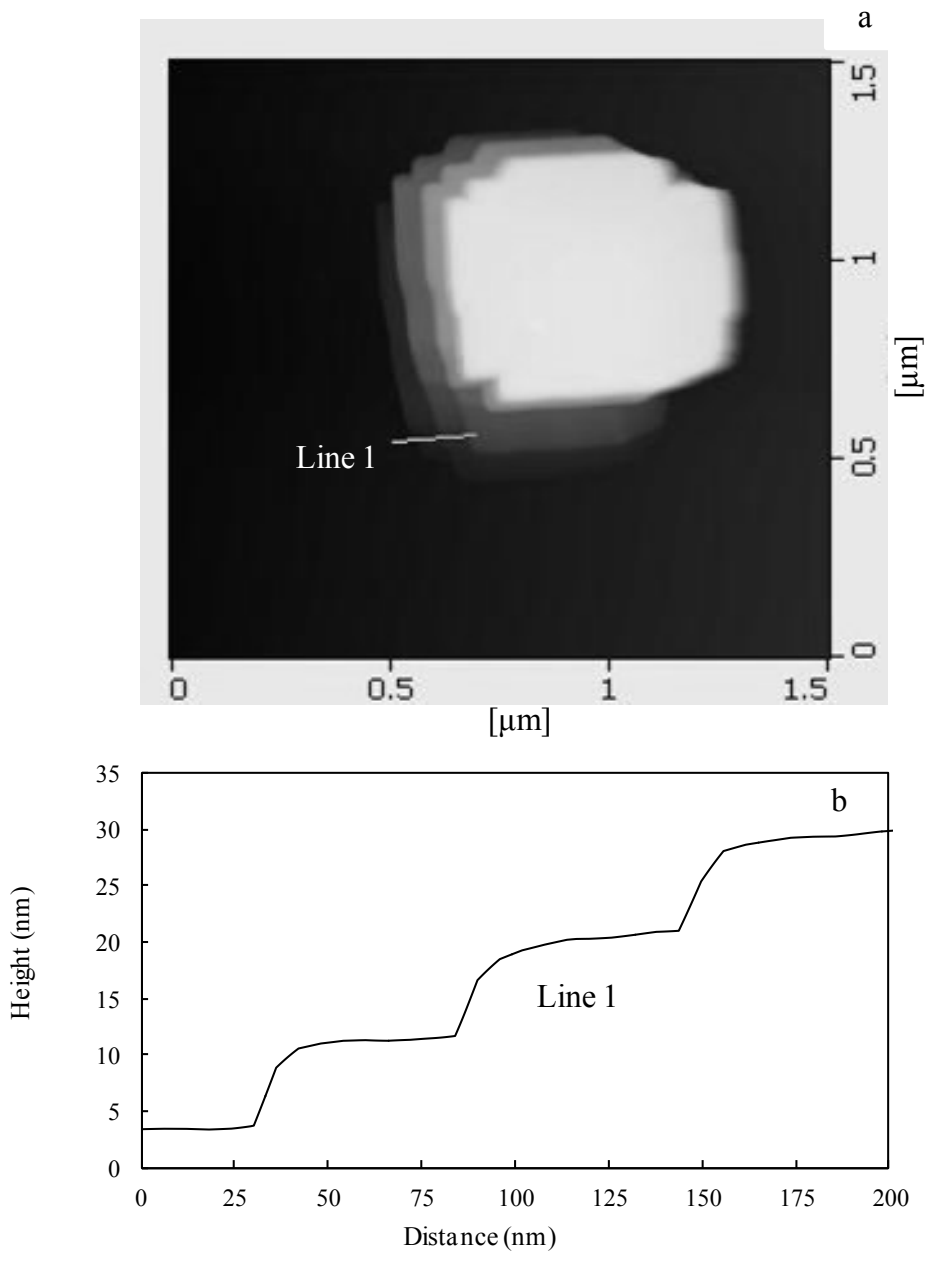

Fig. 2.8 (a) AFM image of a $WO_3 \cdot H_2O$ nanoplate and (b) Height profile along "line 1" in (a).

At the initial period of aging, the intermediate [$WO(OH)_4(OH_2)$] are formed in acidified solution (H_2WO_4) [7, 14], where one water molecule is bonded along to the b-axis opposite to the W=O bond while the four OH groups are in the equatorial a-c plane. Then, the intermediates condense to form a [$WO_5(OH_2)$] octahedral layer through oxolation reaction along to the equivalent a- and c- directions, i.e., along to {010} plane [7, 14, 18] (see Fig. 2.9). The [$WO_5(OH_2)$] octahedral layers are bonded to each other by hydrogen bonds between the terminal oxygen and coordinated water molecules in neighboring layers, leading to the formation of a layered and platelet $WO_3 \cdot H_2O$ structure. From the above consideration, the present aging temperature definitely promotes the two-dimensional oxolation reaction, i.e., extending [$WO_5(OH_2)$] octahedral layer which cause the formation of nanoplatelets [21]. However, the detailed mechanism for formation of $WO_3 \cdot H_2O$ square nanoplates needs to be further explored.

2.3.2 Dehydration behavior of $WO_3 \cdot H_2O$ square nanoplates

Figure 2.10 shows the weight loss behavior of the $WO_3 \cdot H_2O$ nanoplates for temperatures from 25 and 500 °C measured by TGA. From the figure, it is clear that the $WO_3 \cdot H_2O$ nanoplates had an obvious weight loss around 200 °C. The weight loss is almost completed at 300 ^oC. The amount of the structural water of the precipitate can be calculated from the weight loss difference between 150 and 500°C, with taking account of physically adsorbed water. As a result, it corresponded to about $1H_2O$ per mole of WO_3.

Figure 2.11 shows the HT-XRD pattern of the obtained tungsten oxide hydrates. The XRD pattern recorded at room temperatures represented only a single phase of orthorhombic $WO_3 \cdot H_2O$. No phase change occurred up to 150 ^oC.

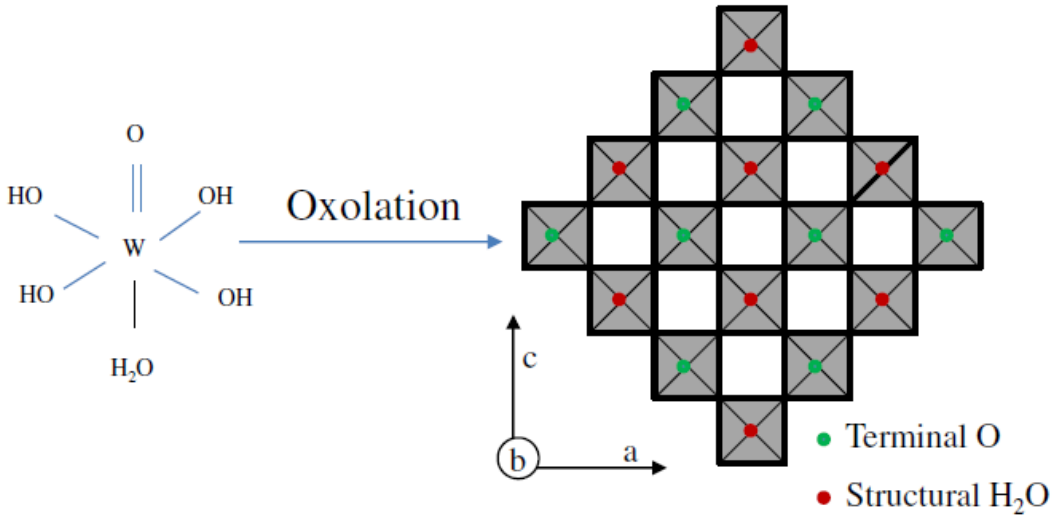

Fig. 2.9 Schematic illustration of the formation of $[WO_5(OH_2)]$ octahedral monolayer from the neutral precursor $[WO(OH)_4(OH_2)]$.

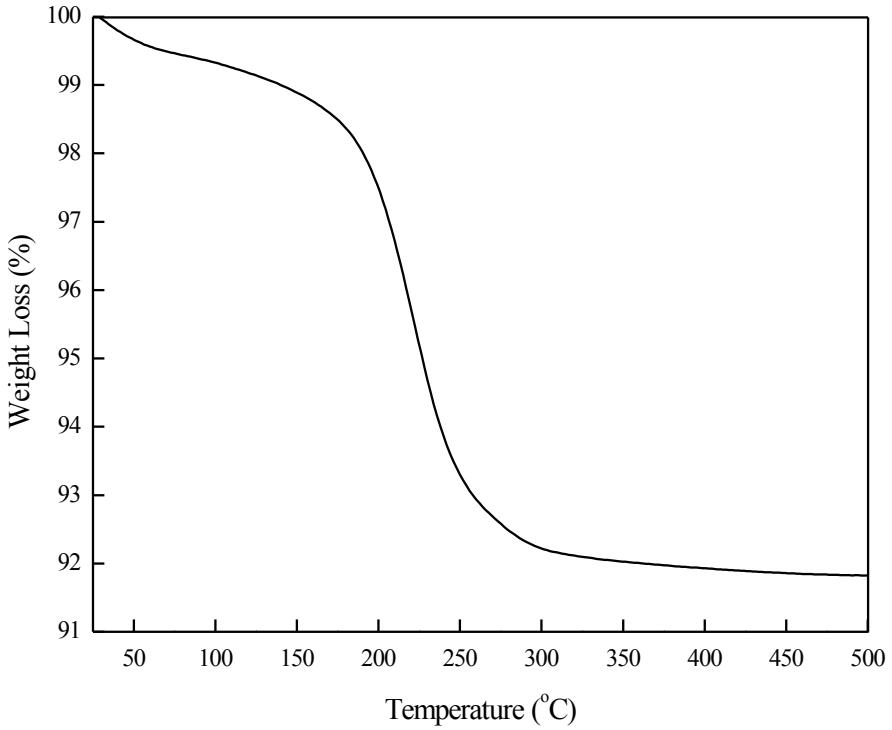

Fig. 2.10 TGA curve of $WO_3 \cdot H_2O$ nanoplates.

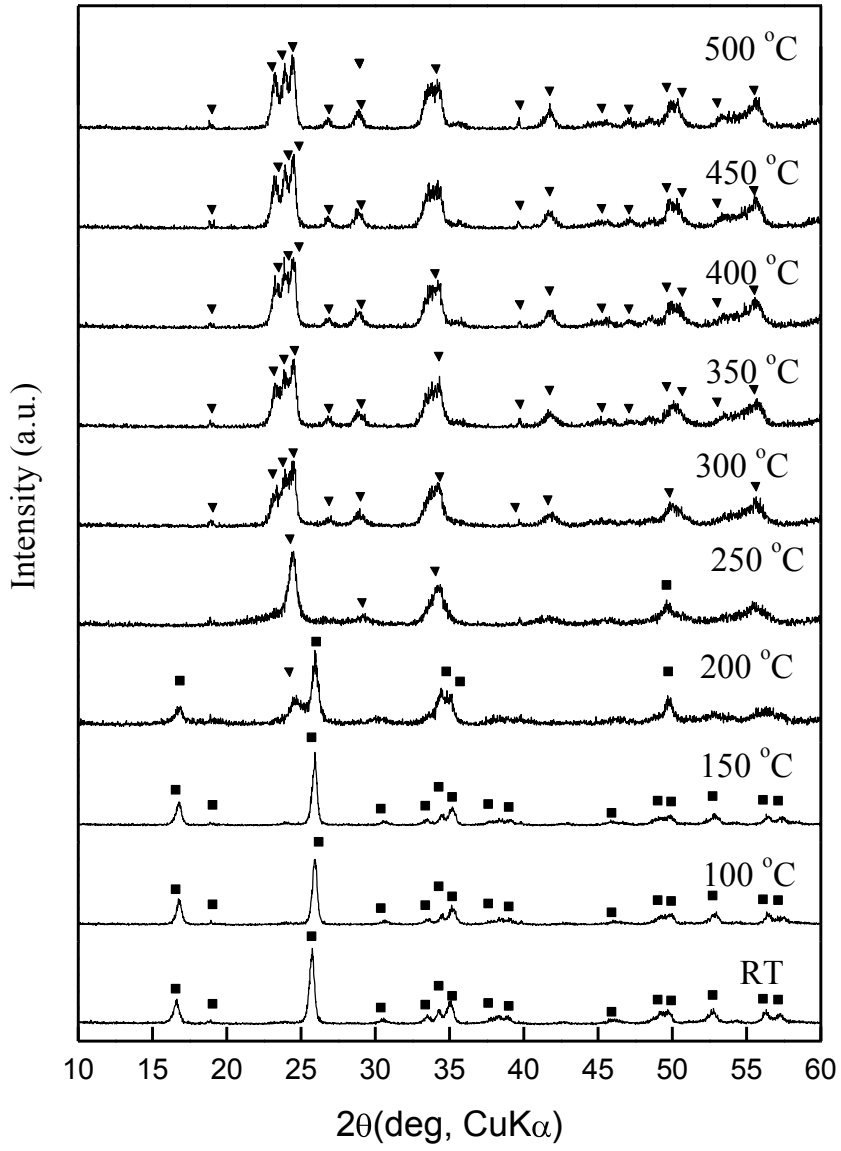

Fig. 2.11 HT-XRD patterns of as-prepared tungsten oxide aged at 50 °C for 24 h recorded from room temperature to 500 °C.

Peaks marked with ■ can be indexed to orthorhombic $WO_3 \cdot H_2O$ (ICDD No: 00-043-0679), while peaks marked with ▼ can be indexed to monoclinic WO_3 (ICDD No: 01-072-0677).

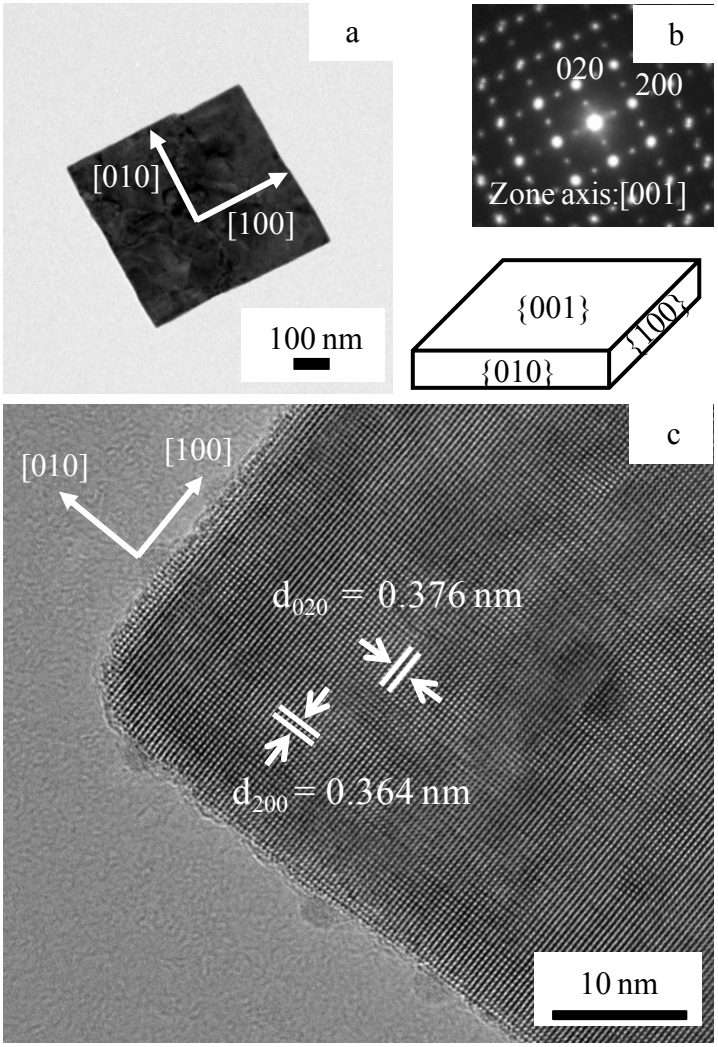

Fig. 2.12 (a, b) TEM images of WO_3 nanoplate and its corresponding SAED pattern, with crystalline model of the nanoplate and (c) HRTEM image of WO_3 nanoplate.

The phase transformation started by annealing the sample at 200 ^{o}C. The XRD pattern recorded at 300 ^{o}C presented a single phase of monoclinic WO_3. No phase change occurred up to 500 ^{o}C. From these results, it could be concluded that the dehydration of $WO_3 \cdot H_2O$ nanoplates started at temperature around 200 ^{o}C and completed at 300 ^{o}C.

Figure 2.12 (a) and (b) show a typical TEM image and its corresponding SAED pattern of one of the annealed WO_3. As shown in the figure, the WO_3 square nanoplate was formed from the $WO_3 \cdot H_2O$ nanoplate without obvious morphological change. In the corresponding SAED pattern, the uniform, wide and ordered diffraction spots can be assigned to a phase of single-crystal monoclinic WO_3 located along the [001] zone axis. Since the WO_3 nanoplate is lying flat on the TEM grid, the thickness of the WO_3 nanoplate is definitely the [001] direction. [100] and [010] directions are almost perpendicular to adjacent sides of the square. These observations reveal that the dehydrated WO_3 square nanoplate provides the well-defined {001} facet for two dominantly exposed surfaces with {100} and {010} side facets. Figure 2.12 (c) shows HRTEM image of the edge of the WO_3 nanoplate. The clear two dimensional ordered lattice fringe means that the obtained WO_3 nanoplate is a single crystal. The interplanar distance values of 0.364 and 0.376 nm can be assigned to the (200) and (020) crystal planes of monoclinic WO_3, respectively. During the annealing, the coordinated water molecules between the $[WO_5(OH_2)]$ octahedral layers in $WO_3 \cdot H_2O$ nanoplates were driven out to stabilize the system three-dimensionally and monoclinic WO_3 began to form. The morphology of square nanoplate could be maintained during the dehydration process, which is considered to be a topotactic process.

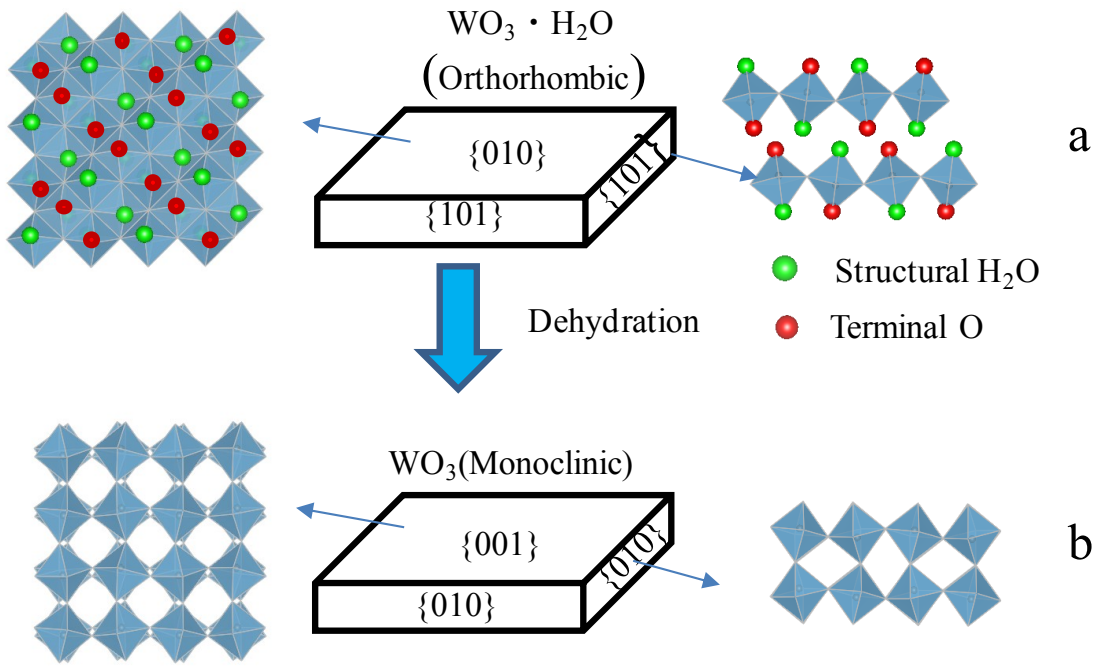

Fig. 2.13 A schematic representation of (a) orthorhombic $WO_3 \cdot H_2O$ nanoplate transferring to (b) monoclinic WO_3 via a dehydration process (Topotactic transformation).

The structural evolution of [010] oriented $WO_3 \cdot H_2O$ nanoplates to [001] oriented WO_3 nanoplates can be simply explained by the crystallographic topotaxy, based on their similarity of the WO_6 octahedral layers in both $WO_3 \cdot H_2O$ and WO_3 [9]. The condensation process from $WO_3 \cdot H_2O$ nanoplates to monoclinic WO_3 nanoplates is shown in Fig. 2.13 (a) and (b). For $WO_3 \cdot H_2O$ nanoplates, the $[WO_5 (OH_2)]$ octahedral layers extend in the ac-plane, and the thickness direction is the b-axis. These octahedral layers are bonded to each other by hydrogen bonds between O and H atoms in neighboring layers. At an elevated temperature (such as 350 ^oC), the hydrogen bonds between two neighboring $[WO_5 (OH_2)]$ octahedral layers are replaced by W–O–W bonds to form a W–O–W network structure, accompanying the release of crystal water molecules. Finally, the monoclinic WO_3 phase, the most stable phase of tungsten oxides, was formed. It should be noted that the 2D plate-like morphology of $WO_3 \cdot H_2O$ nanocrystals is maintained during the course of dehydration, and the resultant WO_3 nanocrystals take on a similar plate-like shape with a thickness along the c-axis. The similar dimensionalities also suggest that the condensation from $WO_3 \cdot H_2O$ nanoplates to WO_3 nanoplates is a topotactic process [24].

2.4. Conclusions

We have investigated the effect of mild aging (50 °C) on the morphology and structure of $WO_3 \cdot nH_2O$ precipitated in the ion-exchanged precursor without any shape-directing additives, and found that the $WO_3 \cdot H_2O$ square nanoplates can be synthesized for 24 h. The nanoplates consisted of stacked thin nanosheets (~10 nm) which provided the well-defined {010} facet for two dominantly exposed surfaces. The lateral dimension of the nanoplates reached several hundreds of nanometers. In addition, WO_3 nanoplates were successfully obtained by dehydration induced topochemical transformation of $WO_3 \cdot H_2O$ nanoplates at 350 °C in air. The obtained $WO_3 \cdot H_2O$ square nanoplates and WO_3 ones are expected for their wide applications such as sensors and building blocks for constructing functional nanostructures.

References

[1] B. Gerand, G. Nowogrocki, M. Figlarz, Journal of Solid State Chemistry, 38 (1981) 312-320.

[2] J. Shi, G. Hu, R. Cong, H. Bu, N. Dai, New Journal of Chemistry, 37 (2013) 1538-1544.

[3] Y. P. Xie, G. Liu, L. Yin, H. M. Cheng, Journal of Materials Chemistry, 22 (2012) 6746-6751.

[4] X. Liu, F. Wang, Q. Wang, Physical Chemistry Chemical Physics, 14 (2012) 7894-7911.

[5] Y. P. Xie, G. Liu, L. Yin, H. M. Cheng, ACS Applied Materials & Interfaces, 4 (2012) 3372-3377.

[6] O. U. Nimittrakoolchai, S. Supothina, Materials Chemistry and Physics, 112 (2008) 270-274.

[7] S. J. Kim, I. S. Hwang, J. K. Choi, J. H. Lee, Thin Solid Films, 519 (2011) 2020-2024.

[8] S. J. Kim, I. S. Hwang, J. K. Choi, J. H. Lee, Journal of Materials Chemistry, 22 (2012) 17744-17752.

[9] X. Su, F. Xiao, Y. Li, J. Jian, Q. Sun, J. Wang, Materials Letters, 64 (2010) 1232-1234.

[10] J. Ma, J. Zhang, S. Wang, T. Wang, J. Lian, X. Duan, W. Zheng, The Journal of Physical Chemistry C, 115 (2011) 18157-18163.

[11] H. F. Pang, X. Xiang, Z. J. Li, Y. Q. Fu, X. T. Zu, physica status solidi (a), 209 (2012) 537-544.

[12] H. Zhang, G. Duan, Y. Li, X. Xu, Z. Dai, W. Cai, Crystal Growth & Design, 12

(2012) 2646-2652.

[13] K.O. Iwu, A. Galeckas, P. Rauwel, A.Y. Kuznetsov, T. Norby, Journal of Solid State Chemistry, 185 (2012): 245-252.

[14] J. Livage, G. Guzman, Solid State Ionics, 84 (1996) 205-211.

[15] M. Gotić, M. Ivanda, S. Popović, S. Musić, Materials Science and Engineering: B, 77 (2000) 193-201.

[16] Y. G. Choi, G. Sakai, K. Shimanoe, N. Miura, N. Yamazoe, Sensors and Actuators B: Chemical, 87 (2002) 63-72.

[17] J. Livage, D. Ganguli, Solar Energy Materials and Solar Cells, 68 (2001) 365-381.

[18] M. Breedon, P. Spizzirri, M. Taylor, J. du Plessis, D. McCulloch, J. Zhu, L. Yu, Z. Hu, C. Rix, W. Wlodarski, K. Kalantar-zadeh, Crystal Growth & Design, 10 (2009) 430-439.

[19] Y. G. Choi, G. Sakai, K. Shimanoe, Y. Teraoka, N. Miura, N. Yamazoe, Sensors and Actuators B: Chemical, 93 (2003) 486-494.

[20] Y. G. Choi, G. Sakai, K. Shimanoe, N. Yamazoe, Sensors and Actuators B: Chemical, 101(2004) 107-111.

[21] R. F. Mo, G. Q. Jin, X. Y. Guo, Materials Letters, 61 (2007) 3787-3790.

[22] M. F. Daniel, B. Desbat, J.C. Lassegues, B. Gerand, M. Figlarz, Journal of Solid State Chemistry, 67 (1987) 235-247.

[23] A. Cremonesi, Y. Djaoued, D. Bersani, P.P. Lottici, Thin Solid Films, 516 (2008) 4128-4132.

[24] D. Chen, L. Gao, A. Yasumori, K. Kuroda, Y. Sugahara, Small, 4 (2008) 1813-1822.

Chapter 3

Synthesis of Hexagonal WO_3 Nanoneedles via Hydrothermal Treatment of Ion-exchanged Precursor

Abstract

A facile route for synthesis of $WO_3 \cdot 0.33H_2O$ nanoneedles via hydrothermal treatment of an aqueous ion-exchanged precursor has been demonstrated. The effects of hydrothermal conditions such as reaction temperature and time on the morphology and structure of $WO_3 \cdot nH_2O$ have been studied systematically. The $WO_3 \cdot 0.33H_2O$ with an orthorhombic structure and needle-like morphology was synthesized at 120 °C for 5 h. No significant change in the structure and morphology was observed with increasing reaction time to 24 h. At the same temperature, the $WO_3 \cdot 0.33H_2O$ grew preferentially along the [100] direction, and was eventually enclosed by {001}, {010} and {110} facets. The observed needle-like evolution has been explained based on the crystal structure of orthorhombic $WO_3 \cdot 0.33H_2O$. The $WO_3 \cdot 0.33H_2O$ nanoneedle was fully dehydrated when it was heated at 350 °C in air. Phase transformation to the hexagonal WO_3 was induced by this dehydration.

3.1 Introduction

Tungsten trioxide and its hydrates ($WO_3 \cdot nH_2O$) have been extensively studied because of their crystal polymorphism [1], intriguing physical and chemical properties [2-4] and widespread applications [5-8]. Among them, $WO_3 \cdot 0.33H_2O$ has been of interest owing to its unique structure [9,10], that is, layers built up by corner shared WO_6 octahedral forming six-membered rings, with water molecules between these planes. Recently, synthetic strategy for nanostructures of $WO_3 \cdot 0.33H_2O$ and their dehydrated hexagonal WO_3 has been a focused subject due to the concerns in both fundamental science and technological applications [11-16]. In particular, one-dimensional nanostructures such as nanoneedles and nanofibers have been attracted much attention because they not only can provide unique properties [13,16] but also can be used as building blocks for functional micro/nanostructured materials [14-16].

Hydrothermal treatment of acidified precursor has been widely investigated to synthesize $WO_3 \cdot 0.33H_2O$ nanoneedles [13, 17-19]. This precursor is usually prepared by acidification of Na_2WO_4 solution with HCl, which contains impurity ions of Na^+ and Cl^-. Gerand et al. synthesized $WO_3 \cdot 0.33H_2O$ nanoneedles using the acidified precursor when heating at 120 °C [18]. In addition, It has been reported that NaCl [13,19] or the sulfate salt [20] act as effective capping agents for formation of one-dimensional evolution of $WO_3 \cdot 0.33H_2O$. However, under the utilization of the acidified precursor and the inorganic salts, the unavoidably contaminated cations such as Na^+ in the final products may result in negative effects on the performances of materials [21].

Ion-exchanged precursor is an alternative acidified precursor [2, 22], which is prepared by acidification only through a protonated cation-exchange resin. It contains negligible small amount of the impurity ions. Recently, we have utilized this precursor for synthesis of $WO_3 \cdot nH_2O$, and observed a dominant two-dimensional growth of $WO_3 \cdot H_2O$

under a relatively low temperature (50 °C), resulting in nanoplatelet morphology [23]. Mo et al. obtained nanorods of $WO_3 \cdot 0.33H_2O$ and h-WO_3 mixed phases at 180 °C for 24 h [24]. However, since there are only a few works available in the published literature on the hydrothermal treatment of ion-exchanged precursor, it has been still remained unclear if the impurity-free route can be utilized for the one-dimensional growth of $WO_3 \cdot 0.33H_2O$.

In this study, a facile route for synthesis of pure $WO_3 \cdot 0.33H_2O$ nanoneedles via hydrothermal treatment of an aqueous ion-exchanged precursor has been demonstrated. We have systematically examined the effects of hydrothermal conditions on the morphological and structural evolution of $WO_3 \cdot nH_2O$, and proven that the product of pure $WO_3 \cdot 0.33H_2O$ can be obtained by heating at 120 °C for 5 h or the longer reaction time. Morphological and structural examinations revealed that the $WO_3 \cdot 0.33H_2O$ grows preferentially along the [100] direction, resulting in nanoneedle structure. We expect that the synthetic strategy for the one-dimensional nanostructure of $WO_3 \cdot 0.33H_2O$ will receive some benefits as contamination-free route and versatile techniques.

3.2 Experimental

3.2.1 Materials

Sodium tungstate dihydrate ($Na_2WO_4 \cdot 2H_2O$, > 99%) was purchased from Kanto Chemical Co. (Japan) and was used without further purification. Strong acid type of Diaion PK228LH cation exchange resin (ion-exchange capacity > 2.05 meq/mL) was supplied from Mitsubishi Chemical Co. (Japan). Deionized water (18.2 MΩcm) from Sartorius-arium® 61316 system (Germany) was used throughout the experiments.

A glass column with height of 150 mm and 24.6 mm in diameter was used for the

ion-exchange process. The glass column was packed with 30 mL of the ion- exchange resin, and then 10 mL of water was passed through the column to wash the resin. This washing step was repeated five times before experiment.

3.2.2 Sample preparation

0.5M Na_2WO_4 solution was prepared by dissolving $Na_2WO_4 \cdot 2H_2O$ powder into deionized water. Then, a 10 mL of the solution was loaded on the glass column, and let it flow down through the resin bed with a rate of 5mL/min. The acidified precursor was recovered from the column by elution with deionized water. The precursor was yellowish and transparent. This ion-exchange treatment was performed in the temperature-controlled chamber at 15 °C. The concentration of W in as-received precursor was estimated to be 0.23~0.24 M by X-ray fluorescence spectroscopy (EDX-800, Shimadzu, Japan). The Na concentration was determined to be 1.7 ±0.6 ppm (n=3) by inductively coupled plasma atomic emission spectrometry (ICP-AES, Optima 4300DV, Perkinelmr).

After achieving complete exchange, the eluted solution was transferred to a Teflon-lined stainless steel autoclave. This ion-exchanged precursor was hydrothermally treated under different reaction temperature (80, 100, 120 and 180 °C) and time (5, 15, 24, 120 h). No additive was employed. After the hydrothermal treatment, the $WO_3 \cdot nH_2O$ powders were obtained, and they were collected by centrifugation and dried in room temperature under vacuum.

3.2.3 Sample characterizations

The crystallographic phase of the samples was determined by powder X-ray diffraction (Ultima IV, Rigaku, Japan, Cu-Kα radiation). Their morphology was

examined by scanning electron microscopy (SU-70, Hitachi, Japan) and by transmission electron microscopy (JEM-2100F, JEOL, Japan). The weight loss of the sample was measured by a thermogravimetric analysis (TG/DTA 6200, SII, Japan). The structural property of WO_3 obtained by annealing the $WO_3 \cdot H_2O$ sample was evaluated by XRD and TEM analyses. The phase evolution was observed by high temperature X-Ray diffraction (HT-XRD) analysis which was conducted by using an instrument of Multiflex (CuKα, 40 kV, 40 mA, Rigaku Co., Japan) in the range between room temperature and 500 °C in air with a 0.02 ^{o} step. Each XRD pattern was acquired after 1 h holding at each temperature. The samples were mounted on a platinum plate. UV-Vis diffuse reflectance spectroscopy was carried out on an UV-Vis spectrophotometer (UV-2450, Shimadzu, Japan), equipped with an integrating sphere and a $BaSO_4$ reference.

An aqueous suspension of $WO_3 \cdot 0.33H_2O$ was prepared as follows: the hydrothermal treated tungsten oxide was centrifuged at 5000 G for 15 min, then the precipitated was dispersed in 10 mM NH_4NO_3 solution with mass ratio of 5 mass%. This suspension had a pH value of 4.2, and was used later as a precursor to coating experiment. The obtained suspension was diluted again with 10 mM NH_4NO_3 solution and the solid concentration was controlled to be 0.125 mass%. The zeta potentials of this suspension were measured as a function of pH at room temperature using a zeta potential analyzer (Zeta plus, Brookhaven, USA). The solution pH was adjusted with HNO_3 or NH_3 solution.

3.3 Results and discussion

3.3.1 Synthesis of $WO_3 \cdot 0.33H_2O$ nanoneedles

The hydrothermal temperature was varied from 80 to 180 °C, while keeping reaction time for 24 h. The XRD patterns of the samples synthesized at different temperatures are shown in Fig. 3.1. When the reaction was conducted at 80 °C, the main phase was orthorhombic $WO_3 \cdot H_2O$ phase (ICDD No.00-043-0679). The secondary phase was orthorhombic $WO_3 \cdot 0.33H_2O$ phase (ICDD No.01-072-0199). When heating at 100 ^oC the main phase was orthorhombic $WO_3 \cdot 0.33H_2O$ phase, and the secondary phase was orthorhombic $WO_3 \cdot H_2O$ phase. Further enhancing the reaction temperature to 120 °C, the crystal phase of the sample was identified as pure $WO_3 \cdot 0.33H_2O$.When heating at 180 °C, some characteristic peaks of h-WO_3 were observed, indicating that the orthorhombic $WO_3 \cdot 0.33H_2O$ structure began to transfer to the h-WO_3 phase.

To further investigate the growth of the $WO_3 \cdot 0.33H_2O$, the hydrothermal reaction was also conducted at 120 °C for different reaction time. Figure 3.2 shows the XRD patterns of the $WO_3 \cdot 0.33H_2O$ obtained for 5, 24 and 120 h. No significant difference is observed for the XRD patterns, indicating that the $WO_3 \cdot 0.33H_2O$ structure was well formed even for relatively short reaction time of 5 h.

The morphologies of the samples obtained at 120 °C for 5 and 24 h are shown in Fig.3.3, respectively. On the basis of the SEM observation, these samples were composed of a large quantity of nanoneedles. The width and length of the nanoneedles did not significantly depend on the reaction time, indicating also that the needle-like morphology was well developed even for relatively short reaction time of 5 h. Average width of the randomly selected 150 nanoneedles in the sample obtained for 24 h was ~20 nm and the length was up to ~ 300 nm, reaching an aspect ratio more than 10.

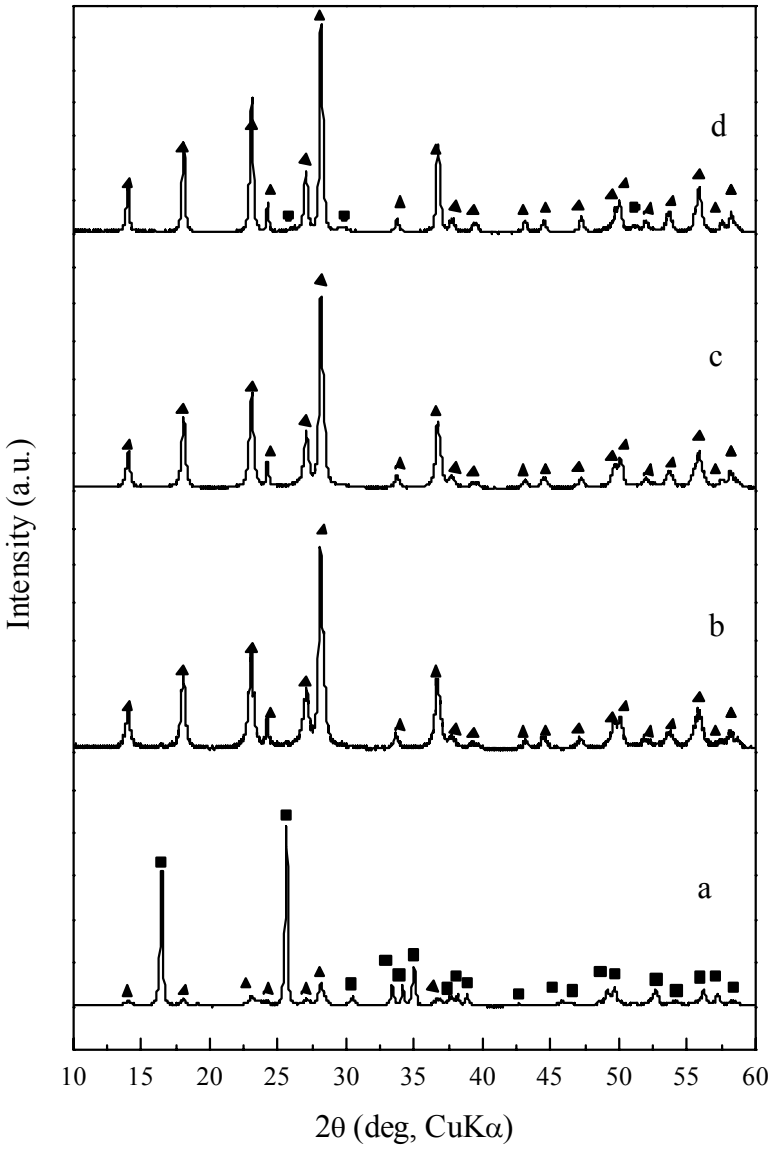

Fig. 3.1 XRD patterns of tungsten oxide hydrates synthesized for 24 h at different reaction temperature of (a) 80, (b) 100, (c) 120 and (d) 180 ^{o}C.

Peaks marked with ■ can be indexed to orthorhombic $WO_3 \cdot H_2O$ (ICDD No: 00-043-0679). Peaks marked by ▼ can be indexed to orthorhombic $WO_3 \cdot 0.33H_2O$ (ICDD No: 01-072-0199). Peaks marked by ● can be indexed to hexagonal WO_3 (ICDD No: 01-075-2187).

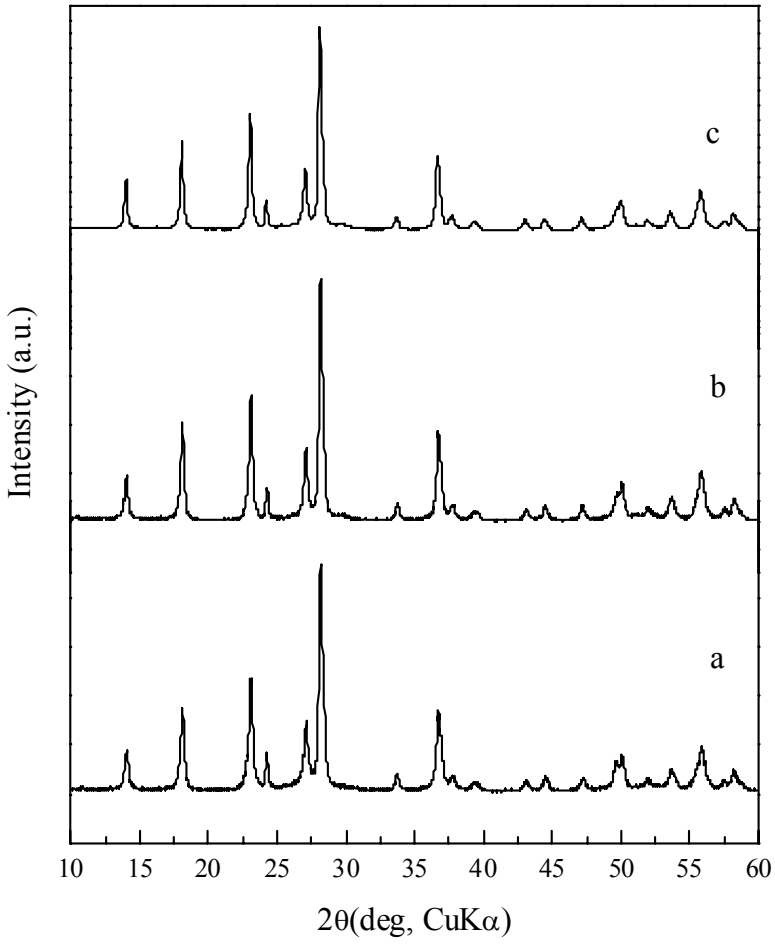

Fig. 3.2 XRD patterns of the nanoneedles synthesized at 120 ^{o}C for different reaction time of (a) 5, (b) 24 and (c) 120 h. (all peaks can be indexed to orthorhombic $WO_3 \cdot 0.33\ H_2O$ (ICDD No. 01-072-0199).

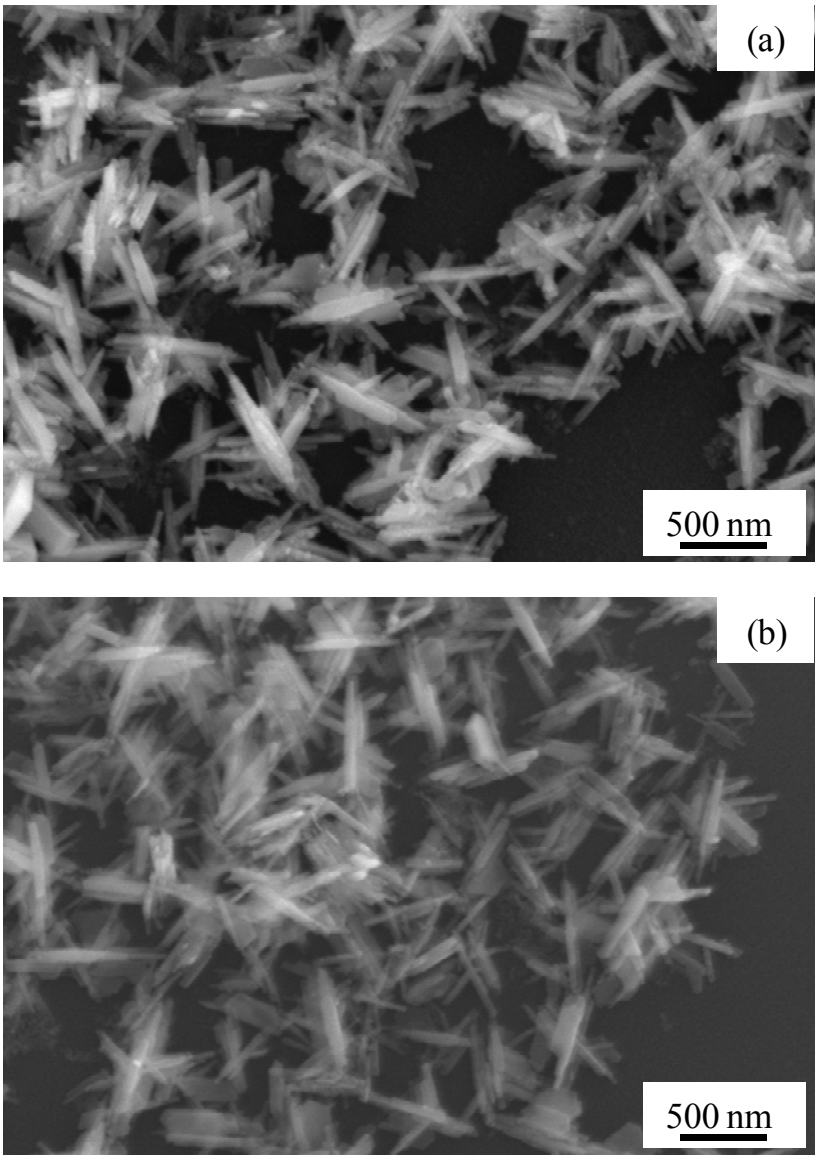

Fig. 3.3 SEM images of $WO_3 \cdot 0.33H_2O$ nanoneedles synthesized at 120 °C for (a) 5 and (b) 24 h.

To understand the detailed structural and morphological characteristics of the $WO_3 \cdot 0.33H_2O$ nanoneedle, the TEM technique was employed. Figure 3.4 (a) shows a typical well-developed nanoneedle found in the sample obtained at 120 °C for 24 h. As can be seen, it consisted of a few or several nanoneedles which elongated and ended triangularly-tapered shape. Figure 3.4 (b) shows its corresponding selected area electron diffraction (SAED) pattern. Interestingly, the SAED pattern can be assigned to a phase of single crystalline of the orthorhombic $WO_3 \cdot 0.33H_2O$ located along the [001] zone axis, implying that the nanoneedles had a single crystal nature and their crystallographic orientation remain the same. It provides that top and bottom surfaces of the nanoneedle were of well-defined {001} facet, and the nanoneedle elongated obviously along the [100] direction. Also, the [010] direction is almost perpendicular to adjacent side edge of the nanoneedle, suggesting that the side facets of the nanoneedle were enclosed by the {010} planes. In addition, the [110] direction is almost perpendicular to the tapered side at the tip of the nanoneedle, suggesting that the ends of nanoneedle are enclosed by {110}. From these observations, it can be concluded that the $WO_3 \cdot 0.33H_2O$ crystal grew preferentially along the [100] direction by hydrothermal treatment at 120°C and was eventually enclosed by {001}, {010} and {110} facets as illustrated in Fig. 3.4 (c). The nanoneedles synthesized in the present condition were mainly aligned and stacked structure as shown in Fig. 3.4.

Figure 3.5 shows the weight loss behavior of the $WO_3 \cdot 0.33H_2O$ nanoneedles for temperatures from 25 °C to 500 °C in air measured by TGA. It is clear that the sample had an obvious weight loss around 250 °C and was almost completely dehydrated at around 350 °C. The amount of the structural water of the sample was calculated from the weight loss difference between 150 °C and 500 °C. As a result, it corresponded to about $0.4H_2O$ per mole of WO_3.

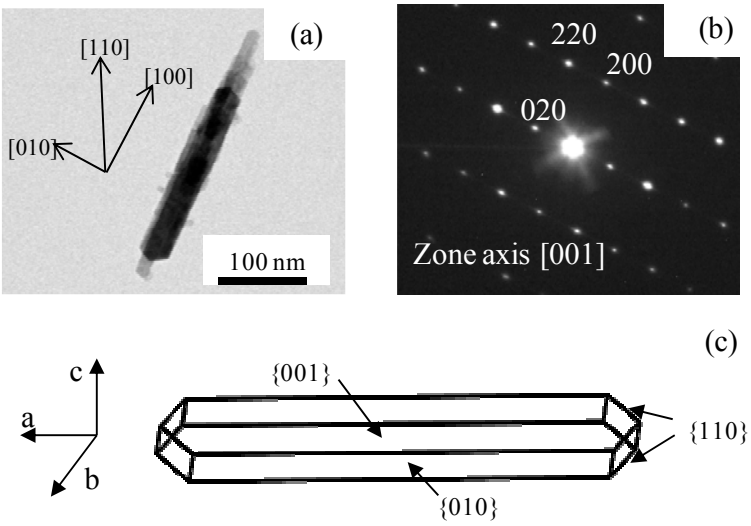

Fig. 3.4 (a, b) TEM image of $WO_3 \cdot 0.33H_2O$ nanoneedle synthesized at 120 ^oC for 24 h and its corresponding SAED pattern. (c) Crystal model of an elongated $WO_3 \cdot 0.33H_2O$.

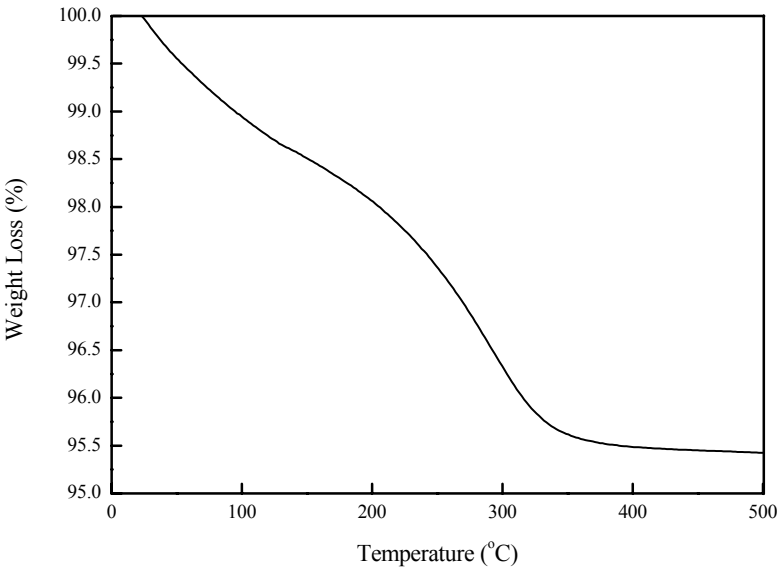

Fig. 3.5 TGA curve of $WO_3 \cdot 0.33H_2O$ sample synthesized at 120 °C for 24 h.

The amount of the structural water estimated was a little higher than theoretical value of 0.33. In this time, we have not taken carefully account of amount of physically adsorbed water trapped between nanoneedles. If it is removed sufficiently, the value would be close to the theoretical one. As demonstrated in this study, the reaction temperature plays an important role in controlling the morphology and structure of $WO_3 \cdot nH_2O$. The nanoneedles of pure $WO_3 \cdot 0.33H_2O$ phase were first time obtained from the ion-exchanged precursor at 120 °C. The results were reproducible and indicate that phase formation of $WO_3 \cdot 0.33H_2O$ and its one-dimensional growth well promotes even without any inorganic additives such as NaCl and Na_2SO_4. Peroxo-polytungstic acid solution has been also known as impurity-free aqueous precursor [25]. However, hydrothermal treatment of the peroxo-polytungstic acid solution did not produce nanoneedle, but nanodisc $WO_3 \cdot 0.33H_2O$ [11].

It has been known that all $WO_3 \cdot nH_2O$ are formed of layers built up by corner sharing $[WO_6]$ octahedral, with water molecules between these planes. Formation of $WO_3 \cdot nH_2O$ in acidified precursor is generally explained as follows [22,26]. The intermediate $[WO(OH)_4(OH)_2]$ is formed in the acidified precursor at the initial period of aging, where one water molecule is bonded along to the *z*-axis opposite to the W=O bond while the four OH groups are in the equatorial *x*-*y* plane. Then, oxolation reaction along to the equivalent *x*- and *y*- directions leads to layered structure. As we reported recently, the reaction promotes to form corner-sharing their four equatorial oxygen atoms of octahedra by aging at 50 °C, resulting in $WO_3 \cdot H_2O$ phase [23]. On the other hand, it was found in this study that more open structure with forming six membered rings can be formed when heating up to 120 °C, resulting in $WO_3 \cdot 0.33H_2O$ phase. Since the ion-changed precursor does not contain any structure-directing species, the dielectric constant of water would play an important role. As Livage and Guzman discussed [22], the dielectric constant of

water decreases as the temperature increase, and then electrostatic repulsions between highly charged W^{6+} ions become stronger, which lead to the formation of the more open structures such as hexagonal $WO_3 \cdot 0.33H_2O$. However, the detailed mechanism of formation of the $WO_3 \cdot 0.33H_2O$ phase needs to be further explored.

The observed preferential growth of $WO_3 \cdot 0.33H_2O$ along [100] direction can be explained from the crystal growth habit of $WO_3 \cdot 0.33H_2O$. As well known, crystal growth along the direction perpendicular to the face with the highest surface free energy possesses the fastest growth rate, leading to exposure of the lower-energy faces. In the orthorhombic $WO_3 \cdot 0.33H_2O$ structure, the surface free energy of different faces have the order of {100} > {110} > {010} > {001} [11]. On this basis, the fastest crystal growth occurs in the [100] direction and the {001}, {010} and {110} facets are expected as the exposed surfaces in $WO_3 \cdot 0.33H_2O$. This expectation agrees with our experimental results.

3.3.2 Dehydration behavior of $WO_3 \cdot 0.33H_2O$ nanoneedles

Figure.3.6 shows the HT-XRD pattern of the obtained tungsten oxide hydrates. The XRD pattern recorded at room temperatures represented only a single phase of orthorhombic $WO_3 \cdot 0.33H_2O$. No phase change occurred up to 300 ^oC. The phase transformation started by annealing the sample at 350 ^oC. The XRD pattern recorded at 350 ^oC presented a single phase of hexagonal WO_3. No phase change occurred up to 450 ^oC. Finally, monoclinic WO_3 appeared by annealing at 500 ^oC. It should be noted that the hexagonal WO_3 and orthorhombic $WO_3 \cdot 0.33H_2O$ phases exhibit very similar XRD patterns except for the characteristic diffraction peak located at 18 ^{o} [27].

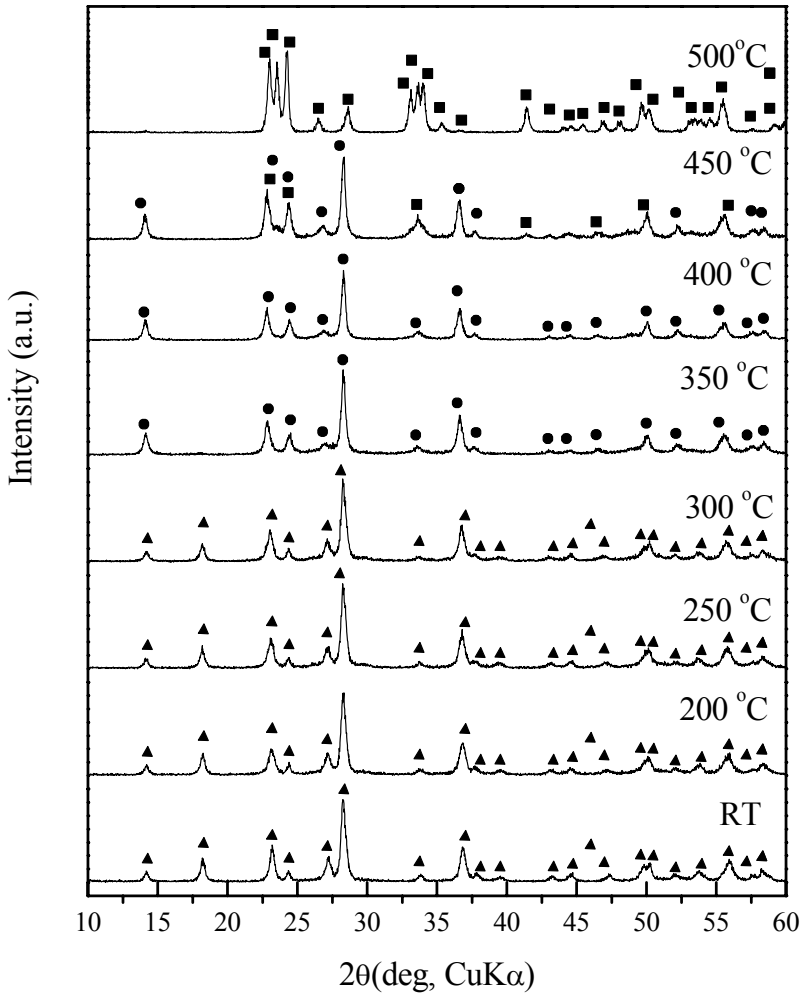

Fig. 3.6 HT-XRD patterns of tungsten oxide aged at 120 °C for 24 h recorded from room temperature to 500 °C.

Peaks marked by ▼ can be indexed to orthorhombic $WO_3 \cdot 0.33H_2O$ (ICDD No: 01-072-0199). Peaks marked by ● can be indexed to hexagonal WO_3 (ICDD No: 01-075-2187) Peaks marked with ■ can be indexed to monoclinic$WO_3 \cdot H_2O$ (ICDD No: 01-072-0677).

From these results it could be concluded that, the dehydration of $WO_3 \cdot H_2O$ nanoplates started at temperature around 200 ^oC and completed at 300 ^oC. The phase transformation occurred between 300 ^oC and 350 ^oC. The major water loss almost completed at 320 ^oC.

Figure 3.7 shows the SEM image of nanoneedles after annealing at 350 ^oC for 1 h. The annealed step did not affect the morphological structure of the obtained nanoneedles, indicating that the transformation from $WO_3 \cdot 0.33H_2O$ to h-WO_3 nanoneedles is a topotactic process [24].

The optical property of the hexagonal WO_3 nanoneedles was investigated by measuring the diffuse reflectance spectrum. The optical absorbance was approximated from the diffuse reflectance data by the Kubelka-Munk transformation [34], as shown in Fig. 3.8. Considering that WO_3 is an indirect n-type semiconductor, its energy band gap (E_g) can be determined using the following relationship[35]:

$$\alpha h\nu = A(h\nu - E_g)^2 \qquad (3.1)$$

where α, $h\nu$, and A are the absorption coefficient, the energy of the incident photon and a constant, respectively. The inset in Fig. 3.8 shows the plot of $(\alpha h\nu)^{1/2}$ *vs* $h\nu$. Extrapolating the liner plot, the energy band gap can be estimated to be ~ 2.7eV.

3.3.3 Aqueous dispersion for assembling nanoneedles

Following the synthesis of 1D nanostructured $WO_3 \cdot 0.33H_2O$, their assembly on a substrate is another challenge. In this regard, preparation of stable colloidal dispersion of $WO_3 \cdot 0.33H_2O$ nanoparticles is quite important for utilizing conventional dip-coating and spin-coating methods for their assembly.

Particles in any colloidal dispersion experience attractive force by van der Waals interactions which can promote reversible or irreversible aggregation. To prepare stable colloidal dispersion, it is necessary to introduce interaction between particles that oppose

the van der Waals attraction. One method of achieving this is to charge the particles. If particles possess suitable chemical functionality, they can become charged as a result of the ionization of surface groups. In aqueous solution, pH is commonly used to control the degree and nature of the ionization. Metal oxides or hydrates may become charged as a result of protonation or deprotonation of surface groups (OH groups).

Figure 3.9 shows the zeta potential of the $WO_3 \cdot 0.33H_2O$ nanoneedles as a function of pH at room temperature. From this experiment, the isoelectric point (IEP) at which zeta potential is zero is determined to be pH~1.2, indicating that the surface hydroxyls on $WO_3 \cdot 0.33H_2O$ nanoneedles are acidic. At a pH less than 1.2, the nanoneedles are positively charged due to protonation. On the other hand, at a pH more than 1.2, they are negatively charged due to deprotonation. The measurement was not taken at a pH more than 5, because of their significant dissolution.

Figure 3.10 shows the sedimentation behavior of $WO_3 \cdot 0.33H_2O$ nanoneedles dispersed in aqueous solution with different pH values. As can be seen, they did not sediment significantly when the solution pH was controlled to be ~4. The observed colloidal stability can be attributed to the highly negatively charge of the $WO_3 \cdot 0.33H_2O$ nanoneedles at pH ~4 as shown in Fig. 3.9.

Based on these results, a colloidal dispersion of $WO_3 \cdot 0.33H_2O$ nanoneedles (solid concentration: 5 mass %) with pH~4.2 was prepared, and then used for film formation. The colloidal dispersion of $WO_3 \cdot 0.33H_2O$ nanoneedles was coated on FTO glass (15Ω/□, sigma, USA) by dip coating method (Dip Coater, Aiden, China). The withdraw speed was fixed to 1mm/s at room temperature and humidity of RH ~50%. The obtained layer was vacuum-dried for 30 min, and then it was annealed at 400 ^oC for 1 h with heating rate of 10 ^oC/ min to fix them on the substrate and transform them to h-WO_3. This procedure was repeated three times. Figure 3.11 (a) shows the SEM image of surface of the obtained film.

The h-WO_3 nanoneedles were aligned randomly parallel to the FTO surface covering most of the surface, except some small area still uncovered.

As a first trial, electrochromic coloration was carried out for the as-prepared h-WO_3 nanoneedle film by a three-electrode electrochemical cell with 1.0 M lithium perchlorate ($LiClO_4$) in propylene carbonate (PC) as the electrolyte. The measurements were carried out with use of potentiostat (PARSTAT 2263, Princeton Applied Research, Germany). The WO_3 nanoneedle film was vertically inserted into the electrolyte and acted as the working electrode, Pt wire acted as the counter electrode, and the Ag/AgCl electrode acted as the reference electrode. The observed electrochromic phenomena of the h-WO_3 nanoneedle film were shown in Fig. 3.11(b) and (c). It can be seen that the as-prepared WO_3 nanoneedle film is almost colorless. When applying a voltage of -1.5 V for 30s, the film displayed a blue color, indicating that the intercalation of electrons and charge balancing of Li^+ ions result in the coloration switching.

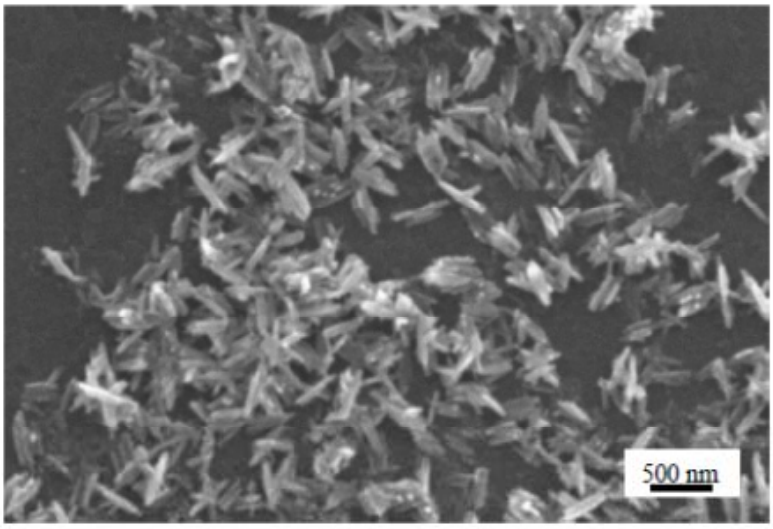

Fig .3.7 SEM images of hexagonal WO_3 nanoneedles synthesized at 120 ^oC for 24 h and annealed at 350 ^oC for 1 h.

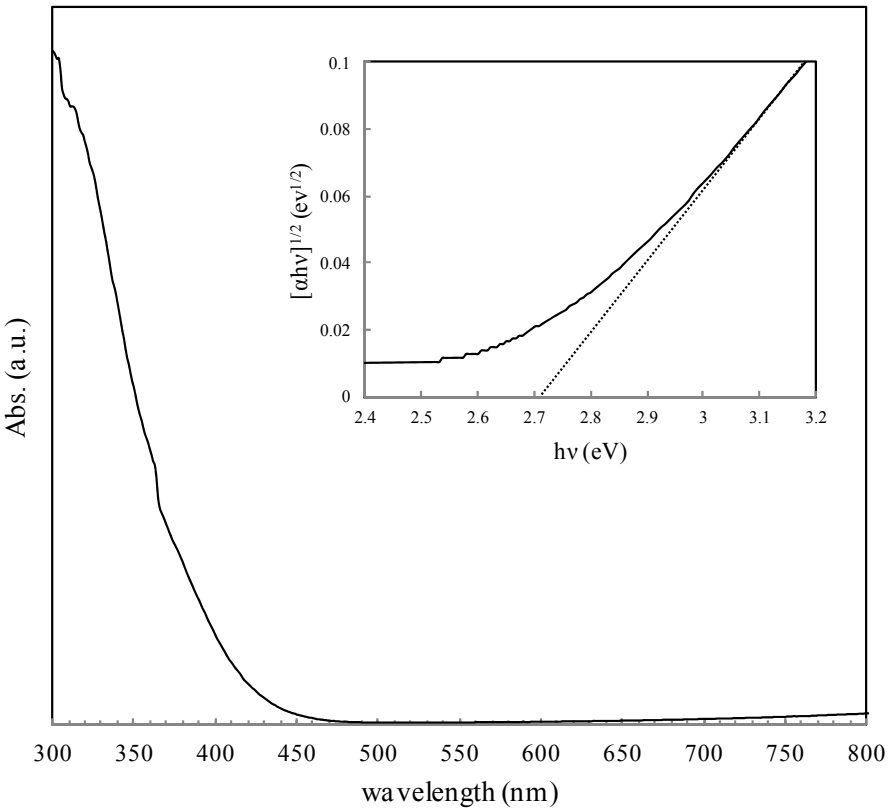

Fig. 3.8 Absorption spectrum of hexagonal WO_3 nanoneedles. The inset shows the plot of $(\alpha h\nu)^{1/2}$ versus $h\nu$.

.

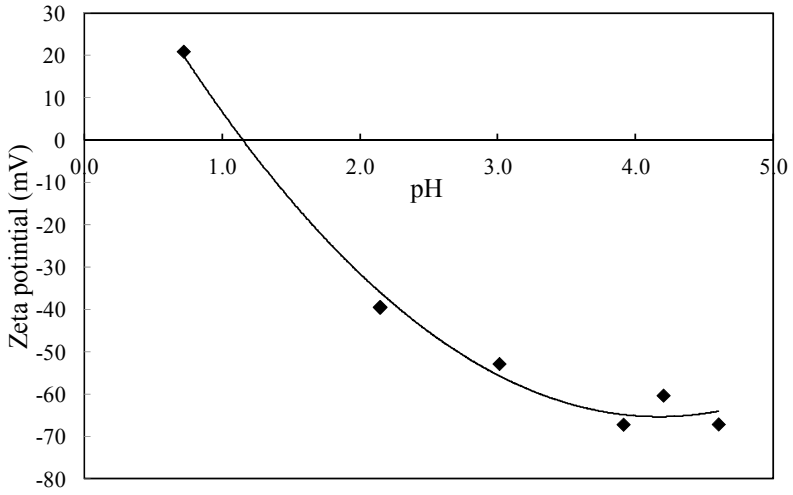

Fig. 3.9 The zeta potential of hexagonal nanoneedles as a function of pH.

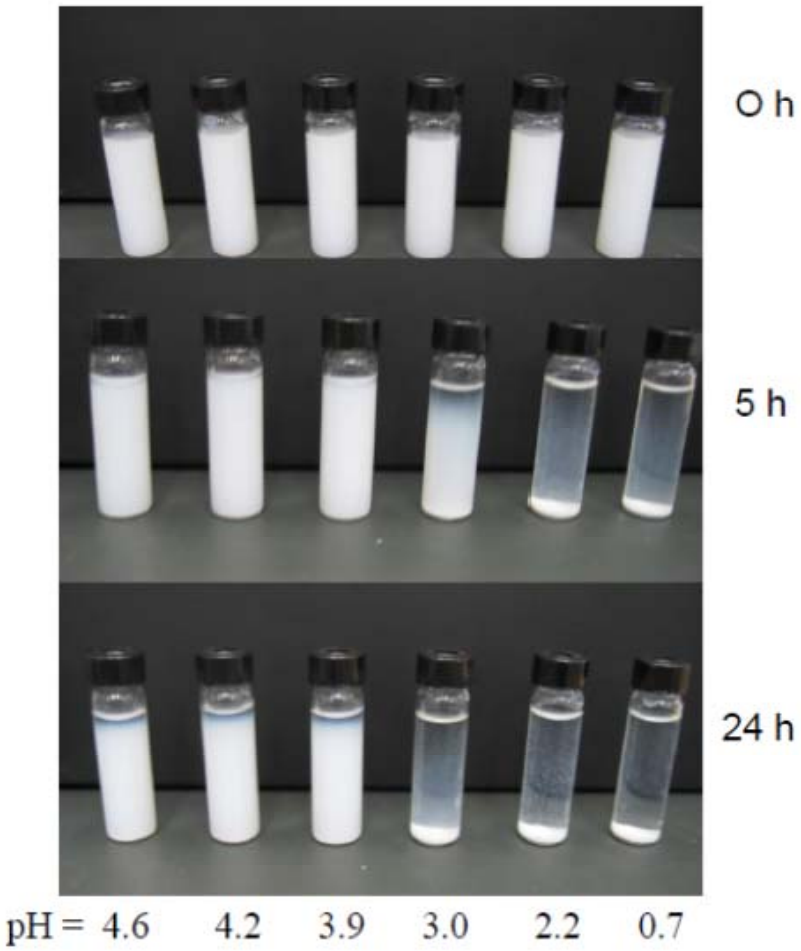

Fig. 3.10 Sedimentation of tungsten oxide nanoneedles in aqueous solution with different pH values.

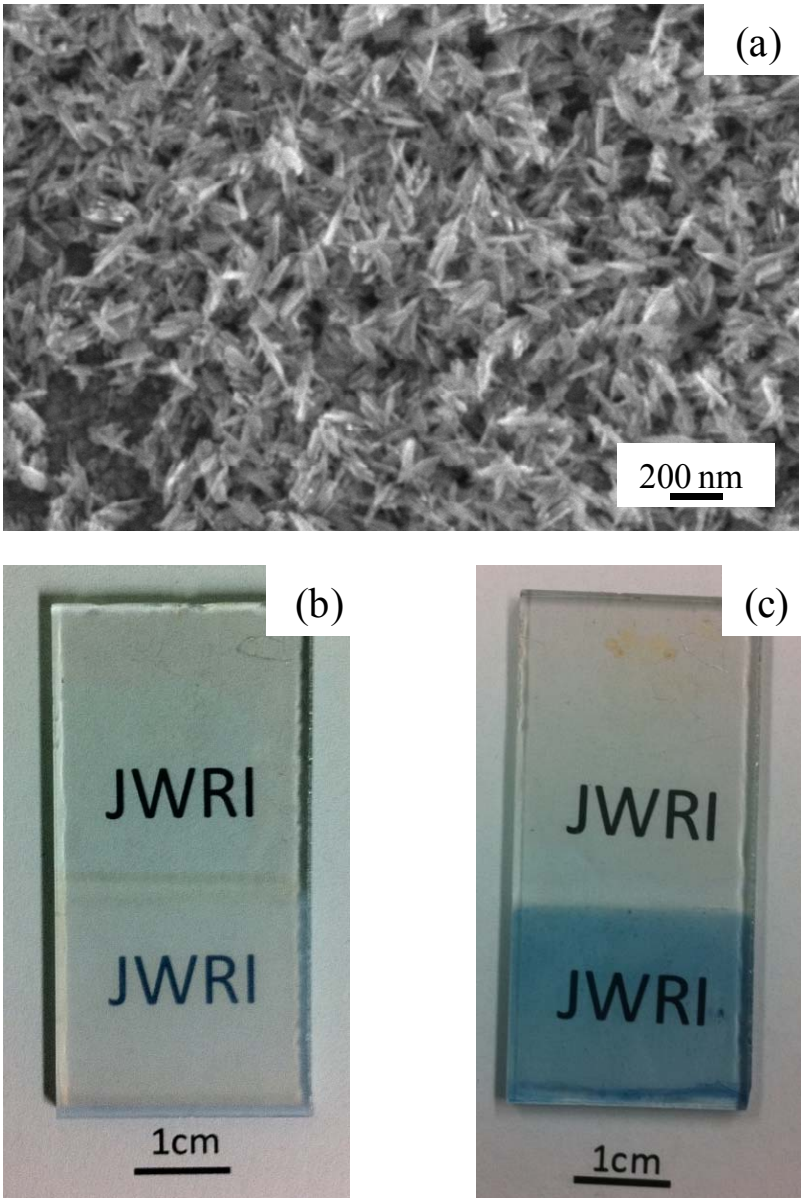

Fig. 3.11 (a) SEM image of hexagonal WO_3 thin film prepared by dip coating and annealed at 400 ^{o}C for 1 h , photographs of hexagonal WO_3 nanoneedles thin film (b) as - prepared , and (c) colored at -1.5V for 30 s.

3.4 Conclusions

We have successfully synthesized $WO_3 \cdot 0.33H_2O$ nanoneedles by the additive-free hydrothermal treatment. It was found that the reaction temperature plays an important role on the one-dimensional growth of $WO_3 \cdot 0.33H_2O$, and the nanoneedles were produced at 120 °C even for relatively short reaction time of 5 h. The morphological evolution of the nanoneedle has been explained based on the crystal structure of $WO_3 \cdot 0.33H_2O$. The present synthesis route provides a facile and impurity-free approach for synthesis of $WO_3 \cdot 0.33H_2O$ nanoneedles. It is expected that the nanoneedles can be applied to wide areas and building blocks for constructing functional nanostructures.

References

[1] C. Guery, C. Choquet, F. Dujeancourt, J. M. Trascon, J. C. Lassegus, J. Solid State Electrochem. 1 (1997) 199-207.

[2] C. Santaro, M. Odziemkowski, M. Ulmann, J. Augustynski, J. Am. Chem. Soc. 123 (2001) 10639- 10649.

[3] Y. P. Xie, G. Liu, L. Yin, H. M. Cheng, J. Mater. Chem. 22 (2012) 6746-6751.

[4] S. H. Baeck, K. S. Choi, T. F. Jaramillo, G. D. Stucky, Adv. Mater. 15 (2003) 1269-1273.

[5] C. Cosa, C. Pinheiro, I. Henriques, C. A. Laia, ACS Appl. Mter. Interfaces 4 (2012) 1330-1340.

[6] D. Li, G. Wu, G. Gao, J. Shen, F. Hung, ACS Appl. Mater. Interfaces 3 (2011) 4573-4579.

[7] R. Archrya, X. A. Cao, Appl. Phys. Lett.101 (2012) 53306-53310.

[8] W. Mickelson, A. Sussman, A. Zettl, Appl. Phys. Lett.100 (2012) 173110-173115.

[9] M. Figlarz, Prog. Solid State Chem. 19 (1989) 1-46.

[10] B. Gerand, D. Nowogrocki, J. Guenot, M. Flglarz, J. Solid, State Chem.29 (1979) 429-434.

[11] L. Zou, M. Yu, P. Lu, J. Wei, Y. Qian, Y. Wang, C. Yu, Cryst. Growth Design 8 (2008) 3993-3998.

[12] J. Li, J. Huang, C. Yu, J. Wu, L. Cao, K. Yanagisawa, Chem. Lett. 40 (2011) 579-581.

[13] X. C. Song, Y. F. Zheng, H. Y. Yin, Current Nanoscience 7 (2011) 120-125.

[14] J. Li, J. Hung, J. Wu, L. Cao, Q. Li, K. Yanagisawa, Cryst Eng Comm. 15 (2013) 7904-7913.

[15] Z. Jiao, J. Wang, L. Ke, X. W. Sun, H. V. Demir, ACS Appl. Mater. Interfaces 3

(2011) 229-236.

[16] J. Yang, L. Jiao, Q. Zhao, Q. Wang, H. Gao, Q. Huan, W. Zheng, Y. Wang, H. Yuan, J. Mater. Chem. 22 (2012) 3699-3703.

[17] J. Pfeifer, C. Guifang, P. T. Buxbaum, B. A. Kiss, M. F. Jahnke, K. Vadasdi, J. Solid State Chem.119 (1995) 90-97.

[18] B. Gerand, G. Nowogrocki, M. Figlarz, J. Solid Sate Chem.38 (1981) 312-320.

[19] J. Wang, E. Khoo, P. S. Lee, J. Ma, J. Phys. Chem. C 113 (2009) 9655-9658.

[20] Z. Gu, H. Li, T. Zhai, W. Yang, Y. Xia, Y. Ma, J. Yao, J. Solid State Chem. 180 (2007) 98-105.

[21] H. Zhang, G. Duan, Y. Li, X. Xu, Z. Dai, W. Cai, Crystal Growth Design 12 (2012) 12, 2646-2652.

[22] J. Livage, G. Guzman, Solid State Ionics 84 (1996) 205-211.

[23] M. Elnouby, K. Kuruma, E. Nakamura, H. Abe, M. Naito, Y. Suzuki, J. Ceram. Soc. Jpn. 121 (2013) 907-911.

[24] R. F. Mo, G. Q. Jin, X. Y. Guo, Mater. Lett. 61 (2007) 3787-3790.

[25] J. Oi, A. Kishimot, T. Kudo, J. Solid State Chem. 96 (1992) 13-19.

[26] J. Yang, W. Li, J. Li, D. Sum, Q. Chen, J. Mater. Chem. 22 (2012) 17744-17752.

[27] W. Xiao, J. Wu, L. Cao, J. Mater. Chem. A 1(2013) 1261-1269.

[28] Y. Shen, J. Li, D. Sum. , Powder Technology 211 (2011) 114–119.

[29] R. Sivakumar, M. Jayachandran, C. Sanjeeviraja, Mater. Chem. Phys. 87 (2004) 439-445.

[30] J. Gaury, E. M. Kelder, E. Bychkov, G. Biskos, Thin solid films 534 (2011) 32-39.

[31] L.G. Teoh, Journal of Alloys and Compounds 396 (2005) 251–254.

[32] A. Patra, K. Auddy, D. Ganguli, J. Livage, P. K. Biswas, Materials Letters 58

(2004) 1059– 1063.

[33] I. V. Shiyanovskaya, Non-Crystalline Solids 187 (1995) 420-424.

[34] P. Mohanty, C. Rath, P. mallick, R. Biiswal, N.C. Mishra, Physica B 405 (2010) 27111-2714.

[35] D. Chen, L. Gao, A. Yasumori, K. Kuroda, Y. Sugahara, Small 4 (2008) 1813-1822.

Chapter 4

Electrochromic Tungsten Oxide Thin Film Synthesized by Aqueous Sol-Gel Method

Abstract

Aqueous precursor of tungstic acid was prepared by passing the sodium tungstate solution (Na_2WO_4) through a protonated cation exchange resin. The ion-exchange precursor was spin coated on ITO glass, and then annealed at 300 ^oC to produce tungsten oxide thin films. Stabilizing agents have been added to the tungstic acid precursor to prevent fast gelation and precipitation of the precursor. The effect of the stabilizing agents on the microstructures and electrochromic performance of the obtained thin films have been investigated. The crystal structure of pure WO_3 without the additive exhibited hexagonal structure. Monoclinic structure formed from samples contained 1% hydrogen peroxide and a mixture of 1% hydrogen peroxide and 4% oxalic acid. The effect of number of layers, and additive type; hydrogen peroxide and/or oxalic acid, were investigated. The thickness of the prepared WO_3 thin films was ranged between 0.33 μm to 9.82 μm, depending on the number of applied layers. Hydrogen peroxide and oxalic acid additives led to an open porous structure and increased the diffusion coefficient from 5.3×10^{-14} to 3.1×10^{-9} cm^2/s. The highest coloration efficiency of 64.2 cm^2/C was obtained for the open porous structure of the two-layer film prepared with W^+ ion concentration of 0.1 M, and 1% hydrogen peroxide and 4% oxalic acid.

4.1. Introduction

Electrochromic devices (ECDs) are opto-electrochemical systems that change their optical properties, mainly their transmittance, when a voltage is applied. This interesting behavior leads to many applications, such as smart windows, sunroofs, shades, visor or rear view mirrors for automotive and mass transportation applications, skylight, displays, light filter and screens for light pipes and other opto-electrical devices [1].

Transition metal oxides have been widely used as inorganic electrochromic materials. Among those transition metal oxides, tungsten trioxide (WO_3), n-type semi-conductor, has been the most extensively studied material due to its electrochromic properties in the visible and infrared regions, high-coloration efficiency and relatively low price. The electrochromic properties of tungsten oxide promise their commercial application in energy-saving smart widows which combine the merits of energy-saving and indoor comfort for modern buildings [2]. Tungsten oxides have diverse polymorphs generally formed by corner and edge sharing of WO_6 octahedra. Simultaneous with stacking or packing of WO_6 octahedra into different crystalline configurations, a considerable number of interstitial sites can be generated inside crystal lattices. The resulting empty space can accommodate uptake/withdrawal of guest ions. The guest ions can diffuse and penetrate into the bulk crystals with suitable open structures, rendering adsorption-desorption of ions on the surface and also intercalation/deintercalation into/out of inner parts. Therefore, crystalline WO_3 with an open structure, e.g. the hexagonal phase, exhibits increased capacity and enhanced kinetics for ion intercalation, evidenced by the reported superior charge densities and higher lithium diffusion coefficient of hexagonal WO_3 [2]. In recent years, however, there has been an orientation to use chemical rather than physical techniques which involve high capital investments. The sol-gel or wet chemical synthesis methods offer many advantages for the preparation of high value added materials in addition to being economic [3]. The sol-gel

process is a less expensive route to produce thin films over large areas and offers the advantage of controlling the film microstructure, which strongly affects the kinetics, durability and coloration efficiency [4]. Several sol-gel routes have been developed to produce WO_3 thin films such as acidification of sodium tungstate [5, 6], peroxopolytungstic acid [7], and tungsten alkoxide [4]. Hydrated tungsten oxides $WO_3 \cdot nH_2O$ can be obtained via the acidification of a tungstate solution Na_2WO_4 through a proton exchange resin [8], or directly upon the reaction of sodium tungstate with strong acid (i.e., HCl, H_2SO_4) [5], but it needs to wash the residual of sodium chloride [9]. The washing step can be avoided by using an ion exchange resin to produce tungstic acid without any side products. A clear solution of tungstic acid H_2WO_4 was first obtained [10]. It was deposited on the substrate by different techniques, such as, spin coating [11, 12], spray [13], or dip coating [11]. Gerand et al [14] prepared orthorhombic $WO_3 \cdot 0.33H_2O$ by hydrothermal treatment of a mixture of sodium tungstate solution and HCl, which could be transformed topotactically into hexagonal WO_3 upon annealing. J. Wang et al. [15] studied the effect of NaCl amount and pH values on the microstructure of hexagonal WO_3 nanorods prepared by hydrothermal method, and the coloration efficiency of the prepared thin films was 37.6 cm^2/C.

The coloration mechanism was also studied related to the structure of WO_3 [16, 17]. Luo et al. [18] explained that by addition of H_2O_2 into doped tungstic acid caused the formation of peroxo tungstic acid by partly replacing the O^{2-} in $[WO_4]^{2-}$ with O_2^{2-}. This reaction decreased the number of O^{2-} ligands in $[WO_4]^{2-}$, decelerated the condensation among tungstic acid and stabilized the tungstic acid sols. The small ligand molecules $H_2C_2O_4 \cdot 2H_2O$ could also coordinate with W^{6+} to stabilize the tungstic acid sols, during formation of tungsten oxide thin films. Particles of tungsten oxide were separated by water and additive molecules, which were evaporated by heat treatment producing porous, as long as the particle size become larger. The pore size enlarged too proportionally to the particle size.

Various applications of the WO_3 thin films require different types of crystalline structure. Electrochromic devices employ both amorphous as well as crystalline WO_3 films owing to their high catalytic behavior both in oxidation and reduction processes [19]. Shiyanovskaya [17] supposed that the injected electron is trapped at a W^{6+} site adjacent to a proton thus forming a W^{5+} color center. Light absorption occurs due to charge transfer between two neighboring tungsten sites $W^{5+}$and W^{6+}. Injected protons compensate for the negative charge of injected electrons [17] .

It has been realized that the morphology and structure of WO_3 directly related to its ability to perform the desired function in a particular application. So, the electrochromic properties like coloration efficiency, cyclic durability, and kinetics of coloration–bleaching process of tungsten trioxide strongly depend on its structural, morphological, and compositional characteristics [19].

In this research, the tungstic acid was obtained via the acidification of a tungstate solution Na_2WO_4 through a proton exchange resin, and the obtained tungstic acid precursor was stabilized by hydrogen peroxide and oxalic acid. Then tungsten oxide thin films were spin coated from the tungstic acid and annealed at 300 ^oC for 30 min. The effect of hydrogen peroxide and oxalic acid on the performance of the WO_3 thin films was also studied.

4.2. Experimental

4.2.1 Preparation of WO_3 thin films

Tungsten oxide was formed via the acidification of a 0.1M of sodium tungstate (98%, Sisco research laboratory, India) through a proton exchange resin (Rohm& Haas, France) to produce a solution of tungstic acid, and then 0.1M of H_2O_2 and 0.1M of oxalic acid were added with 1% and 4% volume ratio respectively. The obtained solution was deposited by spin coating (Polos 300 AWS- CPK Industries, USA) at 200 rpm for 60 sec. and annealed at 300 ^oC for 30 min in an open air furnace (Carbolite, Aston Iane, Hope Sheffield, 53 2RR, England) to produce a single layer or multi-layers of tungsten oxide thin film.

4.2.2 Characterization of WO_3 thin films

X-ray diffraction patterns of the thin films were obtained by X-ray diffractometer (Schimadzu -7000, USA), operating with Cu-Kα radiation (λ = 0.154060 nm) generated at 30 kV and 30 mA. The scan rate was (2^o / min) for 2θ values between 20 and 80 degrees. The surface of the tungsten oxide thin films was investigated with high-resolution scanning electron microscopy (JEOL JSM 6360LA, Japan) to examine the morphology and the homogeneity of the surface. Thin films of gold were sputtered onto the samples to get charge free surfaces. Also, measurements of various grain sizes and film thickness were estimated from the SEM micrographs. The transmission (T %) of the prepared thin films were measured using Double beam UV-VIS spectrophotometer (Labomed, USA). The measurements were carried out in the range 190 to 1100 nm at room temperature. Vibrational spectroscopic studies for as-deposited and annealed WO_3 thin films were obtained by FTIR spectrophotometer (Schimadzu - 8400 s - Japan) at room temperature in the frequency range of 4000 – 500 cm^{-1}. Thermal properties of WO_3 upon annealing were

studied by thermo-gravimetric analysis (TGA 50, Shimadzu, Japan). Transmission electron microscopy (TEM) (JEOL JEM 1230, Japan) operating at 12 - 600 kV was used to determine the size of WO_3 nanoparticles, WO_3 thin film was stripped out from glass substrate and suspended in ethanol and then the copper grid was used for the TEM measurement.

4.2.3 Electrochromic properties of WO_3 thin films measurements

The electrochemical set-up consists of a potentiostat (Voltalab PGP201 - Radiometer Analytical - France) controlled by a computer and conventional three-electrode cell in which the saturated calomel electrode (SCE) and a platinum wire were used as reference and counter electrodes, respectively. Tungsten oxide on ITO coated glass was used as the working electrode in an electrolyte solution of lithium perchlorate (98%,Fluka, Switzerland) / propylene carbonate (PC) (99%, Aldrich, Germany) of 1M ($LiClO_4$: PC). The CV's were recorded in the range between -1 V and 1 V versus (SCE) with a scan rate of (10 mV/s). All the measurements were carried out at room temperature and the cyclic voltammograms were recorded after 10 activation cycles. Electrochromic measurements were recorded using the system which consists of potentiostat and spectrophotometer by connecting samples to potentiostat when placed inside the spectrophotometer measurement compartment, and by applying a current of (I =1mA) in a solution of 1M $LiClO_4$/PC for 60 sec and finally recording the change in transmittance at λ=550 nm, at room temperature.

4.3. Results and Discussion

4.3.1 X-Ray measurements

Figure 4.1 shows XRD patterns of WO_3 thin films prepared using different preparation conditions. Pure WO_3 thin films with no additives (Fig. 4.1a), reveals the hexagonal WO_3 structure (JCPDS card no. 33-1387). High orientation of the (001) plane at $2\theta = 23.03^{o}$ is detected. Adding 4% of oxalic acid (Fig. 4.1b) improves the crystallinity of the WO_3 hexagonal structure. Most of the planes is well identified with high orientation of (100), (001) and (201) planes detected at $2\theta = 13.26º$, 23.03º and 35.5º, respectively. Deepa et al. [11] explain that oxalic acid upon subliming out of the film catalyzes the formation of crystalline phase at lower temperature. When adding 1% H_2O_2 during WO_3 preparation, semi-amorphous structure with weak peaks of the monoclinic WO_3 structure (JCPDS card no. 54-0508) is detected as shown in Fig. 4.1(c). Adding both 1% H_2O_2 and 4% oxalic acid improved the crystallinity of the semi-amorphous structure with high orientation of (100) and (211) planes detected at $2\theta = 25.38º$ and 37.38º of the monoclinic structure (Fig. 4.1(d)).

The average crystallite size was calculated from the full width at half maximum (FWHM) of the diffraction peak using Debye- Scherrer's equation [11] and summarized in Table 4.1. The obtained pure WO_3 thin films have crystalline size of 46.2 nm increased to 49.8 nm by adding 1% hydrogen peroxide and decreased to 44.5 nm by adding 4% oxalic acid and decreased sharply to 12.3 nm by adding both of 1% hydrogen peroxide and 4% oxalic acid, with good agreement with TEM image (Fig. 4.3 b).

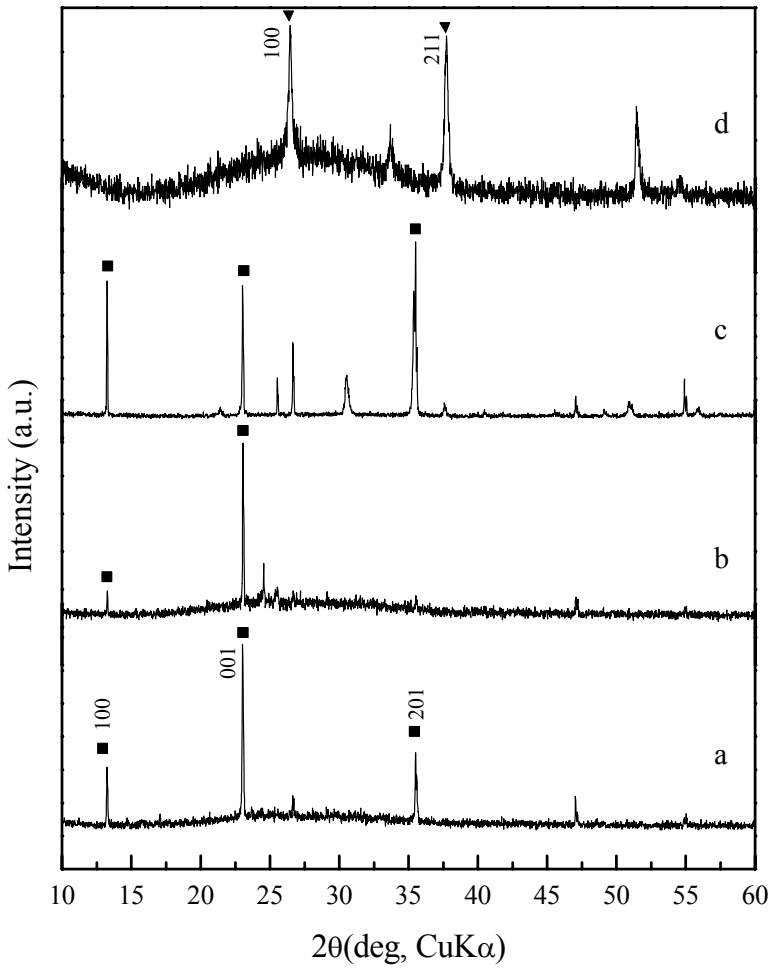

Fig. 4.1 XRD patterns of WO_3 thin films (a) pure, (b) 4% oxalic acid, (c) 1% hydrogen peroxide and (d) 1% hydrogen peroxide and 4% oxalic acid.

■ symbol refers to the hexagonal peaks, while ▼refers to monoclinic peaks.

4.3.2 Morphology evaluation

Figure 4.2 shows SEM images of the WO_3 thin films as the same conditions explained in Table 4.1. Smooth and uniform films are observed for the WO_3 thin films prepared with pure (Fig. 4.2 (a)) and with adding 1% H_2O_2 (Fig. 4.2 (b)). With the addition of 4% oxalic acid (Fig. 4.2(c)) and both 1% H_2O_2 and 4% oxalic acid (Fig. 4.2(d)), the prepared thin films exhibited porous structure. These additives have the advantage of getting crackles thin films of WO_3, as explained by Nidhi et al. [20].

Figure 4.3 shows low magnification TEM of the WO_3 nanoparticles. With no additives (Fig.4.3 (a)), the particles are agglomerated in spherical shape with a diameter of 50 - 200 nm. Adding 1% H_2O_2 (Fig. 4.3 (b)), rod shape with a diameter of about 20 nm and length of 100 nm is observed. Finally, adding 1% H_2O_2 and 4% oxalic acid (Fig.4.3(c)), these nanorods are highly detected with increasing their aspect ratio to 6-7.

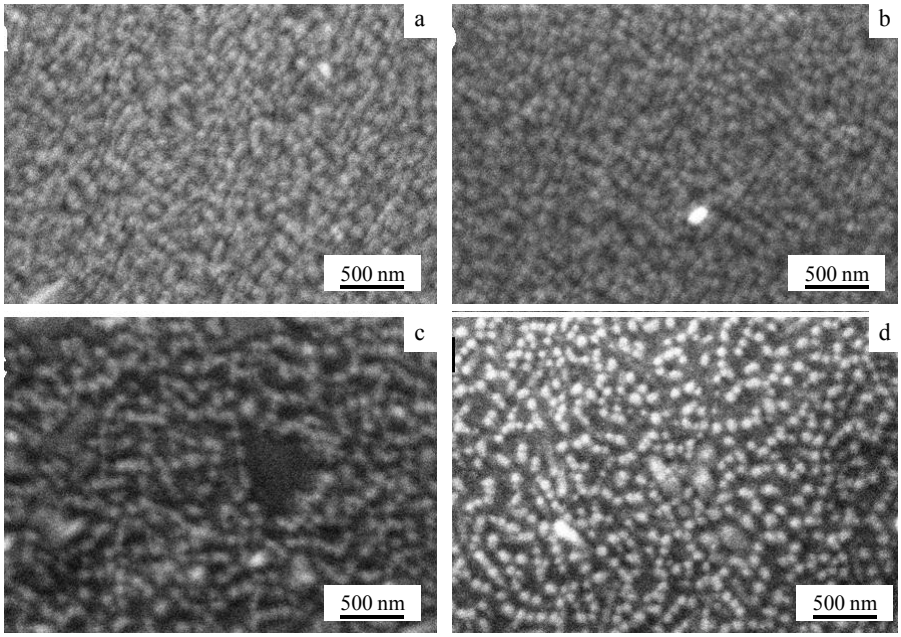

Fig. 4.2 SEM micrograph of WO_3 thin films (a) pure, (b) 1% hydrogen peroxide, (c) 4% oxalic acid and (d) 1% hydrogen peroxide and 4% oxalic acid.

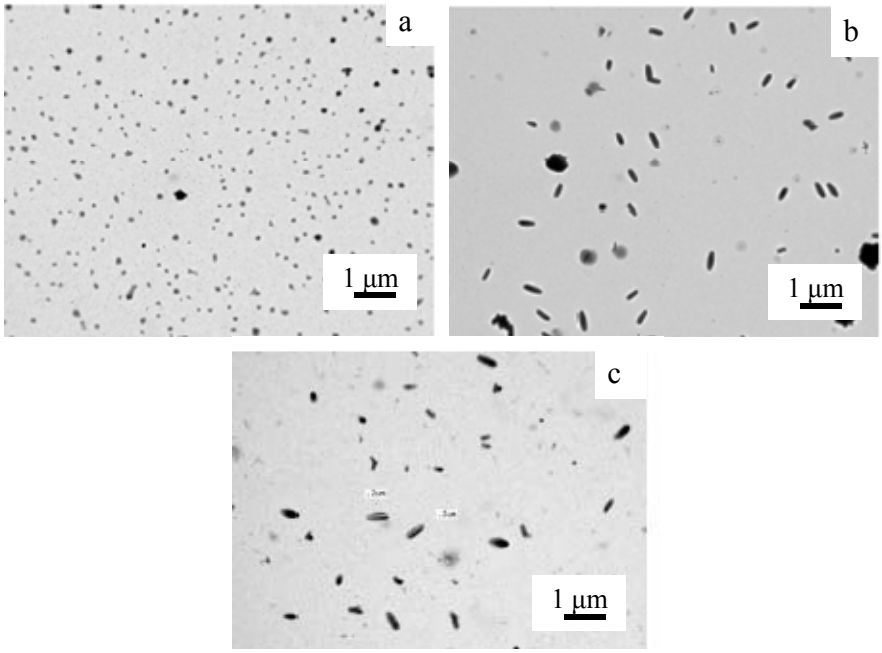

Fig. 4.3 Low magnification TEM images of WO_3 nanoparticles prepared at different additives concentrations; (a) No additives, (b) 1 % hydrogen peroxide and (c) 4 % oxalic acid.

4.3.3 FTIR measurements

Figure 4.4 shows FTIR spectra of the WO_3 thin films with different additives. Peak at 3442 cm^{-1} is referred to water, which increased by adding additives due to porous structure as illustrated by SEM micrographs (Fig. 4.2). WO_3 prepared by adding oxalic acid was characterized by the strong band at 1545 cm^{-1} corresponding to COO group [21] as shown in Fig. 4.4(c) and Fig. 4.4(d). There is almost no deference between Fig. 4.4(c) and (d). This means that hydrogen peroxide has no effect on sample prepared by adding oxalic acid because that the oxalic acid has more chemical stability due to delocalized negative charge on the two oxygen atoms. Peak at 628-630 cm^{-1} is referred to O-W-O. Vijayalakshmi et al. [22] recorded the same peak at 674 cm^{-1} for electrodeposited WO_3 thin films. Peak at 977 cm^{-1} is referred to W=O, in good agreement with results obtained by Deepa et al. [11].

4.3.4 Optical measurements

Figure 4.5 reviews the effect of additives on WO_3 thin films transmittance spectra. The pure WO_3 thin film (Fig. 4.5(a)) shows some interference fringes because of smooth surfaces due to uniform distribution of WO_3 particles on the substrate (Fig. 4.2(a)) which disappeared in the other thin films owing to some roughness caused by additives (Fig. 4.2 (b),(c),(d)).

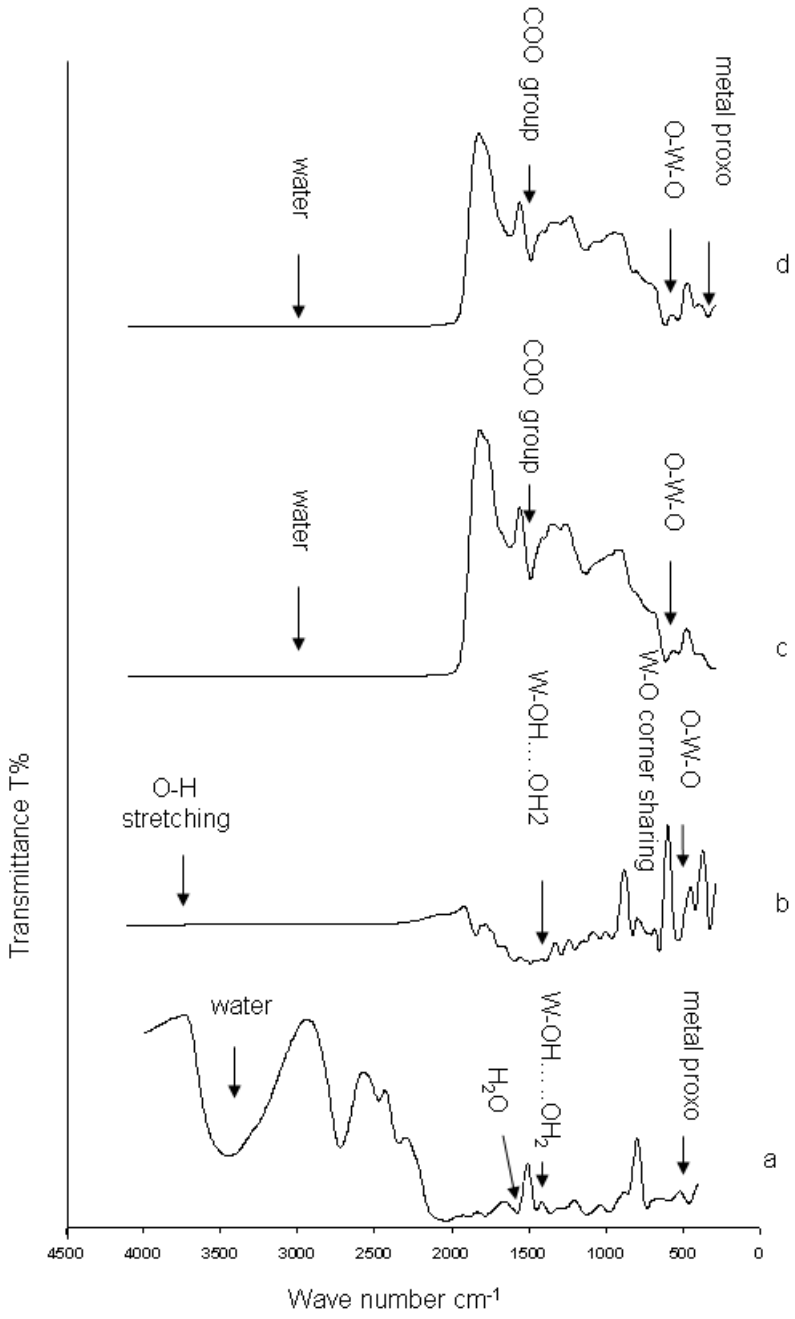

Fig. 4.4 FTIR spectra of WO_3 thin films (a) pure, (b) 1% hydrogen peroxide, (c) 4% oxalic acid and (d) 1% hydrogen peroxide and 4% oxalic acid.

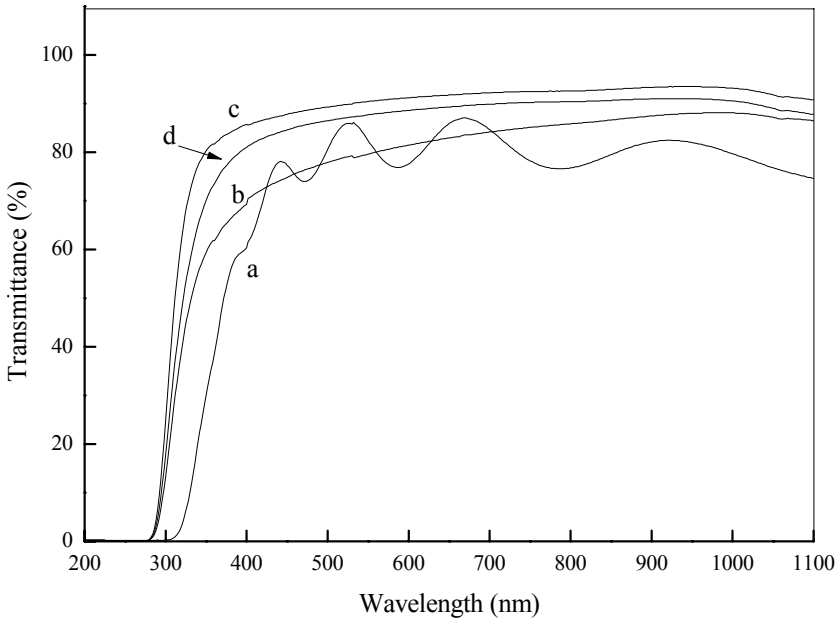

Fig. 4.5 Transmittance spectra of WO_3 thin films (a) pure, (b) 4% oxalic acid, (c) 1% hydrogen peroxide and (d) 1% hydrogen peroxide and 4% oxalic acid.

4.3.5 Electrochemical measurements

Cyclic voltammetry was used to obtain the electrochemical properties of the WO_3 thin films under oxidation state. The main parameter that will be determined from cyclic voltammetry is the current peak I_p, which depends strongly on the diffusion coefficient. Anodic peak refers here to the current peak caused by insertion of Li^+ ions into the WO_3 thin films, while the cathodic peak refers to exertion of Li^+ ions.

Figures 4.6,7 show the cyclic voltamograms of WO_3 thin films, the anodic peak increased by adding hydrogen peroxide and oxalic acid due to open porous structure as explained by Z.Ya et al. [23]. Wei Cheng [24] stated that the charge transfer depends on the proton – injecting contact (electrolyte-WO_3 interface), surface area, pore size and the porosity affected by additive as shown in Fig.4.2.

The diffusion coefficient D of lithium ions (Li^+) was calculated using Randles-Sevcik equation [25]:

$$i_p = 2.69 \times 10^5 n^{3/2} A D^{1/2} C v^{1/2} \qquad (4\text{-}1)$$

Where i_p is the anodic peak current (Amp.) at oxidation state, n is the number of electrons transferred (n = 1 in this case), A is the electrode area (cm^2), D is the diffusion coefficient (cm^2/s), C is the concentration of the electrolyte (mol/cm^3), and v is the voltage scan rate (V/s). The results in Table 4.1 summarize the diffusion coefficient values for WO_3 thin films prepared with different additives. The highest diffusion coefficient is 3.0×10^{-9} cm^2/C recorded for the sample with 1% hydrogen peroxide and 4% oxalic acid. The water content and the porosity play a great role in the diffusion coefficient by increasing the diffusion coefficient value with the H^+ ions.

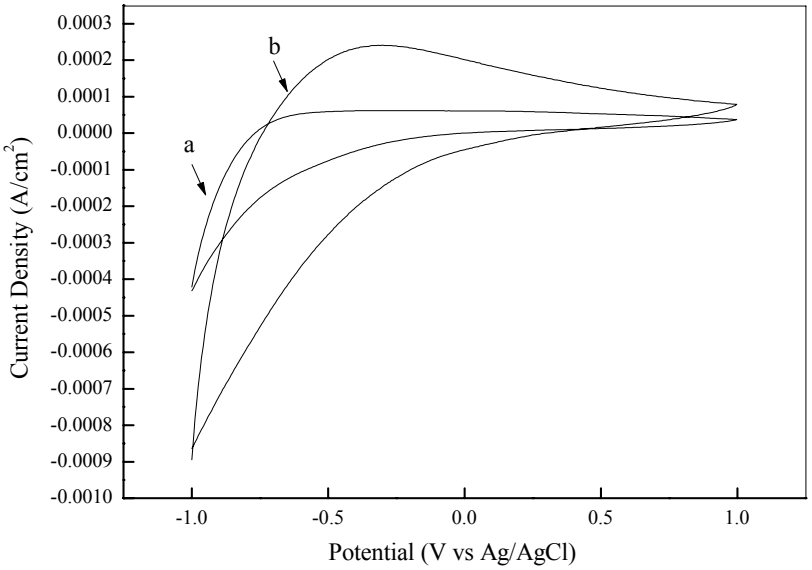

Fig. 4.6 Cyclic voltamogram of WO_3 thin films (a) pure and (b) with 1% hydrogen peroxide.

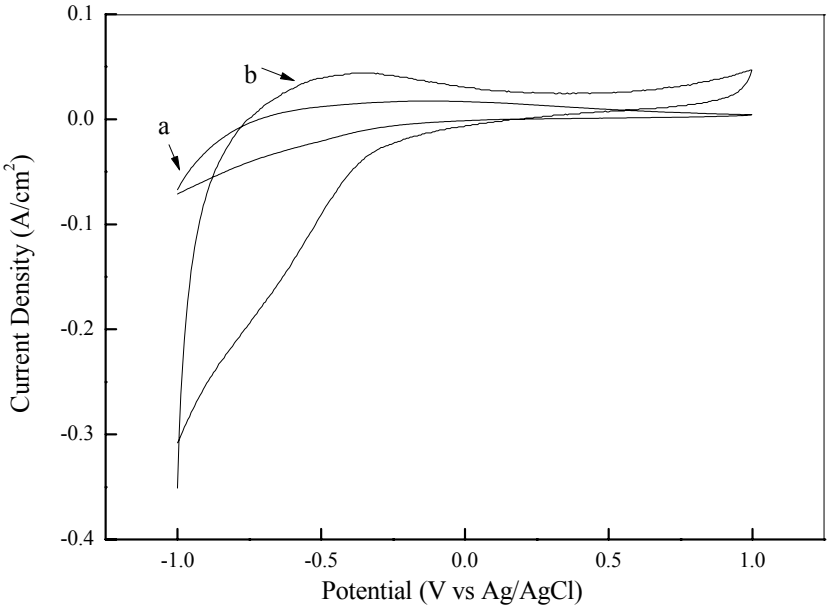

Fig. 4.7 Cyclic voltamogram of WO_3 thin films (a) with 4% oxalic acid and (b) with 1% hydrogen peroxide and 4% oxalic acid.

The transmittance that the human eye perceives is called luminous and the maximum sensitivity corresponds to the photon wavelength of 550 nm. The coloration efficiency, η, was calculated at constant λ=550 nm by applying a constant current on it (I=1mA) in a solution of 1M $LiClO_4$/PC for 60 seconds.

The charge, Q, we inserted in the sample, (area A = 3 cm^2) is: Q=I x t = 0.001 x 60=0.06 C, Q/A= 0.06/3 = 0.02 C/cm^2

By using the equation (4-2), η can be calculated as follows:

$$\eta = \frac{\Delta OD}{\Delta Q} = \frac{\log(T_b / T_c)}{(Q/A)} \qquad (Cm^2/C) \qquad (4\text{-}2)$$

Where ΔOD is the optical density difference, T_b and T_c are transmittance at colorless and colored status respectively as shown in Fig. 4.8.

Table 4.1 summarizes the results of coloration efficiency, presenting the highest calculated coloration efficiency in this work to be 63.59 cm^2/C for the sample with 1% hydrogen peroxide and 4% oxalic acid. These result are higher than other results (34 - 47.6 cm^2/C) obtained by Deepa et al. [11], while Zayim got coloration efficiency of (63 cm^2/C) by sol gel starting form WCl_6 at 650 nm with 1% TiO_2 [26].

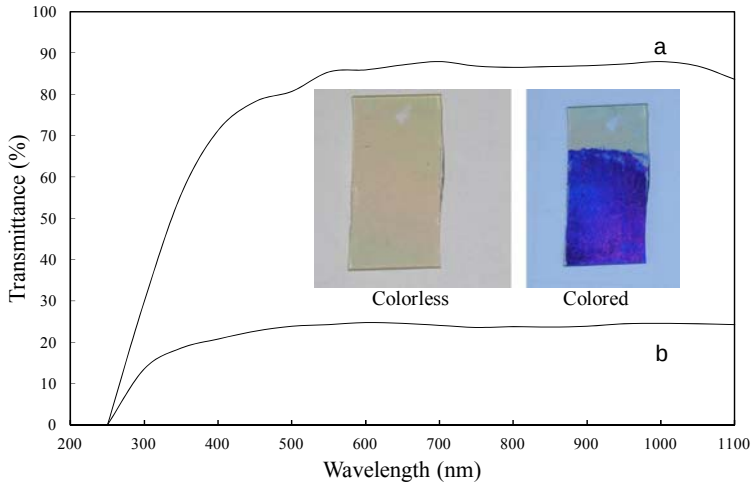

Fig. 4.8 Transmittance spectra of WO_3 thin films with 1% hydrogen peroxide and 4% oxalic acid at (a) colorless state and (b) colored state.

Table 4.1 WO_3 thin films preparation conditions and performance.

	Sample 1	Sample 2	Sample 3	Sample 4
W^+ion concentration	0.1 M			
additives	No	1% hydrogen peroxide	4% oxalic acid	1% hydrogen peroxide and 4% oxalic acid
Deposit	Spinner at 200 rpm for 60s			
Heat Treatment	300 ^oC for 30 min			
Size (nm)	46.2	49.8	44.5	12.3
Transmittance T% (at 550 nm)	82.4	90.4	79.6	87.7
Diffusion coefficient (C/cm^2)	5.3×10^{-14}	8.3×10^{-14}	4.2×10^{-10}	3×10^{-09}
Coloration Efficiency (cm^2/C)	8.5	19.5	45.15	63.59

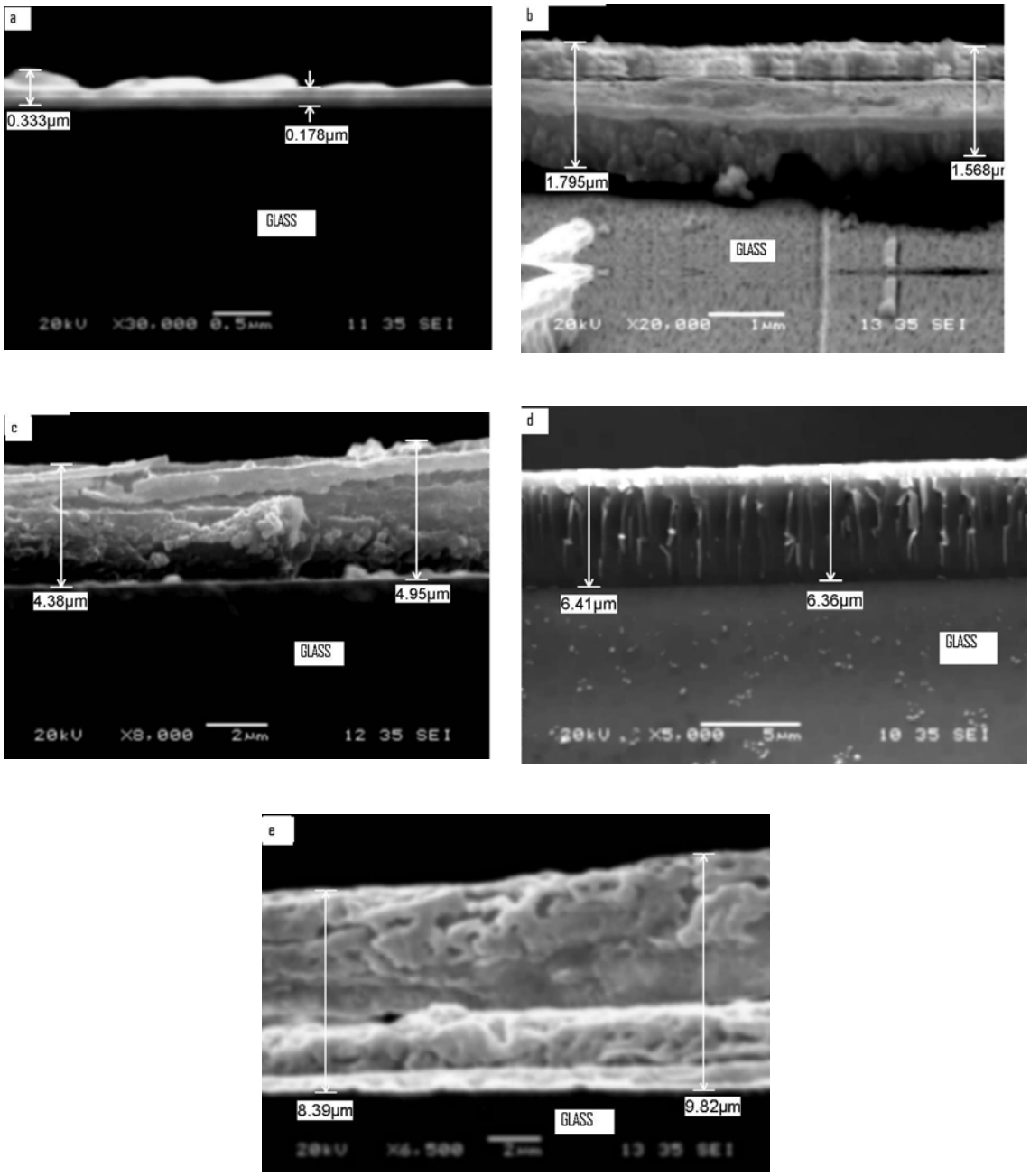

Fig. 4.9 Cross-section SEM micrograph of (a) one layer of WO_3 thin film, (b) two layers, (c) four layers, (d) six layers and (e) eight layers.

Table 4.2 Thickness of WO_3 with 1% hydrogen peroxide and 4% oxalic acid thin films and their coloration efficiency.

No. of layers	1	2	4	6	8
Thickness (μm)	0.17– 0.33	1.6 – 1.8	4.38 – 4.95	6.36 – 6.4	8.39 - 9.82
Q (C/cm_2)			0.02		
(T_b/T_c)	3.568	3.611	2.745	2.406	2.138
ΔOD (log (T_b/T_c))	1.272	1.284	1.01	0.878	0.760
Efficiency (cm^2/C)	63.6	64.2	50.5	43.9	38.3

- Multi-layer films were prepared from tungstic acid precursor contains 1% hydrogen peroxide and 4% oxalic acid.
- All WO_3 films were indexed to monoclinic WO_3 structures.

4.3.6. Thickness measurements

Figure 4.9 and Table 4.2 summarize and show thickness of the multi-layered WO_3 films with 1% hydrogen peroxide and 4% oxalic acid and coloration efficiencies of these films. The highest coloration efficiency (64.2 cm^2/C) was recorded for the two layered WO_3 film. The optical density difference of this film slightly increased than that of the one layered film. On the other hand, the coloration efficiency decreased for the four layered film, and it further decreased with increasing the number of layers because the optical density difference decreased significantly. The origin of the decrease of the optical density difference can be considered to be mainly due to decrease of the transmittance at colorless state (T_b) when the number of layers was four or more.

4.4. Conclusion

In this research, electrochromic WO_3 thin films were deposited by spin coater from solution of tungstic acid obtained using ion exchange method. The obtained thin films had low porous structure (monoclinic) which turned to open porous structure (hexagonal) by adding 1% of hydrogen peroxide and 4% of oxalic acid. These additives also increase the transmittance, diffusion coefficient and coloration efficiency. Coloration efficiency was affected also by number of layers, and the highest coloration efficiency (64.2 cm^2/C) was recorded for two layers of WO_3 thin film.WO_3 shape was turned from spherical nanoparticle with diameter of 50-200 nm to rod with diameter of 20-50 nm by adding 1% H_2O_2, and finally to rod with diameter of 100-200 nm and 200-500 nm length by adding 4% oxalic acid.

References

[1] C. O. Avellaneda, D. F. Vieira, A. Al-Kahlout, S. Heusing, E. R. Leite, A. Pawlicka, M. A. Aegerter, Solar Energy Materials and Solar Cells 92 (2008) 228-233.

[2] W. Xiao, W. Liu, X. Mao, H. Zhu, D. Wang , Journal of Materials Chemistry A 1 (2013)1261-1269.

[3] S. A. Agnihotry, N. Sharma, M. Deepa, Journal of Sol-Gel Science and Technology 24 (2002) 265-270.

[4] C. O. Avellaneda, K. Dahmouche, L. O. S. Bulhões, A. Pawlicka , Journal of Sol-Gel Science and Technology 19 (2000) 447-451.

[5] T. Todorovski, M. Najdoski, Materials Research Bulletin 42 (2007) 2025-2031.

[6] H. Nogueira, M. V. Cavaleiro, J. Rocha, T. Trindade, J. D. Pedrosa, D. Jesus, Materials Research Bulletin 39 (2004) 683-693.

[7] B. Pecquenard, H. Lecacheux, S. C. Garcia, J. Livage, Journal of Sol-Gel Science and Technology 13 (1998) 923-927.

[8] Y. G. Choi, G. Sakai, K. Shimanoe, N. Miura, N. Yamazoe, Sensors and Actuators B: Chemical 87 (2002) 63-72.

[9] S. Supothina, P. Seeharaj, S. Yoriya, M. Sriyudthsak, Ceramics International 33 (2007) 931-936.

[10] J. Livage, G. Guzman, Solid State Ionics 84 (1996) 205-211.

[11] M. Deepa, T. K. Saxena, D. P. Singh, K. N. Sood, S. A. Agnihotry, Electrochimica Acta 51(2006) 1974-1989.B.

[12] Y. G. Choi, G. Sakai, K. Shimanoe, N. Yamazoe, Sensors and Actuators B: Chemical 101(2004) 107-111.

[13] S. R. Bathe, P.S. Patil, Solid State Ionics 179 (2008) 314-323.

[14] G. Gerand, J. Nowogrocki, A. Guenot, M. Figlarz, Journal of Solid State Chemistry

29 (1979) 429-434.

[15] J. Wang , E. Khoo , P. S. Lee, J. Ma, The Journal of Physical Chemistry C 113 (2009) 9655-9658.

[16] C. G. Granqvist, E. Avendaño, A. Azens, Thin Solid Films 442 (2003) 201-211.

[17] I. V. Shiyanovskaya, Journal of Non-Crystalline Solids 187 (1995) 420-424.

[18] W. Luo, X. K. Fu, L. H. Ma, Chinese Chemical Letters 18 (2007) 883-886.

[19] K. J. Patel, C. J. Panchal, V. A. Kheraj, M. S. Desai, Materials Chemistry and Physics 114 (2009) 475-478.

[20] N. Sharma, M. Deepa, P. Varshney, S. A. Agnihotry, Journal of Sol-Gel Science and Technology 18 (2000) 167-173.

[21] A. Patra, K. Auddy, D. Ganguli, J. Livage, P. K. Biswas, Materials Letters 58 (2004) 1059-1063.

[22] R. Vijayalakshmi, M. Jayachandran, C. Sanjeeviraja, Current Applied Physics 3 (2003) 171-175.

[23] Z. Yu, Xi. Jia, J. Du, Ji. Zhang, Solar Energy Materials and Solar Cells 64 (200) 55-63.

[24] W. Cheng, E. Baudrin, B. Dunn, J. I. Zink , Journal of Materials Chemistry 11 (2001) 92-97.

[25] A. K. Srivastava, M. Deepa, S. Singh, R. Kishore, S. A. Agnihotry, Solid State Ionics 176 (2005) 1161-1168.

[26] E. O. Zayim, Solar Energy Materials and Solar Cells 87 (2005) 695-703.

Chapter 5

Fabrication of Tungsten Oxide Thin Film by Electrodeposition Method

Abstract

Electrochromic tungsten oxide thin films were fabricated by galvanostatic electrodeposition. The effect of preparation parameters such as tungsten ions concentration, pH, current density and annealing on the properties and performance of WO_3 thin films electrochromic materials were investigated. Triclinic WO_3 structure was prepared at 0.1 M of W^+ and current density of 0.5 mA/cm^2, while at 0.2 M of W^+, and 1 mA/cm^2, orthorhombic structure was revealed. The highest diffusion coefficient of 6.81×10^{-11}cm^2/S and coloration efficiency of 62.6 cm^2/C were obtained for the films prepared at pH 2, 1 mA/cm^2, and 0.1 M of W^+.

5.1 Introduction

Various applications such as large area displays, smart windows, sun roofs, anti-dazzling rear-view mirror in cars, eye-wear in ski goggles, and visors in motorcycle helmets are based on electrochromic materials that modify their optical properties (transmittance/reflectance) in reversible manner under the influence of electric current [1]. Electrochromic materials include organic compounds, as conducting polymers and inorganic compounds i.e. semiconductor transition metal oxides. Among various semiconductor materials, tungsten oxide (WO_3) and its thin films were drew the attention of many scientists due to their good electrochemical activity, fast switching kinetics, high coloration efficiency, and high chemical stability [2]. Several techniques have been applied to fabricate tungsten oxide thin films including chemical vapor deposition (CVD) [3], sputtering [4,5], sol–gel [6-8], and electrodeposition [9-12]. Electrodeposition technique has more advantages than other techniques as it is simple, cheap, and could be applied for large scale [11]. Many research attempts have been made to prepare WO_3 thin films using electrodeposition technique i.e. Agnihotry et al. [9] who deposited, potentiostatically, WO_3 thin films at -0.45 V for 10 min from 50% ethanolic solution of peroxopolytungstic acid (PPTA). They studied the annealing effect on the electrochromic performance and achieved coloration efficiency of 77 cm^2/C at 60 ^oC [13]. In 2006, the same group [14] investigated the effect of sodium dodecyl sulfate (SDS) on the electrochromic performance and grain size. They reached coloration efficiency of 60–78 cm^2/C for 600 nm film thickness annealed at 100 ^oC. Tsirlina et al. [12,15] started with sodium tungstate dissolved in water and adjusted the pH value by adding sulfuric acid. They studied the structure and electrochromic performance of the films deposited at different potentials and various times. Galvanostatic fabrication of WO_3 thin films was managed by Kolbasoc et al. [16] from sodium tungstate solution with hydrogen peroxide at pH of 0.8–2.0. Electrodeposition of

WO_3 is electron transfer controlled-reaction, in which the reaction rate is proportional to the current density. Therefore, in galvanostatic deposition process, the applied current is constant and, consequently, the reaction rate is constant. The resultant deposits will demonstrate homogeneous morphology and good adhesion to the substrate, which yield high quality WO_3 thin films using a cheap and simple technique.

The aim of this study is to produce high efficiency electrochromic tungsten oxide thin films using a simple galavanostatic deposition as convenient method, which is simple and produces high quality thin films. Thin films of nanostructured tungsten oxide prepared throughout this study were galvanostatically deposited. All essential experimental conditions to optimize the film quality and electrochromic performance of tungsten oxide thin films have been considered. XRD, SEM–EDS, TEM, FTIR, UV–VIS spectrophotometry, and electrochemical measurements were utilized to characterize the structural and compositional properties as well as the electrochromic behaviour of the prepared thin films.

5.2. Experimental

5.2.1 Preparation of WO_3 thin films

The substrate was 3 cm^2 glass slides coated with indium tin oxide (ITO) and the sheet resistance was 14 Ω/□ [17]. The substrate surface was rinsed with distilled water, and ultrasonically cleaned in ethanol bath for 15 min. Then it was dried at room temperature. Acidic tungstate solutions of tungstic acid (H_2WO_4) have been prepared by dissolving sodium tungstate (98%, Sisco research laboratory, India) in double distilled water and stirred for 5 min at room temperature to get 0.05, 0.1, and 0.2 M of tungstic acid clear

solutions. Hydrogen peroxide (30%) was added to these solutions, and mixture was stirred for another 5 min to give 1: 0.03 molar ratio of [H_2WO_4] : [H_2O_2] as reported by Yu et al. [18]. The pH value was adjusted at 2 and 2.5 by sulfuric acid (95–97%, Aldrich, Germany). Thin films were formed by galvanostatic electrodeposition technique using PGS 95 (Wenking, Germany) potentiostat. The electrochemical cell consisted of tungstic acid solution as the electrolyte, 4 cm^2 platinum plate as the counter electrode, and 3 cm^2 ITO-coated glass as the working electrode. Electrodeposition occurred at different current densities, J, of 0.5, 0.75, 1.0 and 1.5 mA/cm^2. The Prepared WO_3 thin films were dark blue color, which rinsed immediately with deionized water and dried in air. After thin film preparation, some selected films were annealed at 450 ^oC for 60 min in air furnace (Carbolite, Aston lane, Hope Sheffield, 530 2RR, England) to investigate the effect of heat treatment on the film properties.

5.2.2 Characterization of WO_3 thin films

X-Ray diffraction patterns (XRD) of the electrodeposited thin films were obtained by X-ray diffractometer (Shimadzu 7000, USA) operating with Cu–Kα radiation (λ = 0.154060 nm) generated at 30 kV and 30 mA. The scan rate was 2θ /min for 2h values between 20 and 80 degrees. The surface of tungsten oxide thin films was investigated with high resolution scanning electron microscopy (SEM) (JEOL JSM 6360LA, Japan) to examine the morphology and the homogeneity of the surface. Thin films of gold were sputtered onto the samples to get charge free surfaces. Also, measurements of various grain sizes were estimated from the SEM micrographs. Transmission electron microscopy (TEM) (JEOL JEM 1230, Japan) operating at 120 kV was used to determine the size of WO_3 nanoparticles. WO_3 thin films were stripped out from ITO substrate and suspended in ethanol and then spreaded on the copper grid for the TEM measurements. The transmission (T) and

absorption (Abs) of the prepared thin films were measured using Double beam UV–VIS Spectrophotometer (Labomed, USA). The measurements were carried out in the range 190 - 1100 nm at room temperature. Vibrational spectroscopic studies for as-deposited and annealed WO_3 thin films were obtained by Fourier transform infra red (FTIR) spectrophotometer (Shimadzu, 8400 S, Japan) at room temperature in the frequency range 4000–500 cm^{-1}.

5.2.3 Electrochromic properties of WO_3 thin films measurements

The electrochemical set-up consisted of a potentiostat (Voltalab PGP201,Radiometer Analytical,France) controlled by a computer and conventional three-electrode cell in which the saturated calomel electrode (SCE) and a platinum wire were used as reference and counter electrodes, respectively. Tungsten oxide on ITO-coated glass was used as the working electrode in an electrolyte of 1M lithium perchlorate ($LiClO_4$, 98% Fluka, Switzerland) in propylene carbonate (PC, 99% Aldrich, Germany) [19]. The CV's were recorded in the range 0–1 V versus SCE with a scan rate of 10 mV/s. All the measurements were carried out at room temperature. The cyclic voltammograms were recorded after 10 activation cycles. Electrochromic measurements were recorded using a systemconsists of potentiostat and spectrophotometer by connecting samples to potentiostat when placed inside the spectrophotometer measurement compartment and by applying a current, I, of 1 mA in the solution of 1M $LiClO_4$/PC for 60 s. Then the data were recorded the change in transmittance at λ = 550 nm [20] at room temperature.

5.3. Results and discussion

5.3.1. XRD measurements

Figure 5.1 shows the XRD patterns of WO_3 thin films (after omitting the ITO peaks) deposited galvanostatically at current density of 0.75 mA/cm^2 from different W^+ ion concentrations (0.05, 0.1 and 0.2 M) at pH 2. At low W^+ ion concentration of 0.05 M (Fig. 5.1(a)), a broad peak at 2θ =20~30 appeared referring to amorphous structure of WO_3. Increasing the W^+ concentration to 0.1 M (Fig. 5.1(b)), the triclinic structure (JCPDS card no. 20-1323) [21] of WO_3 is revealed and the (120) and (202) peaks are detected. At higher W^+ concentration of 0.2 M (Fig. 5.1(c)), the structure is orthorhombic WO_3 (JCPDS Card no. 1-071- 0131). The most intense peaks; (002) and (222) for the triclinic WO_3 structure were observed. At low W^+ concentration (0.05 M), the rate of deposition is faster than the rate of crystal growth, so more disorder occurs in the film, and amorphous phase appeared (Fig. 5.1(a)). Also, the amorphous phase is hardly detected at high W^+ concentration (0.2 M) (Fig. 5.1(c)) due to accumulation between grains, which caused by increasing W^+ concentration. The average crystallite size of WO_3 is calculated from the full width at half-maximum (FWHM) of the diffraction peak using Debye-Scherrer's equation [22]:

$$D = \frac{0.9\lambda}{B_{2\theta}\cos\theta_{\max}} \text{ Å} \qquad (5.1)$$

Where D is the average crystallite size in Å, λ is the characteristic wavelength of X-ray used (1.5406 Å), θ is the diffraction angle, and $B_{2\theta}$ is the angular width in radians at intensity equal to half of the maximum peak intensity. The obtained WO_3 thin films have crystalline size of 15.8 nm increased to 18.6 and 21.2 nm as the W^+ concentration increased in the solution from 0.05 M to 0.1 M then to 0.2 M, respectively.

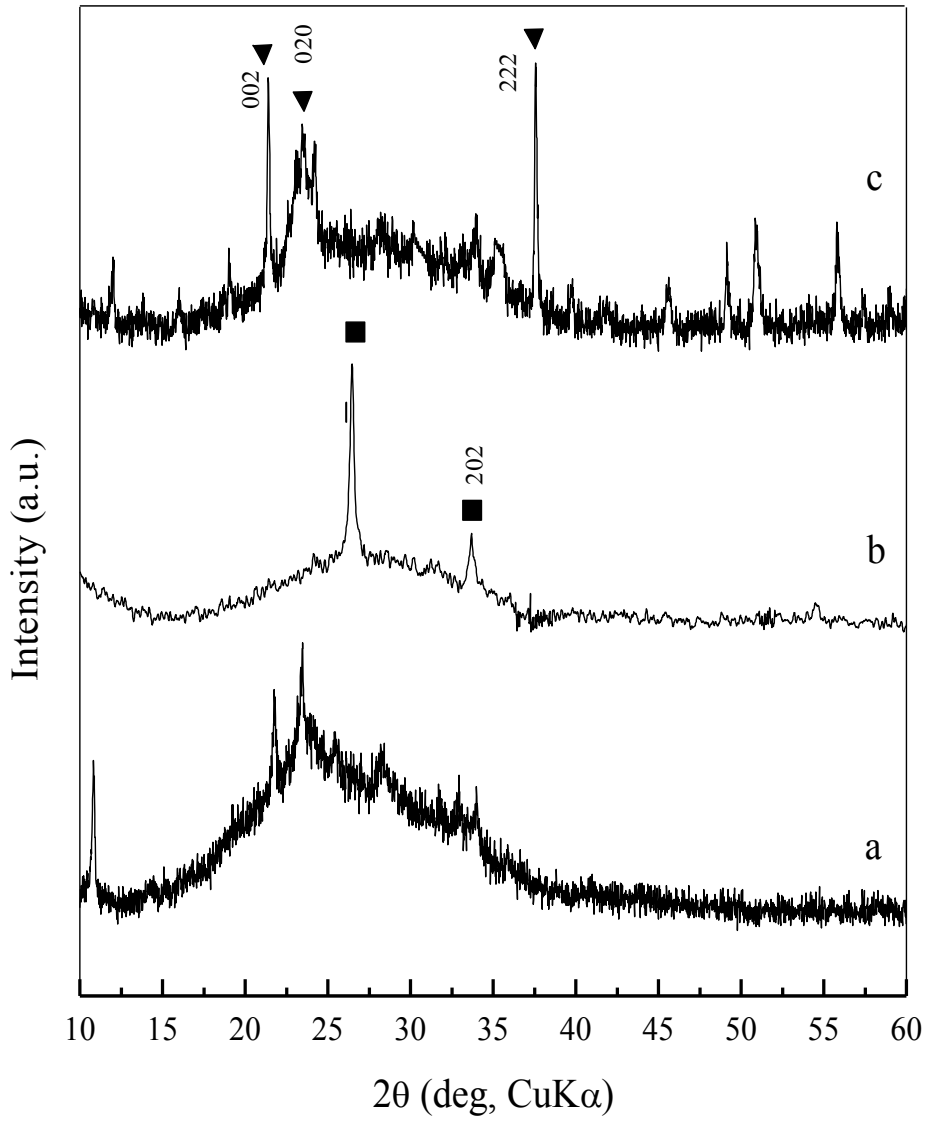

Fig. 5.1 XRD patterns of WO_3 thin films deposited at pH 2 and 0.75 mA/cm^2 from different W^+ concentrations: (a) 0.05 M, (b) 0.1 M and (c) 0.2 M.

■ symbol refers to the triclinic peaks, while ▼refers to orthorhombic peaks.

Figure 5.2 illustrates the XRD patterns of WO_3 thin films (after omitting the ITO peaks) deposited at different current densities; 0.5 mA/cm^2 (Fig. 5.2 (a)), 0.75 mA/cm^2 (Fig. 5.2 (b)), and 1 mA/cm^2 (Fig. 5.2 (c)) for W^+ ion concentration of 0.1 M at pH 2. At low current density, 0.5 and 0.75 mA/cm^2, the triclinic WO_3 structure is the dominant phase and (120) plane is highly oriented (JCPDS Card no. 20-1323). At higher current density, 1 mA/cm^2, the WO_3 has the orthorhombic structure (JCPDS card no. 1-071- 0131). Our results of the triclinic WO_3 structure for galvanostatic deposition at current density of 0.5 mA/cm^2 coincide with the results obtained before by R. Vijayalakshim et al. [22].

5.3.2 Morphology evaluation

Figure 5.3 shows SEM micrographs of WO_3 thin films deposited for different W^+ concentrations at pH 2 and current density of 1 mA/cm^2. Figure 5.3 (a) represents thin film deposited for lower W^+ concentration (0.05 M), which exhibited porous structure with fine grains of about 25 nm. Fig. 5.3 (b) demonstrates that the grain size increased to about 50 nm by increasing the W^+ concentration to 0.1 M. Figure 5.3 (c) illustrates the same as in Fig. 5.3 (a) and (b), but for W^+ concentrations (0.2 M), some of the grains are agglomerated in different shapes (sheets and rods), which decrease significantly the film porosity.

Figure 5.4 presents the SEM micrographs of WO_3 thin films deposited at different current densities. WO_3 thin film deposited at lower current density (0.5 mA/cm^2) exhibited small grains and regular morphology as shown in Fig. 5.4 (a). The film morphology and quality have been improved at moderate current densities; 0.75 and 1 mA/cm^2 as explained in Fig. 5.4 (b) and (c). larger grains and some cracks began to appear in the film at higher current density (1.5 mA/cm^2).

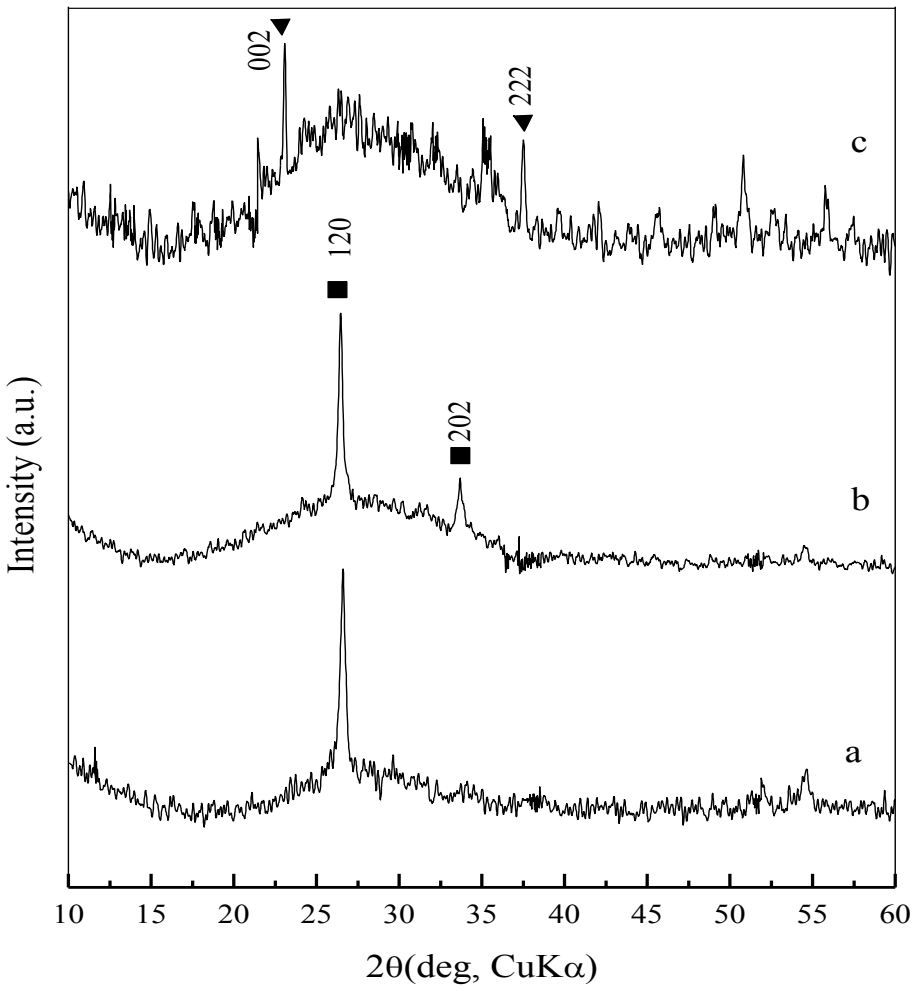

Fig. 5.2 XRD patterns of WO_3 thin films deposited at pH 2 and 0.1 M of W^+ using different current densities: (a) 0.5 mA/cm^2, (b) 0.75 mA/cm^2 and (c) 1 mA/cm^2.

■ symbol refers to the triclinic peaks, while ▼refers to orthorhombic peaks.

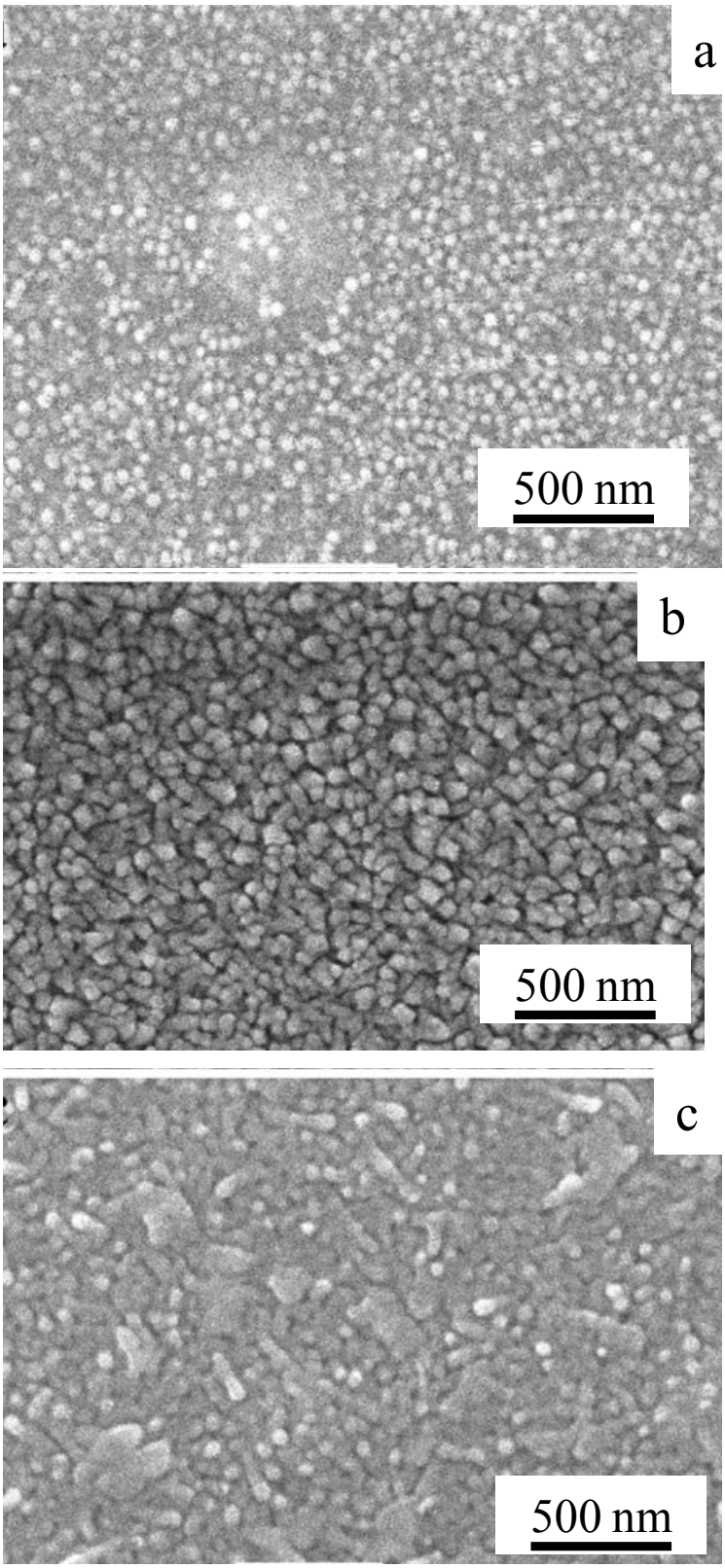

Fig. 5.3 SEM micrographs of WO_3 thin films deposited at pH 2 and 1 mA/cm^2 from different W^+ concentrations: (a) 0.05 M, (b) 0.1 M and (c) 0.2 M.

Figure 5.5 shows the TEM micrograph of the WO_3 thin film deposited from 0.1 M of W^+ solution at pH 2 and 1 mA/cm^2. Regular WO_3 nanoparticles of 20–23 nm are noticeable, which is in good agreement with the crystallite size calculated from XRD.

5.3.3 FTIR measurements

The FTIR spectra of the as-deposited WO_3 thin films prepared at pH 2, 0.1 M of W^+ ions and current density of 0.5 mA/cm^2, and the film annealed at 450 ^oC for 60 min are shown in Fig.5.6. The as-deposited thin film (Fig. 5.6(a)) reveals a strong peak detected at 1,620 cm^{-1} indicating the presence of (HOH) water content [13]. The intensity of this peak decreased upon annealing (Fig. 5.6 (b)). The stretching vibrational mode of (W=O) bond is strongly identified at 968 cm^{-1} for both as-deposited and annealed films [13]. Vibrational bands at 940, 808, 718, 605 and 574 cm^{-1} of triclinic WO_3 ceramic samples were observed by Fihlo et al. [23]. The as-deposited sample reveals the triclinic WO_3 structure identified at 968 cm^{-1} for both as-deposited and annealed films [13]. Vibrational bands at 940, 808, 718, 605 and 574 cm^{-1} of triclinic WO_3 ceramic samples were observed by Fihlo et al. [23]. The as-deposited sample reveals the triclinic WO_3 structure.

5.3.4 Optical measurements

Figure 5.7 shows the effect of W^+ concentration on thin film transmittance at pH 2 without heat treatment at 1.0 mA/cm^2. It is observed that the sample which deposited from 0.1 M of W^+ (Fig. 5.7 (b)) has higher transmittance, ~10% more than other concentrations in the region of visible light as compared to Fig. 5.7 (a) and (c). This result agreed with the previous morphology graphs (Fig. 5.3 (b)), which exhibited good thin film morphology accompanied by high porosity.

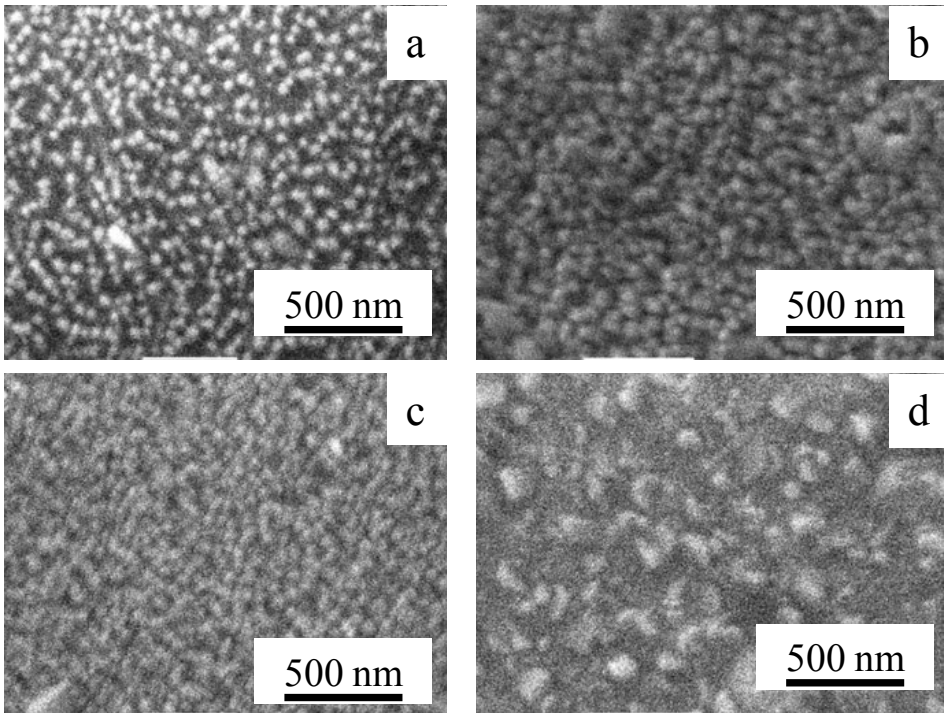

Fig. 5.4 SEM micrographs of WO_3 thin films deposited at pH 2, 0.1 M of W^+ using different current densities of : (a) 0.5 mA/cm^2, (b) 0.75 mA/cm^2, (c) 1 mA/cm^2 and (d) 1.5 mA/cm^2.

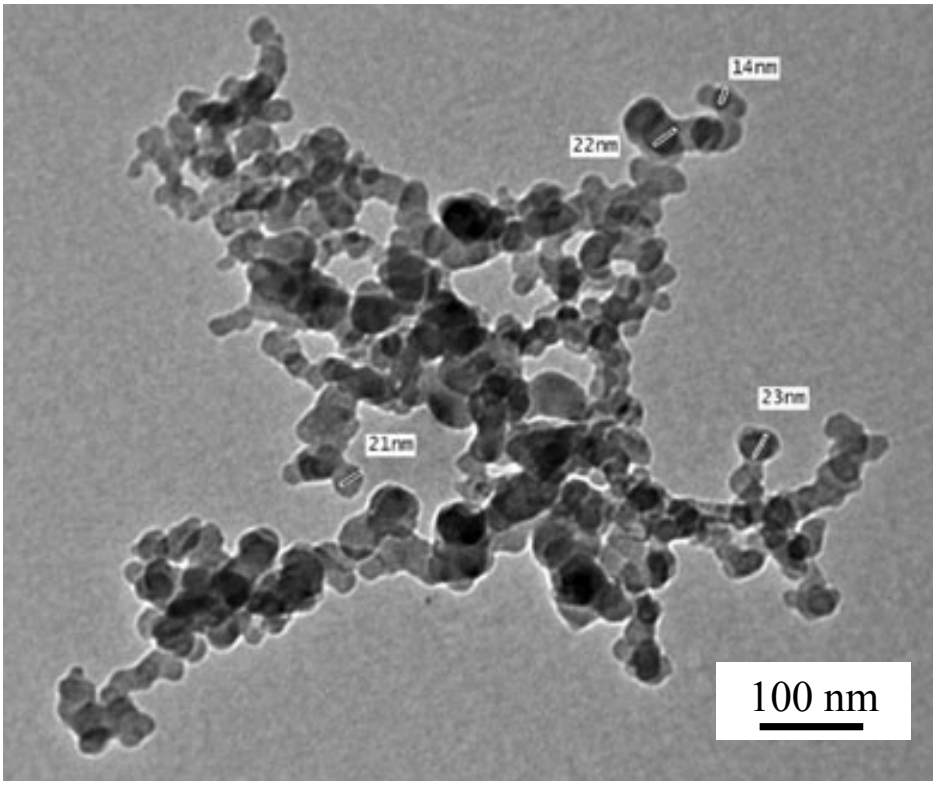

Fig. 5.5 TEM image of WO_3 thin films deposited from 0.1 M of W^+ at pH 2 and current density of 1 mA/cm^2.

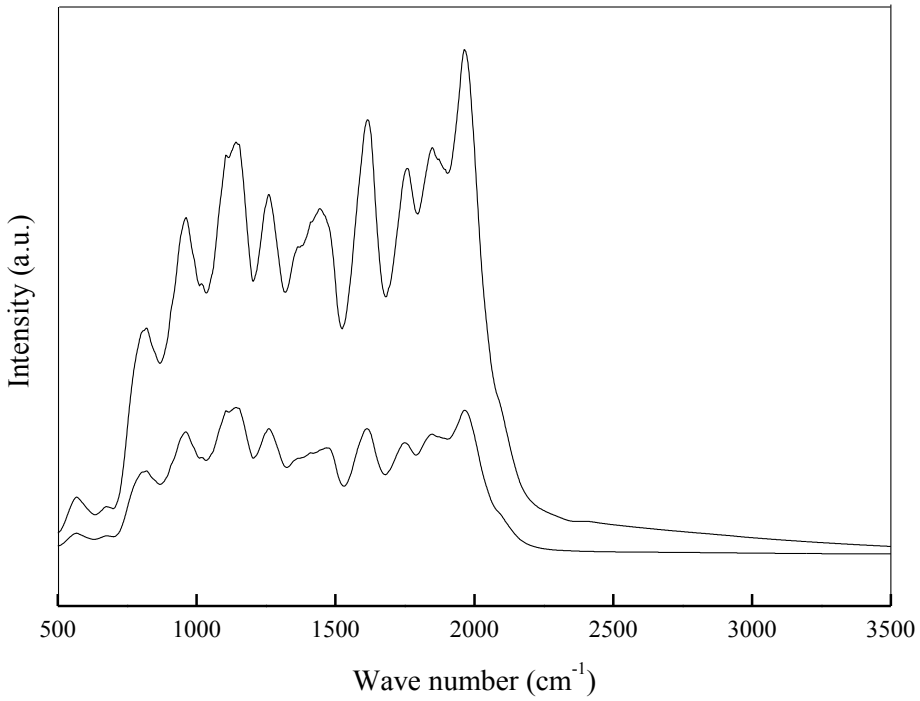

Fig. 5.6 FTIR spectra of (a) as- deposited WO_3 thin film and (b) WO_3 thin film annealed at 450 ^oC for 60 min for the WO_3 thin films prepared at pH 2, 0.1 M of W^+ ions and current density of 0.5 mA/cm^2.

M. Deepa et al. [13] reported that the transmittance correlated with the open porous structure and the transmittance values were increased with increasing pH, which may be due to change in morphology, as discussed above. The number of electrons and holes in a semiconductor is determined by the value of the electronic band gap; E_g. Tungsten oxide has an indirect band gap, E_g [1], and is calculated as described before in section 3.3.2.

Table 5.2 shows the band gap values for WO_3 thin films prepared at different experimental parameters (current density, W^+ concentration, pH, and annealing temperature at 450 ^oC for 60 min). The band gap values ranged from 2.8 to 3.3 eV. The highest band gap value (3.3 eV) was obtained for films prepared at pH 2.5 and 0.75 mA/cm^2, while for the annealed sample at 450 ^oC for 60 min.

5.3.5 Electrochemical measurements

Cyclic voltammetry was used to obtain the electrochemical properties of WO_3 thin films under oxidized state. Current peak, i_p, which depends strongly on the diffusion coefficient, can be determined from the cyclic voltammograms. Anodic peak refers here to the current peak caused by insertion of Li^+ ions into the WO_3 thin films, while the cathodic peak refers to exertion of Li^+ ions. Fig. 5.8 gives the cyclic voltammograms of WO_3 thin films deposited at pH 2 and 1 mA/cm^2. It is observed that the highest anodic peak, which is clearly detected at -0.55 V vs. SCE was recorded for the sample deposited from 0.1 M of W^+. This may be due to the enhancement in morphology and porous structure as Kolbasos et al. [16] reported. In the paper, the film deposited at 1 mA/cm^2 has the highest water content as measured by FTIR, or in another words, it has the highest current peak since the cyclic voltammetric path way depends on water content. Also, the current intensity peak reduced

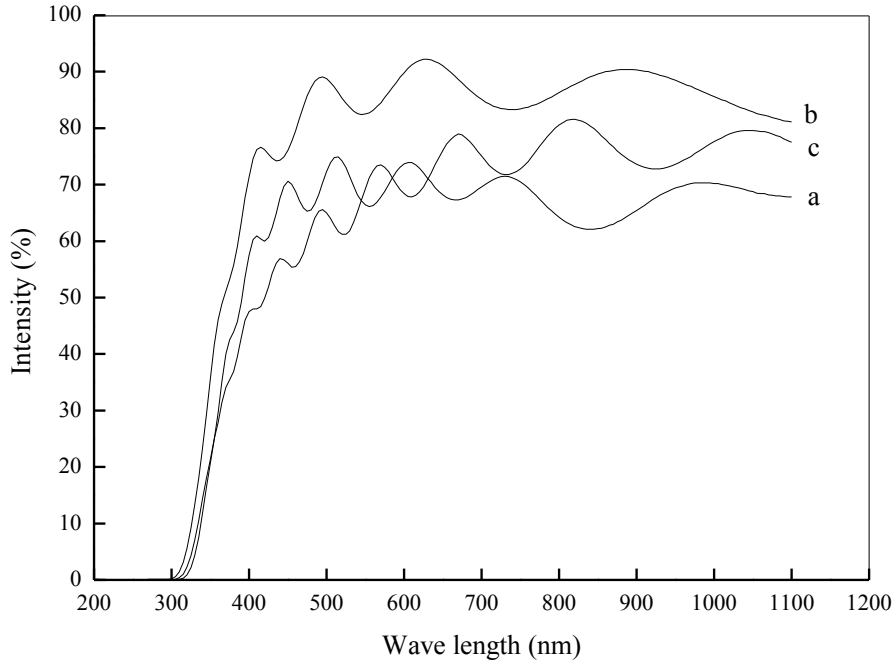

Fig. 5.7 Transmission spectra of WO_3 thin films deposited at pH 2 and 1 mA/cm^2 from different W^+ concentrations: (a) 0.05 M, (b) 0.1 M and (c) 0.2 M.

Table 5.2 Band gap values in (eV) for the WO_3 thin films prepared at different preparation conditions.

		Without annealing				With annealing (450 ^{o}C / 60 min)			
J (mA/cm^2)		0.5	0.75	1.0	1.5	0.5	0.75	1.0	1.5
0.05M	pH 2	3.05	3	2.95	-	2.9	2.92	3.5	-
	pH 2.5	3.12	3.3	3.2	-	3.2	3.1	3.15	-
0.1M	pH 2	3.05	3	3.1	3.2	3.17	2.9	3.15	3
	pH 2.5	3.3	3.2	3.17	3.12	3.25	3.1	2.85	2.8
0.2M	pH 2	2.98	3.11	3.2	-	3.16	2.85	3	-
	pH 2.5	3.15	2.8	3.05	-	3.25	3.05	3	-

with increasing pH. This may be due to the reduction in the porosity, which caused by annealing as well as reducing the pH. Liao et al. [21] explained that the charge transfer depends on the proton—injecting contact (electrolyte — WO_3 interface), surface area, and pore size. Also, he stated that the porosity decreased by annealing, so the cyclic voltammetric peaks are greatly affected by decreasing the WO_3 surface area caused by annealing. Diffusion coefficient was calculated from cyclic voltammetry using the Randles-Servcik equation [19] :

$$i_p = 2.69 \times 10^5 n^{3/2} A D^{1/2} C v^{1/2} \tag{5.3}$$

where i_p is the anodic peak current in amps., n is the number of electrons transferred (n = 1 in this case), A is the electrode area in cm^2, D is the diffusion coefficient in cm^2/s, C is the concentration of the electrolyte in mol/cm^3, and v is the voltage scan rate in V/s.

Table 5.3 gives the diffusion coefficient values for WO_3 thin films prepared at different conditions. The highest diffusion coefficient, 6.81×10^{-11} cm^2/s, is recorded for the sample deposited from 0.1 M of W^+ at 1 mA/cm^2. The water content and the porosity play great role in enhancing the diffusion coefficient values by increasing the H^+ in solution. Yang et al. [3] referred to the reduction in the diffusion coefficient to annealing and increase in pH as the intensity of the current peak does. This can be described as under the influence of electric field, and some of water molecules ionized. The hydrogen ions react with WO_3 to form tungsten bronze. On the other hand, annealing decreases the amount of water in the film and, consequently, the diffusion coefficient. Yang et al. [3] illustrated that the adsorbed water helps the diffusion of ions and electrons in the electrochromic modulation. Agnihotry et al. [6] obtained diffusion coefficient, $D = 2.83 \times 10^{-11}$ to 6.08×10^{-10} cm^2/s, and $D = 2.65 \times 10^{-10}$ to 3.7×10^{-10} cm^2/s for the samples prepared by electrodeposition technique and measured in similar electrolyte (1M lithium perchlorate/propylene carbonate). Avellaneda et al.[8]

reduced the diffusion coefficient from 8.6 $\times 10^{-13}$ to 1.7 $\times 10^{-9}$ cm^2/s by doping WO_3 with P, which is deposited by sol–gel technique. Berggren et al. [5] reached $D = 1\times 10^{-11}$ cm^2/s by sputtering, while Siokou et al.[25] achieved $D = 8\times 10^{-13}$ to 2×10^{-12} cm^2/s by e-beam deposition. The transmittance that the human eye perceives is called luminous and the maximum sensitivity corresponds to the photon wavelength of 550 nm [26]. The coloration efficiency, η, was calculated at constant λ = 550 nm by applying a constant current (I = 1 mA) in a solution of 1 M $LiClO_4$/PC for 60 s.

η can be calculated as follows [24,27]:

$$\eta = \frac{\Delta OD}{\Delta Q} = \frac{\log(T_b / T_c)}{(Q/A)} \qquad cm^2/C \qquad (5.4)$$

where ΔOD is the optical density difference, T_b and T_c are transmittance at colorless and colored status; respectively, as shown in Fig.5.9, Q is the inserted charge, and A is the electrode area. The prevailing model is that absorption takes place by polaron hopping and involves transition between W^{5+} and W^{6+} states, [24] which is caused by ion insertion. The prevailing model is that absorption takes place by polaron hopping and involves transition between W^{5+} and W^{6+} states, [24] which is caused by ion insertion.

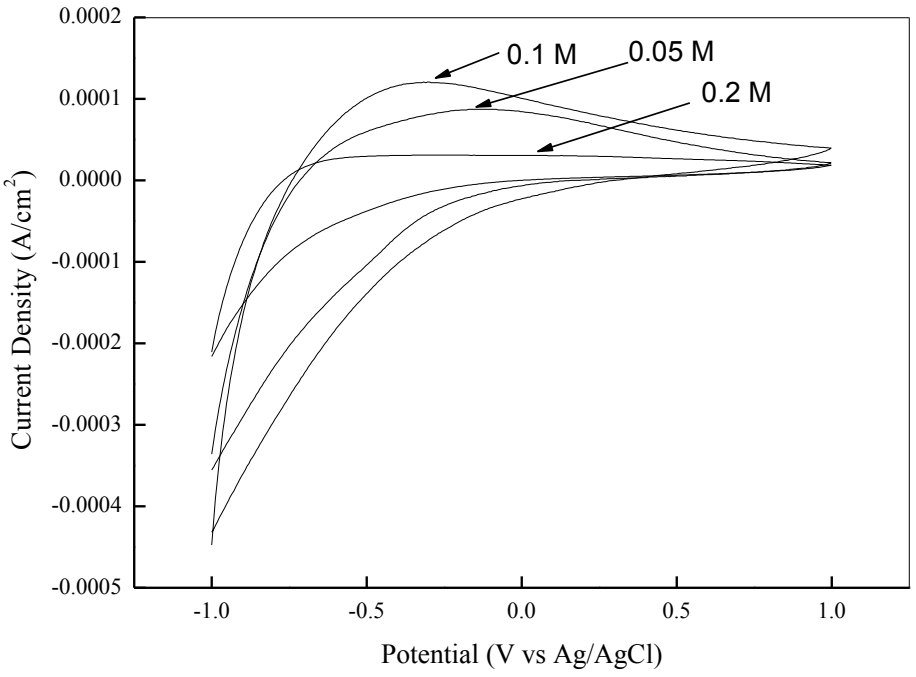

Fig. 5.8 Cyclic voltammograms of WO_3 thin films deposited at pH 2 and 1 cm^2/s from different W^+ concentrations: (a) 0.05 M (b) 0.1 M and (c) 0.2 M.

Table 5.3 Diffusion coefficient D ($\times 10^{-11}$) (cm^2/s) for the WO_3 thin films deposited at different preparation conditions.

		Without annealing				With annealing(450^{o}C /60 min)			
J (mA/cm^2)		0.5	0.75	1.0	1.5	0.5	0.75	1.0	1.5
0.05 M	pH 2	0.009	5.65	2.526	-	0.102	1.102	3.24	-
	pH 2.5	0.007	0.102	1.236	-	0.01	0.04	0.71	-
0.1 M	PH 2	0.009	3.263	6.81	4.025	0.122	1.212	4.025	0.48
	pH 2.5	0.01	0.11	1.82	0.27	0.011	0.053	0.81	0.14
0.2M	pH 2	0.008	2.43	5.32	-	0.101	1.1	3.215	-
	pH 2.5	0.008	0.102	1.37	-	0.099	0.043	0.76	-

Table 5.4 summarizes the results of coloration efficiency, presenting the highest calculated coloration efficiency in this work, which is 62.62 cm^2/C for the sample deposited from 0.1 M of W^+, at pH 2 and 1 mA/cm^2 without annealing. These coloration efficiencies are higher than results obtained before (22.97–29.37 cm^2/C) obtained by Agnihotry et al. [6] by using sol–gel technique, while Yang et al. [3] got coloration efficiency of (31.1–40.4 cm^2/C) by using DC magnetron sputtering. Tacconi et al.[28] presented coloration efficiency (65–73 cm^2/C) by doping WO_3 with (2, 4% TiO_2). Another data reported by M. Deepa and Agnihotry [29] presented coloration efficiency (52.5–81 cm^2/C) by adding oxalic acid (up to 5%), which agree with the results obtained in this work. The highest coloration efficiency value (62.62 cm^2/C) was recorded for the samples deposited from 0.1 M of W^+ ions concentration, pH 2, current density of 1.0 mA/cm^2 and without heat treatment. This may be due to the WO_3 thin films deposited from these conditions which have the highest diffusion coefficient and highest transmittance as indicated in Table 5.3 and Figure 5.7 The coloration efficiency depends on the diffusion coefficient, so it has the same trend with changing the pH value. The diffusion coefficient peak values decreased by increasing pH values. This may be due to the reduction of the porosity which caused by reducing pH value. The film deposited at current density of 1.0 mA/cm^2 has the higher water content [16], so it has the higher coloration efficiency. Coloration efficiency decreases by annealing at 450 ^oC for 60 min. This may be related to the decrease of the water content in the film due to annealing effect. Tang et al. [3] illustrated that the adsorbed water helps the diffusion of ions and electrons in the electrochromic modulation. Also, the structure of the as-deposited film is orthorhombic that is the hydrated form of tungsten oxide, $WO_3 \cdot H_2O$, which is characterized by nanosized grains embedded in a nanoporous amorphous matrix, while triclinic is only WO_3 [9].

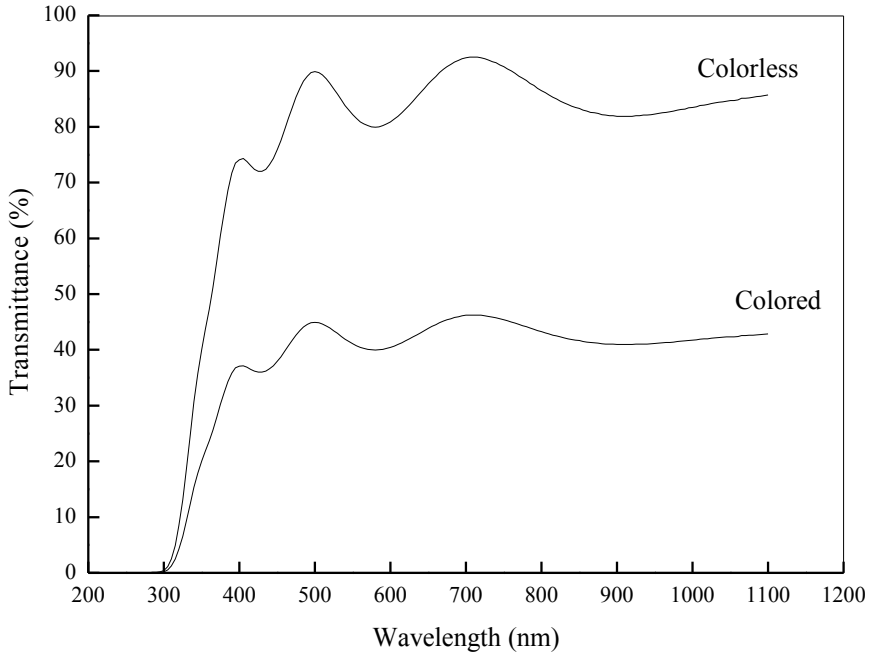

Fig. 5.9 Transmittance at colourless and coloured status of WO_3 thin films deposited from 0.1 M of W^+ at pH 2 and current density of 1 mA/cm^2.

Table 5.4 Coloration efficiency (cm^2/C) of WO_3 thin films deposited using different preparation conditions.

		Without annealing				With annealing (450 ^oC /60 min)			
J (mA/cm^2)		0.5	0.75	1.0	1.5	0.5	0.75	1.0	1.5
0.05 M	pH 2	27.7	52.54	57.4	-	9.12	45.8	53.2	-
	pH 2.5	26.5	43.77	47	-	25.6	49.66	53.24	-
0.1 M	pH 2	34.4	61.19	62.62	62.6	43.77	53.2	62.6	49.66
	pH 2.5	37	41.64	58.15	46.8	37.0	39.4	51.48	45.8
0.2M	pH 2	23.5	43.77	47.77	-	25.34	47.77	53.23	-
	pH 2.5	23.5	45.82	45.8	-	23.5	49.7	53.23	-

The degree of crystallinity increases in the triclinic, as a result, less porous, more ordered and higher density with improvement in the chemical stability of the film and the electrochromic performance were obtained. Not to mention that the hydrated or hydroxylated orthorhombic structure is beneficial for fast lithium ion insertion and extraction. Much larger effective surface area and an open structure can be exploited for faster access of the electrolyte into the film.

5.4. Conclusions

In the present comparison study, WO_3 thin films were prepared by galvanostatic electrodeposition technique under various conditions. The as-deposited thin films were amorphous structure at low current density of W^+ ion concentrations. Triclinic structure was obtained at both medium W^+ ion concentrations and current density. At high current density and W^+ ion concentration, orthorhombic structure of WO_3 was revealed. Grain size increased with increasing W^+ ions concentration, current density, and pH, while it decreased with annealing. It is necessary to mention that all grain sizes were in the nano scale (20–50 nm) which were measured by SEM and TEM. WO_3 thin films deposited from 0.1 M of W^+ ion concentration at current density of (1.0 mA/cm^2) had the highest diffusion coefficient of 6.81×10^{-11} cm^2/s , and the highest coloration efficiency of 62.62 cm^2/C was obtained.

References

[1] R. Sivakumar, M. Jayachandran, C. Sanjeeviraja, Mater. Chem. Phys 87 (2004) 439-445.

[2] E. Avendano, L. Berggren, G. A. Niklasson, C.G. Granqvist, A. Azens, Thin Solid Films 496 (2006) 30-36.

[3] T. Yang, Z. Lin, M. Wong, Appl. Surf. Sci. 252 (2005) 2029–2037.

[4] S. K. Komornicki, M. Radecka, P. Sobas, J. Mater. Sci.: Mater. Electron. 15 (2004) 527-531.

[5] L. M. Di Giulio, D. Manno, G. Micocci, A. Serra, A. Tepore, J. Mater. Sci.: Mater. Electron. 9 (1998) 317-322.

[6] S. A. Agnihotry, Sol. Energy Mater. Sol. Cells 90 (2006) 15-24.

[7] P. S. Patil, S. H. Mujawar, A. I. Inamdar, P. S. Shinde, H. P. Deshmukh, S. B. Sadale, Appl. Surf. Sci. 252 (2005) 1643-1650.

[8] C. O. Avellaneda, L. O. S. Bulhoes, Sol. Energy Mater. Sol. Cells 90 (2006) 395-401.

[9] A. K. Srivastava, M. Deepa, S. Singh, R. Kishore, S. A. Agnihotry, Appl. Surf. Sci. 252 (2005) 1568-1580.

[10] R. Vijayalakshmi, M. Jayachandran, C. Sanjeeviraja, Curr. Appl. Phys. 3 (2003) 171-175.

[11] S. H. Baeck, T. F. Jaramillo, C. Brandli, E. W. McFarland, J. Comb. Chem. 4 (2002) 563-568.

[12] A. A. Khokhlov, L. V. Pugolovkin, M. I. Borzenko, G. A. Tsirlina, Electrochemica Acta 54 (2009) 5439-5448.

[13] M. Deepa, A. K. Srivastava, S. N. Sharma, Govind, S. M. Shivaprasad, Appl. Surf. Sci. 254 (2008) 2342-2352.

[14] M. Deepa, A. K. Srivastava, Sol. Energy Mater. Sol. Cells 92 (2008) 170-178.

[15] G. A. Tsirlina, Solid State Ionics 176 (2005) 1681-1686.

[16] Y. S. Krasnov, G. Y. Kolbasov, Electrochim. Acta 49 (2004) 2425-2433.

[17] M. Fathy, A. B. Kashyout, M. Soliman, in International conference on sustainable energy; Technologies, materials and environmental issues, Cairo, Egypt, (2007) 21.

[18] Z. Yu, X. Jia, J. Du, J. Zhang, Sol. Energy Mater. Sol. Cells 64 (2000) 55-63.

[19] A. K. Srivastava, M. Deepa, S. Singha, R. Kishore, S. A. Agnihotry, Solid State Ionics 176 (2005) 1161-1168.

[20] A. L. Larsson, G. A. Niklasson, Sol. Energy Mater. Sol. Cells 84 (2004) 351-360.

[21] C. Liao, F. Chen, J. Kai, Sol. Energy Mater. Sol. Cells 90 (2006) 1147-1155.

[22] R. Vijayalakshmi, M. Jayachandran, D. C. Trivedi, C. Sanjeeviraja, Ionics 10 (2004) 151-154 .

[23] A. G. Fihlo, V. N. Freire, J. M. Sasaki, J. M. Fihlo, J. F. Juliao, U. U. Gomes, J. Raman Spectrosc. 31 (2000) 451-454.

[24] C. G. Granqvist, Sol. Energy Mater. Sol. Cells 60 (2000) 201–262.

[25] A. Siokou, S. Ntais, S. Papaefthimiou, G. Leftheriotis, P. Yianoulis, Surf. Sci. 566–568 (2004) 1168-1173.

[26] G. A. Niklasson, L. Berggren, A. Jonsson, R. Ahuja, N. V. Skorodumova, J. Backholm, M. Stromme, Sol. Energy Mater. Sol. Cells 90 (2006) 385-394.

[27] J. Zhang, J. P. Tu, X. H. Xia, Y. Qiao, Y. Lub, Sol. Energy Mater. Sol. Cells 93 (2009) 1840-1845.

[28] N. R. de Tacconi, C. R. Chenthamarakshan, K. L. Wouters, F. M. MacDonnell, K. Rajeshwar, J. Electroanal. Chem. 566 (2004) 249–256.

[29] M. Deepa, R. Sharma, A. Basu, S.A. Agnihotry, Electrochim. Acta 50 (2005) 3545–3555.

Chapter 6
Conclusions

Controlled synthesis of WO_3 nanoparticles has been a focused subject to explore nanostructure-dependent properties of WO_3. In particular, there are needs for economic and environmentally benign synthetic routes which can produce WO_3 nanoparticles efficiently. With this regard, the present thesis primarily concerns the structural control and characterization of WO_3 nanoparticles by aqueous solution methods. The aqueous solution methods focused in this study are hydrothermal method, aqueous sol-gel method and galvanostatic electro deposition. The various structures of WO_3 nanoparticles such as nanoplate, nanoneedles and spherical nanoparticles have been successfully obtained by these methods. As an important property, electrochromic performance of WO_3 nanoparticle films has been characterized. The main conclusions in this study are summarized as follows.

In Chapter 1, the properties of WO_3 nanoparticles, their applications and their synthetic routes were introduced. Then the background of this study and its objectives were explained.

In Chapter 2, a facile synthesis route of monoclinic WO_3 square nanoplates via mild hydrothermal treatment of ion-exchanged precursor was proposed. The ion-exchanged precursor was prepared by passing the sodium tungstate solution (Na_2WO_4) through a protonated cation-exchange resin, and used as impurity-free acidified precursor for synthesizing $WO_3 \cdot H_2O$ nanoplates. No shape-directing additive was employed. The effects of mild hydrothermal conditions such as reaction temperature and time on the morphology and structure of $WO_3 \cdot nH_2O$ have been studied systematically. The $WO_3 \cdot H_2O$ with an orthorhombic structure and platelet-like morphology was synthesized at 50 °C for 8 h. The morphological evolution to square platelet proceeded with an increase of aging time. After aging for 24 h, the $WO_3 \cdot H_2O$ square nanoplates were predominantly synthesized. The square nanoplates consisted of a few or several stacked thin layers (thickness, ~10nm/layer), and provided the well-defined {010} facet for two dominantly exposed surfaces. Their lateral dimension reached several hundreds of nanometers. In addition, the monoclinic WO_3

nanoplates were successfully obtained by dehydration-induced topochemical transformation of the $WO_3 \cdot H_2O$ nanoplates. It is thus demonstrated that the mild aging (50 °C) of the ion-exchanged precursor is a simple and impurity-free synthetic route for $WO_3 \cdot H_2O$ nanoplates and monoclinic WO_3 nanoplates. It can be expected that this synthetic strategy with such a low temperature will receive some benefits as inexpensive and versatile techniques.

In Chapter 3, one-dimensional crystal growth of orthorhombic $WO_3 \cdot 0.33H_2O$ was demonstrated by hydrothermal treatment of ion-exchanged precursor. The effects of hydrothermal conditions such as reaction temperature and time on the morphology and structure of $WO_3 \cdot nH_2O$ have been studied systematically. The $WO_3 \cdot 0.33H_2O$ with an orthorhombic structure and needle-like morphology was synthesized at 120 °C for 5 h. No significant change in the structure and morphology was observed with increasing reaction time to 24 h. At the same temperature, the $WO_3 \cdot 0.33H_2O$ grew preferentially along the [100] direction, and was eventually enclosed by {001}, {010} and {110} facets. The observed needle-like evolution has been explained based on the crystal structure of orthorhombic $WO_3 \cdot 0.33H_2O$. The isoelectric point (IEP) of nanoneedles was determined to be pH~1.5, and they could be stabilized when solution pH was controlled to be ~4. The $WO_3 \cdot 0.33H_2O$ nanoneedle was fully dehydrated when it was heated at 350 °C in air. Phase transformation to the hexagonal WO_3 was induced by this dehydration.

In Chapter 4, WO_3 nanoparticle films were fabricated by aqueous sol-gel method using ion-exchanged precursor. The ion-exchange precursor was spin-coated on ITO glass, and then annealed at 300 ^{o}C. Stabilizing agents of hydrogen peroxide and oxalic acid have been added to the ion-exchanged precursor to prevent fast gelation and precipitation of the precursor. The effect of the stabilizing agents on the microstructures and electrochromic performance of the obtained thin films have been investigated. The crystal structure of pure

WO_3 without the additive exhibited hexagonal structure. Monoclinic structure formed from samples contained 1% hydrogen peroxide and a mixture of 1% hydrogen peroxide and 4% oxalic acid. The effect of number of layers, and additive type; hydrogen peroxide and/or oxalic acid, were investigated. The thickness of the prepared WO_3 thin films was ranged between 0.33 μm to 9.82 μm, depending on the number of applied layers. Hydrogen peroxide and oxalic acid additives led to an open porous structure and increased the diffusion coefficient from 5.3×10^{-14} to 3.1×10^{-9} cm^2/s. The highest coloration efficiency of 64.2 cm^2/C was obtained for the open porous structure of the two-layer film prepared with W^+ ion concentration of 0.1 M, and 1% hydrogen peroxide and 4% oxalic acid.

In Chapter 5, WO_3 nanoparticle films were fabricated by galvanostatic electrodeposition. The effect of preparation parameters such as tungsten ions concentration, pH, current density and annealing on the properties and performance of WO_3 thin films electrochromic materials were investigated. Triclinic WO_3 structure was prepared at 0.1 M of W^+ and current density of 0.5 mA/cm^2, while at 0.2 M of W^+ and 1 mA/cm^2, orthorhombic structure was revealed. The highest diffusion coefficient of $6.81 \times 10^{-11} cm^2/S$ and coloration efficiency of 62.6 cm^2/C were obtained for the films prepared at pH 2, 1 mA/cm^2, and 0.1 M of W^+.

In this study, the aqueous solution methods have been proven to be effective for structure control of WO_3 nanoparticles. Following the syntheses of WO_3 nanoplates and nanoneedles, their uniform assembly is a remained challenge. The assembled nanostructures would offer unique properties that do not exist in bulk form.

Finally, the author hopes that the findings and strategies obtained in this study will contribute to the progress in science and engineering.

Acknowledgement

This doctoral thesis has been completed under the guidance of Professor Makio Naito of Joining and Welding Research Institute (JWRI), Osaka University. I would like to express my heartiest gratitude to him for his valuable advices and discussions throughout this work.

I am grateful to Professor Toshihiro Tanaka and Professor Yasufumi Fujiwara, of Division of Materials and Manufacturing Science, Graduate School of Engineering, Osaka University, and Associate Professor Hiroya Abe of JWRI for their peer reviewing of the thesis with valuable advices. I would like also to thank Associate Professor Yoshikazu Suzuki of University of Tsukuba for his stimulating discussions.

I wish to express my appreciation to Japan International Cooperation Agency (JICA) and Egyptian-Japanese University of Science and Technology (E-JUST) for funding and providing the opportunity to enter the doctor course of engineering, Osaka University.

I wish to express my appreciation to all the members of Professor Naito's laboratory, especially Mr. Kazuo Kuruma and Miss. Eri Nakamura for their excellent contributions to this work.

I am grateful to Professor Hesham Mohamed Abdel-Fattah Soliman and Professor Abd El-Hady Bashir Kashyout of Advanced Technology and New Materials Research Institute, City for Scientific Research and Technology Applications, (CSRTA) Alexandria, Egypt. And Professor Abdel Salam Mohammed Abu Sehly, Faculty of Science, Al-Azhar University, Egypt For their remarkable scientific supports.

Among my colleagues at CSRTA, I wish to express my appreciations to Dr. Abu Bakr Ahmed Amine, Dr. Marwa Fathy Ibraheem, and Dr. Hassan Shokry Hassan for their supports.

I would like to express a special thanks to my parents, wife, daughters, and all my family for their continuous encouragement and supports.

List of publications

[1] H. M. A. Soliman, A. B. Kashyout, Mohamed S. El Nouby, A. M. Abosehly, “Preparation and characterizations of tungsten oxide electrochromic nanomaterials”, Journal of Materials Science: Materials in Electronics 21 (2010) 1313–1321.

[2] H. M. A. Soliman, A. B. Kashyout, Mohamed S. El Nouby, A. M. Abosehly, “Effect of hydrogen peroxide and oxalic acid on electrochromic nanostructured tungsten oxide thin films”, International Journal of Electrochemical Science 7 (2012) 258 – 271.

[3] Mohamed Elnouby, Kazuo Kuruma, Eri Nakamura, Hiroya Abe, Yoshikazu Suzuki, Makio Naito, “Facile synthesis of $WO_3 \cdot H_2O$ square nanoplates via a mild aging of ion-exchanged precursor”, Journal of the Ceramic Society of Japan 121 (2013) 907-911.

[4] Mohamed Elnouby, Kazuo Kuruma, Eri Nakamura, Hiroya Abe, Yoshikazu Suzuki, Makio Naito, “Synthesis of $WO_3 \cdot 0.33H_2O$ nanoneedles by hydrothermal treatment of ion-exchanged precursor”, Journal of Flux Growth 8 (2013) 62-65.